

Spring 1987

# INELASTIC ELECTRON SCATTERING FROM MOLYBDENUM-92

THOMAS EDWARD MILLIMAN

*University of New Hampshire, Durham*

Follow this and additional works at: <https://scholars.unh.edu/dissertation>

---

## Recommended Citation

MILLIMAN, THOMAS EDWARD, "INELASTIC ELECTRON SCATTERING FROM MOLYBDENUM-92" (1987). *Doctoral Dissertations*. 1513.

<https://scholars.unh.edu/dissertation/1513>

This Dissertation is brought to you for free and open access by the Student Scholarship at University of New Hampshire Scholars' Repository. It has been accepted for inclusion in Doctoral Dissertations by an authorized administrator of University of New Hampshire Scholars' Repository. For more information, please contact [nicole.hentz@unh.edu](mailto:nicole.hentz@unh.edu).

## **INFORMATION TO USERS**

While the most advanced technology has been used to photograph and reproduce this manuscript, the quality of the reproduction is heavily dependent upon the quality of the material submitted. For example:

- Manuscript pages may have indistinct print. In such cases, the best available copy has been filmed.
- Manuscripts may not always be complete. In such cases, a note will indicate that it is not possible to obtain missing pages.
- Copyrighted material may have been removed from the manuscript. In such cases, a note will indicate the deletion.

Oversize materials (e.g., maps, drawings, and charts) are photographed by sectioning the original, beginning at the upper left-hand corner and continuing from left to right in equal sections with small overlaps. Each oversize page is also filmed as one exposure and is available, for an additional charge, as a standard 35mm slide or as a 17"x 23" black and white photographic print.

Most photographs reproduce acceptably on positive microfilm or microfiche but lack the clarity on xerographic copies made from the microfilm. For an additional charge, 35mm slides of 6"x 9" black and white photographic prints are available for any photographs or illustrations that cannot be reproduced satisfactorily by xerography.

Order Number 8722437

**Inelastic electron scattering from  $^{92}\text{Mo}$**

Milliman, Thomas Edward, Ph.D.

University of New Hampshire, 1987

**U·M·I**  
300 N. Zeeb Rd.  
Ann Arbor, MI 48106

**PLEASE NOTE:**

In all cases this material has been filmed in the best possible way from the available copy. Problems encountered with this document have been identified here with a check mark .

1. Glossy photographs or pages \_\_\_\_\_
  2. Colored illustrations, paper or print \_\_\_\_\_
  3. Photographs with dark background \_\_\_\_\_
  4. Illustrations are poor copy \_\_\_\_\_
  5. Pages with black marks, not original copy \_\_\_\_\_
  6. Print shows through as there is text on both sides of page \_\_\_\_\_
  7. Indistinct, broken or small print on several pages  \_\_\_\_\_
  8. Print exceeds margin requirements \_\_\_\_\_
  9. Tightly bound copy with print lost in spine \_\_\_\_\_
  10. Computer printout pages with indistinct print \_\_\_\_\_
  11. Page(s) \_\_\_\_\_ lacking when material received, and not available from school or author.
  12. Page(s) \_\_\_\_\_ seem to be missing in numbering only as text follows.
  13. Two pages numbered \_\_\_\_\_. Text follows.
  14. Curling and wrinkled pages \_\_\_\_\_
  15. Dissertation contains pages with print at a slant, filmed as received \_\_\_\_\_
  16. Other Page 66 has print missing. Best copy available.
- 
- 

University  
Microfilms  
International

**INELASTIC ELECTRON SCATTERING FROM  $^{92}\text{Mo}$**

**by**

**Thomas Edward Milliman  
M.S., University of Wisconsin, 1980  
B.A., Grinnell College, 1978**

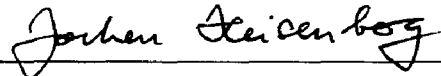
**A DISSERTATION**

**Submitted to the University of New Hampshire  
in Partial Fulfillment of  
the Requirements for the Degree of**

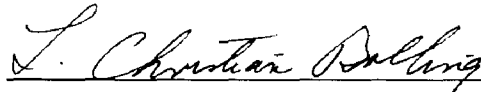
**Doctor of Philosophy  
in  
Physics**

**May, 1987**

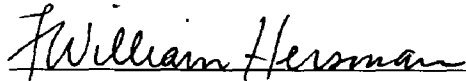
This dissertation has been examined and approved.



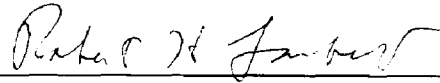
Dissertation director, Jochen Heisenberg  
Professor of Physics



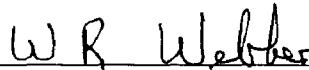
L. Christian Balling, Professor of Physics



F. William Hersman, Assistant Professor of Physics



Robert H. Lambert, Professor of Physics



William R. Webber, Professor of Physics

**To my family and friends.**

## Acknowledgements

The work described here has been carried out by many people. The entire UNH Nuclear Physics Group consisting of Jochen Heisenberg, John Dawson, Bill Hersman, John Calarco, John Wise, Steve Frolking and Jimmy Connelly helped in the long hours of data taking and analysis. In a very real sense this is their work as well as mine. In particular Jochen Heisenberg and Bill Hersman have not only taught me most of the nuclear physics that I have learned they have also provided the encouragement necessary to keep this work moving forward. During the data taking valuable assistance was also provided by Costas Papanicolas and Bruce Miller from the University of Illinois and the entire operating staff at the Bates Laboratory. My thanks goes also to K. Allaart for sending the results of his Broken-Pair calculations and to H. P. Blok for communicating this need. During the data analysis special support was provided by the staff of the UNH Research Computing Center and I would particularly like to thank Dr. W. Lenharth for this effort. Finally I would like to acknowledge Mark McConnell, Craig Pollock and Jimmy Connelly whose friendship and support has been unwavering and whose humor has helped to keep me sane.



## Table of Contents

Dedication .....	iii
Acknowledgements .....	iv
Table Captions .....	vii
Figure Captions .....	viii
Abstract .....	xiii
<b>Section</b> .....	<b>page</b>
Introduction .....	1
1.0 Nuclear Structure .....	4
1.1 Independent Particle Model .....	4
1.2 Groundstate Correlations .....	5
1.3 Core Polarization .....	7
1.4 Nuclear Currents .....	8
2.0 Electron Scattering Formalism .....	10
2.1 Kinematics .....	10
2.2 Born Approximation .....	12
2.3 Radiative Corections .....	18
3.0 Data Collection .....	21
3.1 The Bates Electron Scattering Facility .....	21
3.2 Targets .....	28
3.3 Kinematics .....	29
4.0 Data Reduction - Cross Sections .....	34
4.1 Data Files .....	34
4.2 Peak Shape Fitting .....	34
4.3 Corrections to the Data .....	37
4.4 Normalizations .....	40

5.0	Data Reduction - Densities .....	47
5.1	Density Fitting Programs .....	47
5.2	Models for the Transition Densities .....	48
6.0	Discussion of Results .....	52
6.1	Model Calculations .....	52
6.2	Elastic Scattering .....	55
6.3	The $\pi(1g_{9/2})^2$ Multiplet .....	58
6.4	The $5^-$ State at 2.537 MeV .....	63
6.5	The $3^-$ State at 2.850 MeV .....	69
6.6	The $7^-$ State at 4.555 MeV .....	71
6.7	States Between 3.0 and 4.0 MeV .....	77
6.8	States Between 4.0 and 5.1 MeV .....	84
6.9	The States at 4.690 and 4.925 MeV .....	93
7.0	Conclusion .....	96
	Bibliography .....	99
	Appendix A .....	103
	Appendix B .....	107
	Appendix C .....	142

## Table Captions

3.1. Data from ORNL isotopic analysis of the target. ....	28
3.2. Results from calibration runs taken during the forward scattering part of the experiment. ....	31
3.3. Results from calibration runs taken during the backward scattering part of the experiment. ....	32
3.4. Kinematics for both the backward and forward scattering parts of this experiment. ....	33
4.1. Ground state charge density Fourier–Bessel Parameters. These parameters were obtained by fitting the data from previous experiments only. ....	41
4.2. Normalization factors for the forward scattering data points. ....	44
4.3. Ground state charge density Fourier–Bessel Parameters for fit including data from this experiment ....	45
4.4. Normalization factors obtained for the backward scattering data points. ....	46
5.1. Separation energies used in the SPM fits for transition densities ....	50
6.1. Summary of data on $8^+$ states. ....	62
6.2. Occupation estimates of the $2p$ and $1g$ proton orbits taken from the observed quenching of the transition current relative to the transition charge. ....	68
6.3. Summary of information on the occupation of the $\pi 1g_{9/2}$ orbit in $N=50$ nuclei. ....	68
6.4. Radius of the $\pi 1f_{5/2}$ orbit determined by fitting the E7 form factors in $^{92}\text{Mo}$ . ....	77

## Figure Captions

	page
1.1. The independent particle model for $^{92}\text{Mo}$ . . . . .	5
1.2. Known excitation spectrum for $^{92}\text{Mo}$ . . . . .	6
2.1. Scattering diagram for Born scattering. . . . .	11
2.2. Geometry of the scattering process in the laboratory frame. . . . .	13
2.3. Geometry for radiative processes. . . . .	19
2.4. Scattering diagrams for the radiative processes accounted for in the analysis. . . . .	20
3.1. Layout of the MIT-Bates facility. . . . .	22
3.2. Cutaway of the spectrometer, target, and focal plane instrumentation at Bates. . . . .	24
3.3. The focal plane instrumentation consists of five detectors: VDC-I, VDC-II, TA, Č1, and Č2. . . . .	25
3.4. Quantities measured by a VDC. . . . .	26
3.5. Quantities measured by the transverse array. . . . .	27
4.1. Electron spectrum from scattering at 189.6 Mev, and 65.0 degrees. . . . .	36
4.2. The ground state density of $^{92}\text{Mo}$ obtained by fitting data from this experiment along with the existing data. Also shown are the statistical errors associated with this fit. . . . .	43
6.1. Excited states in $^{92}\text{Mo}$ below 5.2 MeV and the predictions of two calculations. . . . .	54
6.2. Elastic scattering form factor showing the $(e, e')$ data included in the fit. The data have all been recalculated to 370.0 MeV. The Mainz data are taken from the thesis of B. Dreher ( <i>ref.</i> 28), the Saclay data are from Ho,	

	<i>et al.</i> (ref. 29) and the Glasgow data are from Singhal, <i>et al.</i> (ref.30). The curve (A) is a distorted wave fit described in Chapter 4. ....	56
6.3.	The difference in the ground state charge densities between $^{92}\text{Mo}$ and $^{90}\text{Zr}$ . The curve is the density corresponding to a $(\pi 1g_{9/2})^2_{0^+}$ configuration which has been normalized so that $4\pi \int_0^{10} \rho(r)r^2 dr = 2e$ . The error in the difference is taken to be the sum of the errors for the two densities. ...	57
6.4.	Excitation energies of states attributed to the $\pi(1g_{9/2})^2$ configuration.	58
6.5.	Forward scattering form factors for the $2^+$ through $8^+$ states in $^{92}\text{Mo}$ . The curves showing the DWBA fits are discussed in the text. ....	60
6.6.	Transition charge densities for the $2^+, 4^+, 6^+, 8^+$ multiplets observed in $^{86}\text{Sr}$ and $^{92}\text{Mo}$ . In $^{86}\text{Sr}$ the multiplet is due to $\nu(1g_{9/2})^2$ configuration while in $^{92}\text{Mo}$ it is due to a $\pi(1g_{9/2})^2$ configuration. ....	61
6.7.	Form factors for forward and backward scattering from the state at 2.527 MeV. The curves are the result of simultaneously fitting the charge and current densities in the FBE. The solid curve is the full fit and the dotted curve is the longitudinal contribution only. ....	64
6.8.	Transition densities for the E5 transitions in $^{89}\text{Y}$ , $^{90}\text{Zr}$ and $^{92}\text{Mo}$ . The strength of the transition charge increases with Z while the strength of the transition current decreases. The solid curves are the BP predictions and the dashed curves are the predictions of the SM calculation. ....	65
6.9.	Forward and backward scattering form factors for the $3^-$ level at 2.850 MeV. The solid curves is the full DWBA fit to the data while the dashed curves gives the longitudinal contribution only. ....	70
6.10.	Transition charge and current densities for the $3^-$ state at 2.850 MeV. The solid curve is the Broken-Pair prediction. ....	71
6.11.	Spectra of electrons scattered from $^{90}\text{Zr}$ (top) and $^{92}\text{Mo}$ (bottom) at backward angles. The momentum transfer of the two spectra have roughly	

the same value. The strong $7^-$ states stand out clearly at the backward angles and higher momentum transfers. ....	73
6.12. Forward and backward scattering form factors for the $7^-$ state at 4.555 MeV. The solid curve is the full DWBA fit. The dashed curve gives the longitudinal contribution only. ....	74
6.13. The transition charge and current densities for the $7^-$ states in $^{88}\text{Sr}$ , $^{90}\text{Zr}$ and $^{92}\text{Mo}$ . The solid curve labeled (A) is the broken-pair prediction. The dashed curve labeled (B) is the prediction of a pure single-particle transition. ....	76
6.14. Form factor and transition charge density for the second $2^+$ state at 3.092 MeV. ....	78
6.15. Form factors and transition charge densities for the states at 3.369, 3.545 and 3.583 MeV. The solid curves in the form factor plots are the DWBA fits as described in the text. ....	80
6.16. Form factors and transition charge densities for the states at 3.626, 3.879 and 3.925 MeV. The solid curves in the form factor plots are the DWBA fits as described in the text. ....	83
6.17. Spectrum of scattered electrons for the excitations region 4.0 to 5.3 MeV. The energies listed above the spectrum indicate the levels which have been included in the peak shape fits. ....	85
6.18. Form factors for the states at 4.159 and 4.312 MeV. ....	87
6.19. Densities extracted for the states at 4.159 and 4.312 MeV. ....	88
6.20. Form factors and transition charge densities for the states at 4.495, 4.598, and 4.724 MeV. ....	90
6.21. Form factors for two possible $J^\pi = 1^-$ states in $^{92}\text{Mo}$ . No DWBA fit was done for the state at 4.634 MeV. The transition charge density for the state at 5.007 MeV assumes $J^\pi = 1^-$ . ....	91

6.22. Form factor and transition charge density for the state at 5.088 MeV .93

6.23. Form factors for the states at 4.690 and 4.925 MeV. Also shown are the transition current densities for states and the BP predictions for the first  $6^-$  and  $7^+$  states. ....94





## ABSTRACT

### INELASTIC ELECTRON SCATTERING FROM $^{92}\text{Mo}$

by

THOMAS E. MILLIMAN

University of New Hampshire, May, 1987

Differential cross sections for electron scattering from  $^{92}\text{Mo}$  have been measured for excitation energies less than 5.1 MeV. The momentum-transfer dependence of these cross sections has been mapped out over a range of 0.5 to 3.1  $fm^{-1}$  in the forward direction and 0.8 to 2.9  $fm^{-1}$  in the backward scattering direction. The elastic scattering data are analyzed along with existing data and muonic atom data to provide an improved description of the groundstate charge distribution. The inelastic scattering data for 23 excited states have been further analyzed to extract electromagnetic transition densities. These densities are discussed and when possible related to the underlying nuclear structure.

## Introduction

This thesis describes an experimental study of inelastic electron scattering from  $^{92}\text{Mo}$ . The experiment was undertaken to provide data which can be used to test microscopic descriptions of  $^{92}\text{Mo}$ . The electromagnetic transition densities determined from the data collected in this experiment represent just this type of information. The transition densities can be extracted reliably and often with small enough uncertainties to allow for quantitative tests of model wavefunctions and interactions. While a great deal of spectroscopic information already exists for  $^{92}\text{Mo}$ , the determination of these densities represents a significant increase in our knowledge of the excited state structure.

The experiment on  $^{92}\text{Mo}$  is part of a larger study of several nuclei in this mass region using the  $(e, e')$  reaction. The nuclei previously studied are  $^{87}\text{Sr}$ ,  $^{88}\text{Sr}$ ,  $^{89}\text{Y}$ , and  $^{90}\text{Zr}$ . Concurrently with this experiment the forward scattering data on  $^{86}\text{Sr}$  were taken. These nuclei are all near the shell closures at  $Z=38$  and  $40$  and  $N=50$ . As a result, the low-lying excited states often involve only a small number of valence nucleons. The densities for these states which are dominated by a few single-particle components are most easily interpreted and provide the best tests of nuclear models. It is mainly these states which are of interest in this study.

Several papers on the previously studied nuclei have already been published. A comparison of low-lying quadrupole excitations in  $^{88}\text{Sr}$ ,  $^{89}\text{Y}$ , and  $^{90}\text{Zr}$ <sup>[1]</sup> established the strong single-particle nature of these states which had previously been thought to be collective vibrations. A comparison of E5 transitions<sup>[2]</sup> was used to estimate the ground state occupation of the proton  $1g_{9/2}$  orbit. Results for the positive parity states in  $^{90}\text{Zr}$  are discussed in a paper by Heisenberg, *et al.*<sup>[3]</sup>. Early results from the  $^{92}\text{Mo}$  experiment have already been published in a comparison of the proton  $1g_{9/2}$  orbit size in  $^{88}\text{Sr}$ ,  $^{90}\text{Zr}$ , and  $^{92}\text{Mo}$ <sup>[4]</sup>. The interpretation of the  $^{92}\text{Mo}$  data presented here will draw heavily from a comparison with the previously studied nuclei.

There were several objectives in extending this study to include  $^{92}\text{Mo}$ . In general because of the increased occupancy of the proton  $1g_{9/2}$  orbit, the extension of the study to  $^{92}\text{Mo}$  will improve the sensitivity of our measurements to the observables involving this orbit. More specific objectives were,

- Make a comparison of the band of states with  $J^\pi = 2^+, 4^+, 6^+, \text{ and } 8^+$  based on the  $\pi(1g_{9/2})^2$  configuration. These states have been observed in  $^{88}\text{Sr}$  and  $^{90}\text{Zr}$ . In these nuclei their presence is due to small admixtures of the  $\pi(1g_{9/2})^2_{0^+}$  configuration in the ground state. In the  $^{92}\text{Mo}$  ground state this component is the dominant one because of the additional two protons.
- Extend the comparison of the low-lying quadrupole excitations.
- Compare the low-lying  $3^-$  state at 2.850 MeV with the  $3^-$  state at 2.734 MeV in  $^{88}\text{Sr}$ . (The state in  $^{90}\text{Zr}$  which fits in with this comparison was unresolved from a nearby  $4^-$  state.)
- Further test the ideas put forward in *ref. 2* which relate the reduction in transition current strength for the lowest E5 excitation to ground state occupation of the  $\pi 1g_{9/2}$  orbit.
- Locate the  $7^-$  state corresponding to the  $1f_{5/2}$  to  $1g_{9/2}$  proton transition. This state has been observed in  $^{88}\text{Sr}$  and  $^{90}\text{Zr}$ . A possible weak-coupling doublet based on this state has also been observed in  $^{89}\text{Y}$ .

The experiment was performed at the MIT-Bates Linear Accelerator Laboratory. Measurements were made at forward angles covering a momentum transfer region of  $0.5 \leq q_{eff} \leq 3.1 \text{ fm}^{-1}$  and at backward angles over roughly the same region.

Chapter 1 is a general discussion of the nuclear structure in this region and of a few aspects which are of concern in the interpretation of results. Chapter 2 summarizes the formalism of inelastic electron scattering as it applies to this

experiment. In Chapter 3 the experimental details are discussed and the kinematics chosen for this experiment are summarized. Chapters 4 and 5 explain the reduction of the data to obtain the differential cross sections and transition densities respectively. In Chapter 6 the extracted densities are discussed along with possible interpretations. Chapter 7 summarizes the results which have been obtained.

## 1. Nuclear Structure

Nuclear models have long been applied successfully in the mass-90 region. While these models provide a good qualitative description of the nuclear structure, often the quantitative aspects are lacking. Typically the places where the models break down are the most interesting ones to examine. This chapter contains a review of the independent particle model for  $^{92}\text{Mo}$ . Following this is a brief discussion of three aspects of nuclear structure (ground state correlations, core polarization, and nuclear currents) where model calculations often have difficulty reproducing experimental results. This discussion should serve as a context in which the interpretation of results can be presented.

### 1.1 INDEPENDENT PARTICLE MODEL

*Figure 1.1* shows the independent particle model (IPM) for  $^{92}\text{Mo}$ . The neutrons form a closed shell at  $N=50$ . With  $Z=42$  the protons fill all the orbits through the  $2p_{1/2}$  orbit with the remaining two protons in the  $1g_{9/2}$  orbit. The gap to the next neutron orbit is roughly 4 MeV and below that excitation energy the excited states should be dominated by proton transitions among the  $1f_{5/2}$ ,  $2p_{3/2}$ ,  $2p_{1/2}$  and  $1g_{9/2}$  orbits.

*Figure 1.2* shows the spectrum of excited states for  $^{92}\text{Mo}$ . The spins and parities of the low-lying levels fit nicely into the framework of the IPM. Within this model negative parity states arise from removing protons from the  $1f_{5/2}$ ,  $2p_{3/2}$ , and  $2p_{1/2}$  orbits and placing them in the  $1g_{9/2}$  orbit. These are the dominant transitions which lead to the first  $3^-$ ,  $4^-$ , and  $5^-$  states. Positive parity states arise from recoupling of pairs in the  $1g_{9/2}$  orbit. The recoupling of a single proton pair in the  $1g_{9/2}$  orbit leads to states with  $J^\pi = 2^+, 4^+, 6^+$ , and  $8^+$  all of which are observed at low excitation energy. The only known level below 3 MeV excitation which is not predicted as a  $1p1h$  excitation from the IPM ground state is the  $0^+$  level at 2.512 MeV.

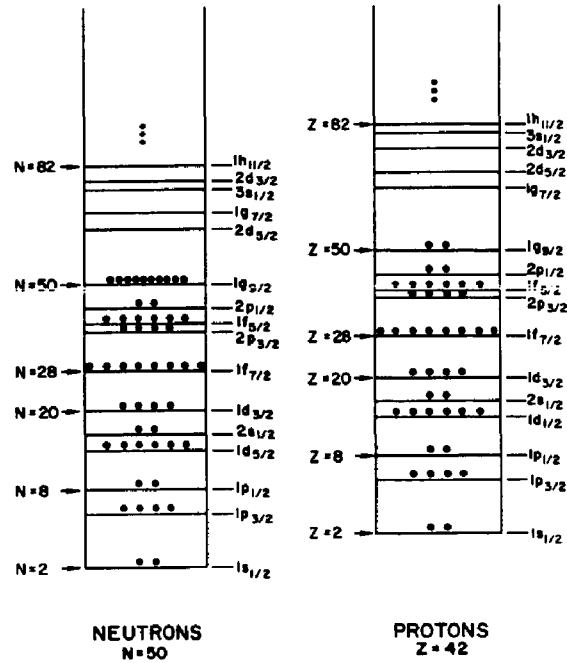


Figure 1.1 The independent particle model for  $^{92}\text{Mo}$ .

## 1.2 GROUND STATE CORRELATIONS

In the IPM the orbitals fill in order, the more tightly bound orbits filling first, and the ground state occupation has a sharp cutoff. This is typical of a system of non-interacting fermi particles. The ground state occupation is strictly a function of particle numbers and orbit energies. The shell model extends this picture by introducing a residual interaction between valence nucleons. This interaction leads to a mixture of configurations in the ground state.

Configuration mixing in the mass-90 region has been studied extensively. In  $^{90}\text{Zr}$  the first excited state is a  $0^+$  state at 1.761 MeV. The  $^{90}\text{Zr}$  ground state can be crudely pictured as a  $^{88}\text{Sr}$  core coupled with two protons in a configuration,

$$\alpha(2p_{1/2})_{0^+}^2 + \beta(1g_{9/2})_{0^+}^2.$$

The excited  $0^+$  state is then due to the orthogonal mixture of the two protons

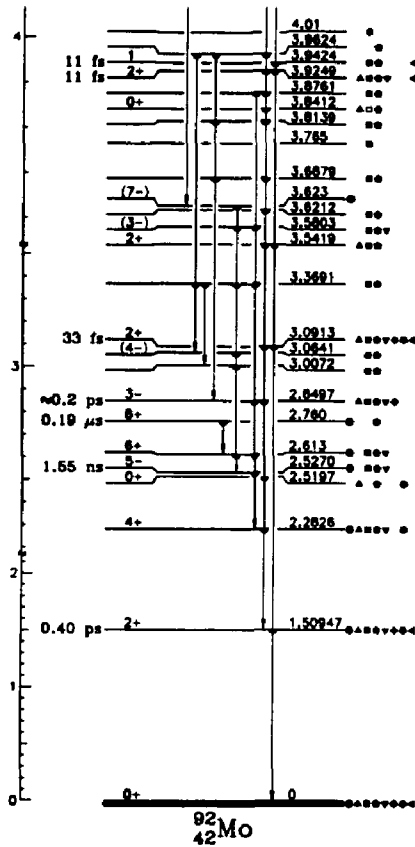


Figure 1.2 Excitation spectrum for  $^{92}\text{Mo}$ .

outside the  $^{88}\text{Sr}$  core. Mixing in the  $^{90}\text{Zr}$  ground state has been investigated many times using transfer reactions<sup>[6-7]</sup>. An analysis<sup>[6]</sup> of these experiments shows that configuration mixing involving only the  $1g_{9/2}$  and  $2p_{1/2}$  orbits is inadequate to account for the measured lifetime of the excited  $0^+$  state. If additional configurations which depopulate the  $2p_{3/2}$  orbit are included, agreement with the lifetime measurement can be achieved. The actual ground state occupation in  $^{90}\text{Zr}$  clearly does not have a sharp cutoff as in the IPM.  $^{88}\text{Sr}$  has also shown indications of configuration mixing. The observation of the  $2^+$ ,  $4^+$ ,  $6^+$ ,  $8^+$  band in electron scattering from  $^{88}\text{Sr}$  indicates the presence of a  $\pi(1g_{9/2})^2_{0^+}$  component in the ground state of that nucleus. A similar situation exists for  $^{92}\text{Mo}$

and the  $0^+$  state at 2.512 MeV is analogous to the first excited state in  $^{90}\text{Zr}$ .

Correlations between pairs of nucleons coupled to spin zero tend to soften the fermi level, *i.e.* increase the number of orbitals which are neither filled nor empty but rather partially occupied. There is evidence that in the Pb-region mean-field calculations underpredict these correlations. The difference between the ground state charge densities of  $^{205}\text{Tl}$  and  $^{206}\text{Pb}$  has been determined by a combined analysis of muonic atom and electron scattering data<sup>[9]</sup>. A comparison with mean-field predictions indicates that reduction of 30% in the occupation of the  $\pi 3s_{1/2}$  orbit is needed to achieve agreement with the measured difference. It has also been suggested<sup>[10]</sup> that this reduced occupation is necessary to correctly predict the strength of magnetic transitions to high-spin states. The measured strengths are considerably less than predicted in shell model calculations. In general an understanding of the ground state correlations and occupations is a central topic in nuclear structure physics.

### 1.3 CORE POLARIZATION

The shell model divides the nucleus into two parts which are then treated separately. The "core" contains the nucleons which fill the last major neutron and proton shells. For  $^{92}\text{Mo}$  this would be all 50 neutrons and 28 protons. The core provides a mean field in which the remaining 14 valence protons interact. The core is considered to be inert and unaffected by the movement of the valence particles. For some time this approximation has been known to be a serious deficiency of the model and several schemes to account for the polarization of the core have been employed. Most notably these include the use of effective charges for both the proton and neutron.

This problem is especially relevant when modeling transition densities obtained from electron scattering. Electron scattering is mainly sensitive to the proton distributions in the nucleus. For strong neutron single-particle transitions almost all the scattering can be due to the polarization of the protons in



the core. Even for a state dominated by a few proton single-particle transitions the polarization density can be of the same order of magnitude as the components included in the model. Effective charges, which merely change the magnitude of the single-particle components of the density, can not be expected to fully account for the polarization. In general the polarization densities will not have radial shapes which follow the dominant single particle components. Their presence can affect both the magnitude and shape of the measured density. Attempts to understand this effect and to account for it are very important in interpreting the results of this experiment.

#### 1.4 NUCLEAR CURRENTS

There has been considerable interest lately in studying electromagnetic currents in nuclei. Traditional nuclear models construct a nuclear Hamiltonian in a non-relativistic way using Schrödinger's Equation. In these models the interactions used are incomplete and terms in the Hamiltonian (*e.g.* the spin-orbit term in the shell model) are often included in an *ad hoc* manner. The presence of these terms influences the form of other operators such as the one-body charge and current operators. In most cases the corrections to the charge operator are well understood while an appropriate form for the current operator is not. It is also unclear what effect meson-exchange currents will have on the current operator. A determination of the nuclear currents is needed to resolve some of these theoretical questions.

The measurement of transition current densities is a fairly recent development. Electron scattering is sensitive to nuclear currents through the transverse polarization of the exchanged virtual photon. The currents have two components, a convection current due to the motions of the charges in the nucleus, and a magnetization current due to the intrinsic magnetic moments of the protons and neutrons. For natural parity transitions the nuclear currents usually add only a small contribution to the cross section. For the unnatural parity transitions the entire cross section is due to a nuclear current density but the cross

sections themselves are usually very small. In general the measured current densities have been significantly smaller than predicted by nuclear models and there is considerable interest in understanding this 'current quenching.'

In Schwentker, *et al.*<sup>[2]</sup> the possibility that some of the quenching is due to a nuclear structure effect was discussed. The presence of backward going particle-hole transitions causes a quenching of the current density relative to the charge density. The backward going amplitudes are possible because of pairing correlations which lead to partial vacancy of the hole orbits.

There is also considerable interest in the effect of non-nucleonic degrees of freedom on the current densities. In particular there has been much work on calculating the effects of meson-exchange currents on the one-body current operator. The study of the  $7^-$  states in the mass-90 region is particularly relevant to this work. The single-particle E7 transitions have *both* charge *and* current densities which can be measured. The pure  $1f_{5/2} \rightarrow 1g_{9/2}$  transition accounts for the charge form-factor in  $^{90}\text{Zr}$  quite well. The same wavefunctions do not reproduce the contribution from current scattering. If we assume that the form of the charge operator is correct, the nucleonic degrees of freedom are fairly well determined from the charge scattering. The discrepancy with the current scattering then becomes an ideal case for studying the non-nucleonic effects.

## 2. Electron Scattering Formalism

The theory of electron scattering is well developed and can be found in numerous references<sup>[11-13]</sup>. In the analysis presented here we have treated the excitation of the nucleus in the one-photon or first Born approximation. The Born scattering is represented by the single scattering diagram shown in *fig. 2.1*. The actual scattering involves many additional processes which are loosely grouped into three categories: distortions, radiative corrections and dispersion corrections. Distortions and radiative corrections are taken into account in the analysis of the data and will be discussed briefly below. Dispersion corrections account for the possibility of exciting the nucleus through a multiple photon process (*i.e.* through some intermediary nuclear state.) These corrections are known to be small and have been ignored in this analysis. For a discussion of the errors this assumption introduces see deForest and Walecka<sup>[11]</sup>.

This chapter starts with a discussion of kinematics. This is followed by a discussion of the Born scattering and its relation to nuclear structure. Finally a section on radiative corrections will outline how the first Born cross section can be obtained from the experimental one.

### 2.1 KINEMATICS

*Figure 2.2* shows the lab geometry of the scattering. For the electron energies involved in the experiment, to good approximation, we can neglect the electron mass. The quantities shown in *fig. 2.2* and used throughout are:

$$a \cdot b \equiv a_0 b_0 - \vec{a} \cdot \vec{b}$$

$$p_i \equiv \left( \frac{E_i}{c}, \vec{p}_i \right) \equiv \text{incident electron 4-momentum}$$

$$p_f \equiv \left( \frac{E_f}{c}, \vec{p}_f \right) \equiv \text{final electron 4-momentum}$$

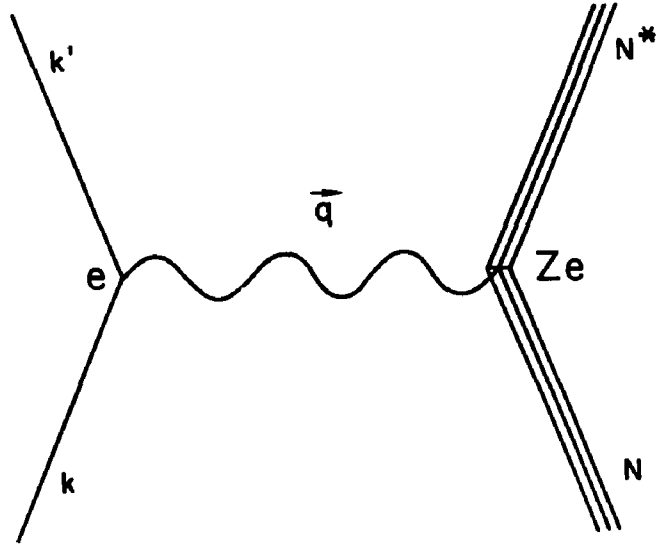


**Figure 2.1** Scattering diagram for Born scattering.

$P_i \equiv (Mc, 0) \equiv$  target nucleus incident 4-momentum

$P_f \equiv \left( \frac{T + M^* c^2}{c}, \vec{P}_f \right) \equiv$  target nucleus final 4-momentum

$M \equiv$  mass of target nucleus

$M^* \equiv$  mass of recoil nucleus

$T \equiv$  kinetic energy of recoil nucleus

$\hbar\omega \equiv$  excitation energy of the recoil nucleus

$\theta \equiv$  laboratory scattering angle

$\hbar q \equiv \hbar(q_0, \vec{q}) \equiv$  4-momentum transfer.

Conservation of momentum and energy gives

$$\hbar^2 \vec{q}^2 = \vec{p}_i^2 + \vec{p}_f^2 - 2\vec{p}_i \cdot \vec{p}_f \quad (2.1)$$

and,

$$E_i + Mc^2 = E_f + M^*c^2 + T \quad (2.2)$$

where,

$$M^*c^2 \equiv Mc^2 + \hbar\omega \quad (2.3)$$

Using these relationships we get,

$$E_f = \left\{ E_i - \left( \hbar\omega + \frac{\hbar^2\omega^2}{2Mc^2} \right) \right\} \eta \quad (2.4)$$

$$\eta \equiv \left( 1 + \frac{2E_i}{Mc^2} \sin^2 \frac{\theta}{2} \right)^{-1} \quad (2.5)$$

Electromagnetic form factors can be considered as a function of a single kinematic variable,  $q$ , the 4-momentum transfer. The magnitude of  $q$  is given by,

$$q^2 = 4 \frac{E_i E_f}{\hbar^2 c^2} \sin^2 \frac{\theta}{2}. \quad (2.6)$$

Mapping the form factors as a function of  $q$  can be accomplished either by varying  $\theta$  at a fixed  $E_i$  or by varying  $E_i$  at a fixed  $\theta$ .

## 2.2 BORN APPROXIMATION

The first Born Approximation to the cross section can be derived from first-order time dependent perturbation theory<sup>[14]</sup>. The interaction between the electron and the nucleus is written in terms of the electromagnetic charges and currents involved. The charges and currents of the electron can be calculated from the relativistic wavefunctions which are solutions to the Dirac Equation with an appropriate potential. The cross section can then be expressed in terms of the nuclear charge and current densities.

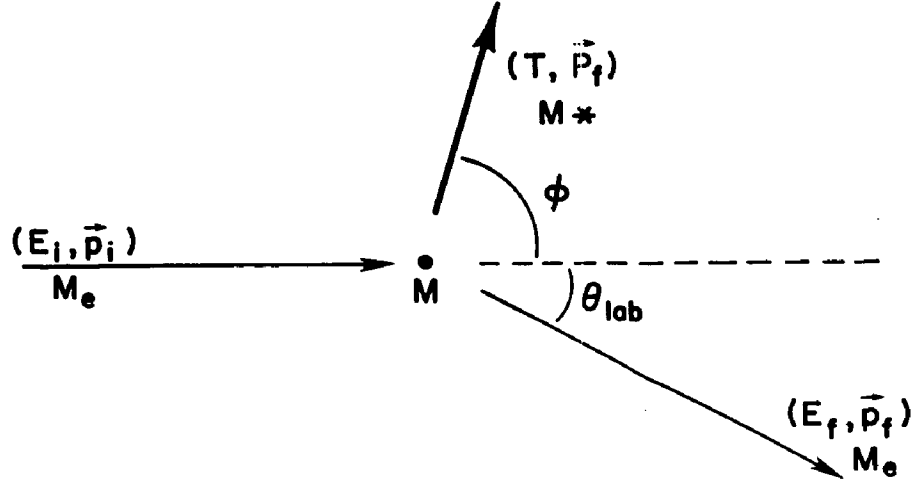


Figure 2.2 Geometry of the scattering process in the laboratory frame.

The relevant nuclear quantities in deriving the scattering cross section are the matrix elements of the charge and current operator between the initial and final nuclear states. A multipole expansion of these matrix elements can be given in terms of the reduced matrix elements which are referred to as transition densities,

$$\langle \Psi_f | \rho^{op}(\vec{r}) | \Psi_i \rangle = \sum_{LM} (J_i M_i L M | J_f M_f) \rho_L(r_N) Y_L^{*M}(\hat{r}_N) \quad (2.7)$$

$$\langle \Psi_f | \vec{J}^{op}(\vec{r}) | \Psi_i \rangle = \sum_{LM} (J_i M_i L M | J_f M_f) \quad (2.8)$$

$$[J_{L,L-1}(r_N) \vec{Y}_{L,L-1}^{*M}(\hat{r}_N) + J_{L,L+1}(r_N) \vec{Y}_{L,L+1}^{*M}(\hat{r}_N) + J_{L,L}(r_N) \vec{Y}_{L,L}^{*M}(\hat{r}_N)]$$

These relations define the four transition densities  $\rho_L$ ,  $J_{L,L-1}$ ,  $J_{L,L+1}$ , and  $J_{L,L}$ . Explicitly these are,

$$\rho_L(r) = \int \langle \Psi_f | \rho^{op}(\vec{r}) Y_L(\hat{r}) | \Psi_i \rangle d\hat{r} \quad (2.9)$$

$$J_{L,L'}(r) = \int \langle \Psi_f \| \vec{J}^{op}(\vec{r}) \cdot \vec{Y}_{L,L'}(\hat{r}) \| \Psi_i \rangle d\hat{r} \quad (2.10)$$

For these definitions we have used the Wigner–Eckhart theorem in the form,

$$\langle J_f M_f | T_{\lambda\mu} | J_i M_i \rangle = (J_i M_i \lambda \mu | J_f M_f) \langle J_f \| T_\lambda \| J_i \rangle \quad (2.11)$$

Selection rules dictate that the transition charge  $\rho_L$  and transverse electric currents  $J_{L,L-1}$  and  $J_{L,L+1}$  are non-zero only if the change in parity  $\Delta\pi$  is given by  $\Delta\pi = (-1)^L$  *i.e.* only for natural parity transitions. Similarly the transverse magnetic current  $J_{L,L}$  is non-zero only if  $\Delta\pi = (-1)^{L+1}$  *i.e.* for unnatural parity transitions.

#### Plane Wave Born Approximation

The plane wave Born Approximation (PWBA) assumes the electron wavefunctions are the plane-wave solutions to the Dirac Equation. The simple relation between the transition densities and the cross sections in the PWBA makes it useful for understanding the connection between these quantities. The derivation of the PWBA cross section has been given many times and only the main results are given here. We have the approximate result,

$$\left(\frac{d\sigma}{d\Omega}\right)_{PWBA} = 4\pi Z^2 \left(\frac{d\sigma}{d\Omega}\right)_{Mott} \eta \left\{ \sum_{L \geq 0} |F_L^C(q)|^2 + \left(\frac{1}{2} + \tan^2 \frac{\theta}{2}\right) \sum_{L \geq 1} [ |F_L^E(q)|^2 + |F_L^M(q)|^2 ] \right\}. \quad (2.12)$$

The Mott cross section is given by,

$$\left(\frac{d\sigma}{d\Omega}\right)_{Mott} = \frac{\alpha^2 \hbar^2 c^2}{4E_i^2 \sin^4 \frac{\theta}{2}} \cos^2 \frac{\theta}{2}. \quad (2.13)$$

All the nuclear structure information is contained in the form factors which are given by,

$$F_L^C(q) = \frac{\hat{J}_f}{\hat{J}_i} \int_0^\infty \rho_L(r) j_L(qr) r^2 dr \quad (2.14)$$

$$F_L^E(q) = \frac{\hat{J}_f}{\hat{J}_i \hat{L}} \int_0^\infty [\sqrt{L+1} J_{L,L-1}(r) j_{L-1}(qr) + \sqrt{L} J_{L,L+1}(r) j_{L+1}(qr)] r^2 dr \quad (2.15)$$

$$F_L^M(q) = \frac{\hat{J}_f}{\hat{J}_i} \int_0^\infty J_{L,L}(r) j_L(qr) r^2 dr \quad (2.16)$$

These form factors are Fourier-Bessel transforms of the transition densities into momentum space. In the PWBA the densities can be reconstructed by taking inverse transforms of the form factors. The form factors can be obtained directly from the measured cross sections.

The transition charge and current densities determined from electron scattering are related to the electromagnetic transition probabilities, B(EL) and B(ML), measured in Coulomb excitation or determined from lifetime measurements. These quantities are given by,

$$B(EL) = \left[ \frac{\hat{J}_f}{\hat{J}_i} \int_0^\infty \rho_L(r) r^{L+2} dr \right]^2 \quad (2.17)$$

and,

$$B(ML) = \frac{L}{L+1} \left[ \frac{\hat{J}_f}{\hat{J}_i} \int_0^\infty J_{L,L}(r) r^{L+2} dr \right]^2 \quad (2.18)$$

By comparison with Eqns. (2.14) and (2.16) it is clear that these probabilities are closely related to  $F_L^C(q)$  and  $F_L^M(q)$ . For small  $q$  the spherical Bessel functions are proportional to  $r^L$  so the B(EL) and B(EM) values are equivalent to the square of  $F_L^C(q)$  and  $F_L^M(q)$  near zero momentum transfer.

Because of the factor  $\left(\frac{1}{2} + \tan^2 \frac{\theta}{2}\right)$  in Eq. (2.12), the transverse contribution to the cross section increases at backward angles. If information on both the



transverse and longitudinal contributions is desired, both forward scattering and backward scattering data must be taken.

As shown in an article by Heisenberg<sup>[18]</sup> the continuity equation can be used to eliminate one of the three densities  $\rho_L$ ,  $J_{L,L+1}$ ,  $J_{L,L-1}$ . Expressing the continuity equation in terms of the transition densities gives,

$$\hat{L}\frac{\omega}{c}\rho_L(r) = \sqrt{L}\left(\frac{d}{dr} - \frac{L-1}{r}\right)J_{L,L-1}(r) - \sqrt{L+1}\left(\frac{d}{dr} + \frac{L+2}{r}\right)J_{L,L+1}(r) \quad (2.19)$$

Using this relation the transverse electric form factor can be rewritten as,

$$F_L^E(q) = -\sqrt{\frac{L+1}{L}}\frac{\omega}{qc}F_L^C(q) - \frac{\hat{L}\hat{J}_f}{\sqrt{L}\hat{J}_i} \int J_{L,L+1}(r)j_{L+1}(qr)r^2 dr \quad (2.20)$$

The longitudinal and transverse electric form factors are then expressed in terms of the densities  $\rho_L$  and  $J_{L,L+1}$  alone.

From Eq. (2.12) it is clear that only  $|F_L^E(q)|^2$  is determined by measuring the cross sections. There are two possible currents  $J_{L,L+1}$ , differing in size and shape, which yield the same cross-sections. Even if both forward and backward scattering are measured this ambiguity will persist. The choice of current must be guided by other considerations.

#### Distorted Wave Born Approximation

The PWBA is a good approximation only for scattering from low  $Z$  nuclei. For higher  $Z$  nuclei the electron wavefunction is distorted by the coulomb field of the nucleus. The Distorted-Wave Born Approximation (DWBA) uses electron wavefunctions which are solutions to a Dirac equation with a coulomb potential due to the ground state nuclear charge distribution. The nuclear excitation is still treated as a one-photon exchange (ie. in the first Born Approximation) but the interaction of the electron with the static field of the nucleus is treated exactly.

The derivation of the DWBA cross section has been given many times.<sup>[15-17]</sup> It will suffice here to point out the essential differences with the PWBA.

In the DWBA a strict separation of the longitudinal (charge) and transverse (current) form factors is not possible. By this it is meant that a factorization such as in equation (2.12) does not occur. The DWBA cross section for a transition of a single multipolarity,  $L$ , is given by,

$$\left(\frac{d\sigma}{d\Omega}\right)_{DWBA} = \frac{E_f^2}{(2\pi)^2} \sum_{Mmm'} \frac{1}{2J_i + 1} |A_{if}(LMmm')|^2 \quad (2.21)$$

where  $A_{if}$  is the matrix element of the interaction Hamiltonian between the initial and final nuclear states. No factorization of  $A_{if}$  can separate the transverse from the longitudinal contributions. The main result other than the extra computational difficulties is that DWBA form factors are not simply related to the underlying nuclear transition densities. Since the transition densities contain the nuclear structure information we have taken them as the fundamental quantity to be extracted rather than the form factors.

Another difference between the PWBA and DWBA leads to the use of an effective momentum transfer when displaying data. Because of the attraction between the electron and the nucleus the electron is accelerated as it nears the nucleus. Another way of stating this is to say that for the distorted electron wavefunction the local wavenumber is not constant as for a plane-wave, but rather is larger near the nucleus. The result is that the interaction with the nucleus occurs at a larger incident momentum (and therefore a larger momentum transfer) than would be given by the asymptotic kinematics. The effective momentum transfer can be approximated for spherical nuclei as,

$$q_{eff} = q \left(1 + \frac{4}{3} \frac{Z\alpha}{E_i R}\right) \quad (2.22)$$

where  $R$  is the equivalent hard-sphere radius of the nucleus. This has been approximated as  $1.2 \times A^{1/3} fm$ . All calculations presented here have been done in the full DWBA.

## 2.3 RADIATIVE CORRECTIONS

There are many references on the subject of radiative corrections<sup>[12,18,19,20]</sup>. The purpose of making these corrections is to unfold the contributions to the experimental cross sections which are a result of processes other than the single-photon exchange discussed in the previous section. A brief review of the processes and how they enter the experimental cross section is given here.

### Geometry and Terminology

*Figure 2.3* shows a scattering event inside an experimental target. We will make a distinction between internal and external processes. Internal processes result from the electron being in the field of the particular nucleus with which the main scattering occurs (region II in *fig. 2.3*). The external processes occur in regions I and III and are a result of the electron passing through the target material.

### Internal Processes

The internal effects which have been considered in this analysis are represented by the diagrams shown in *fig. 2.4*. Diagrams *a* and *b* involve the emission of real photons as small angle bremsstrahlung radiation. Diagrams *c* - *e* involve the emission and reabsorption of virtual photons and lead to a mass renormalization for the electron. The vacuum polarization diagram *f* leads to a charge renormalization. The correction due to the interference of the terms *c* - *f* with the first Born Approximation (*fig. 2.1*) is known as the Schwinger correction. The size of the internal correction for the potential scattering scales with the first Born cross section and it is this fact that allows the corrections to be made.

### External Processes

The external processes which have to be accounted for are electron-electron collisions (including ionization) and small angle bremsstrahlung scattering. In traversing the target an electron will interact with the atomic electrons causing

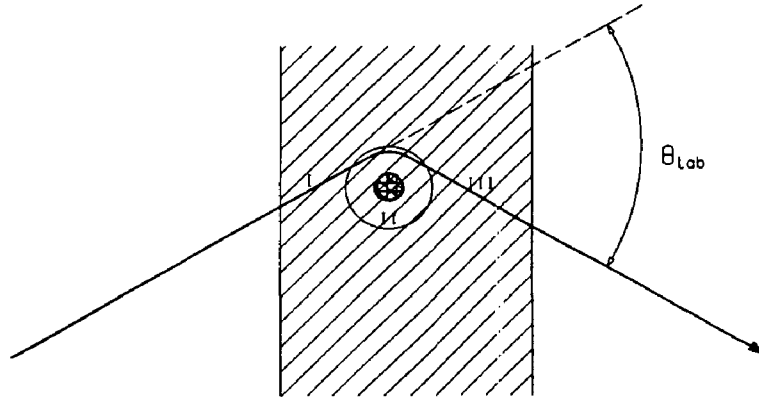


**Figure 2.3** Geometry for radiative processes. Regions I and III in the figure indicate where 'external' radiative processes occur. Region II is the volume of the target where an electron is under the influence of the nucleus with which the Born scattering occurs. The radiative processes which occur in region II are referred to as 'internal'.

ionizations and losing energy. This effect is referred to as Landau straggling. An electron can also interact with the coulomb field of a nucleus or an atomic electron and emit Bremsstrahlung radiation as it is deflected.

#### Total Radiative Correction

The total radiative correction is given as a combination of the processes which occur in all three regions shown in *fig. 2.3*. A theoretical electron energy distribution due to radiative processes can be calculated. This distribution will be a convolution of the distributions for the regions I, II, and III.

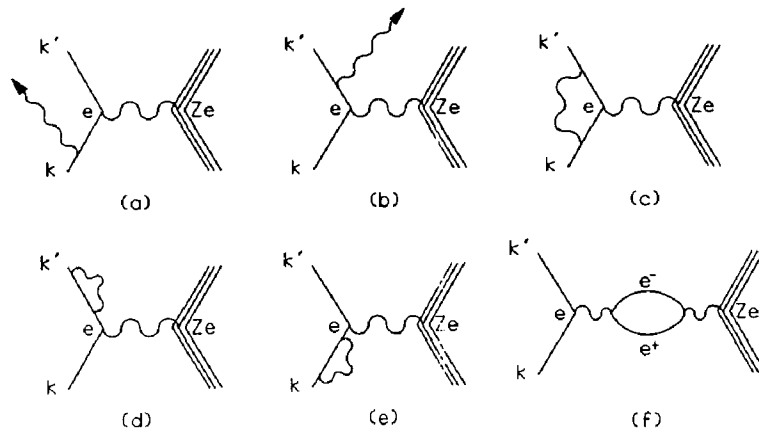


**Figure 2.4** Scattering diagrams for the internal radiative processes accounted for in the analysis.

### 3. Data Collection

The data for this experiment was collected on the Energy-Loss Spectrometer System (ELSSY) at the William H. Bates Linear Accelerator Center. The data taking occurred during a period beginning in December of 1982 and ending in April of 1985. During this period no major changes in the data collection facilities occurred.

#### 3.1 THE MIT-BATES ELECTRON SCATTERING FACILITY

Various aspects of ELSSY have been presented elsewhere<sup>[22-24]</sup> in greater detail than will be discussed here. The following overview is presented mainly for a reader unfamiliar with the laboratory. The laboratory is administered by MIT and funded primarily through the Department of Energy. The general layout of the facility is shown in *fig. 3.1*.

##### Accelerator, Beam Switchyard, Scattering Chamber, and Spectrometer

The linear accelerator at Bates produces a pulsed electron beam of variable energy and intensity. The energy can be varied continuously in the range of approximately 50-400 MeV. Average currents of 25-35  $\mu\text{A}$  are routinely achieved and under favorable conditions average currents of more than 60  $\mu\text{A}$  have been obtained. A typical beam structure is 12  $\mu\text{s}$  pulses, with peak currents of 6 mA and a repetition rate of 360 hz.

After the beam leaves the accelerator it is brought to a focus at an object point. This focus ideally serves to uncouple the accelerator from the beam switchyard (BSY) so that steering and focusing adjustments made in the accelerator do not affect the 'quality' of the beam on the target. Between the object point and the focal plane the imaging is roughly of unit magnification.

The BSY transports the beam from the object point to the scattering chamber and also performs numerous functions essential for taking good data. Briefly these are: selecting a range of beam energy components, focusing these individual

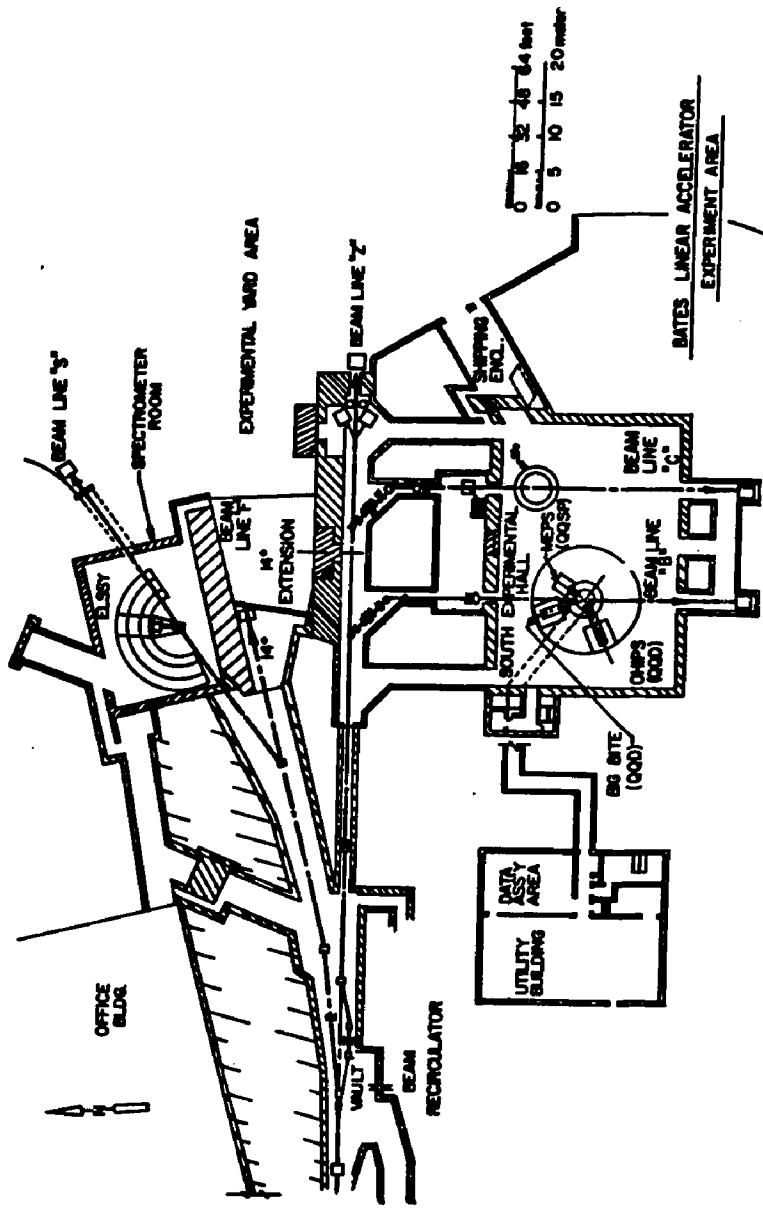


Figure 3.1 General layout of the MIT-Bates facility.

energy components on the target, dispersing these components on the target, and matching this dispersion to that of the spectrometer.

Just upstream from the scattering chamber two toroids measure the beam current. The signal from these toroids is fed into integrating amplifiers which can measure the current to one part in  $10^3$ . The two integrators are periodically calibrated to maintain accuracy.

The scattering chamber is connected directly to the beam pipe which comes from the BSY. The scattering chamber is also connected to the spectrometer and a large diameter exit pipe which leads to a shielded beam dump. During an experiment the entire system is evacuated to approximately  $10^{-5}$  torr. Facilities exist for transferring targets to the scattering chamber under a controlled environment (dry argon or vacuum). Several targets can be mounted in the chamber at once and a given target and target angle can be selected remotely. The scattering chamber is connected to the spectrometer by a sliding seal which in principle allows the spectrometer angle to be varied without breaking vacuum. In practice the targets are moved into a sealed environment and the scattering chamber is backfilled with dry nitrogen during angle changes.

The 900 MeV/c energy-loss spectrometer is a  $90^\circ$  split-pole design. *Figure 3.2* shows a diagram of the spectrometer. The maximum solid angle of acceptance is  $5 \text{ msr}$  with a  $\pm 5\%$  momentum bite. The optics are discussed in some detail in Bertozzi, et al.<sup>[22]</sup> and are a combination of point-to-point in the momentum direction and parallel-to-point in the transverse direction (*i.e.* perpendicular to the momentum direction.) The focal surface is inclined at  $45^\circ$  to the central ray as shown in *fig. 3.2* and is curved in the transverse direction. The design resolution of  $\frac{\Delta p}{p} = 1 \times 10^{-4}$  is routinely achieved and often exceeded.

#### Focal Plane Instrumentation

The focal plane instrumentation consists of two vertical drift chambers (VDC-I and VDC-II), two transverse arrays connected in series (TA), two Čerenkov



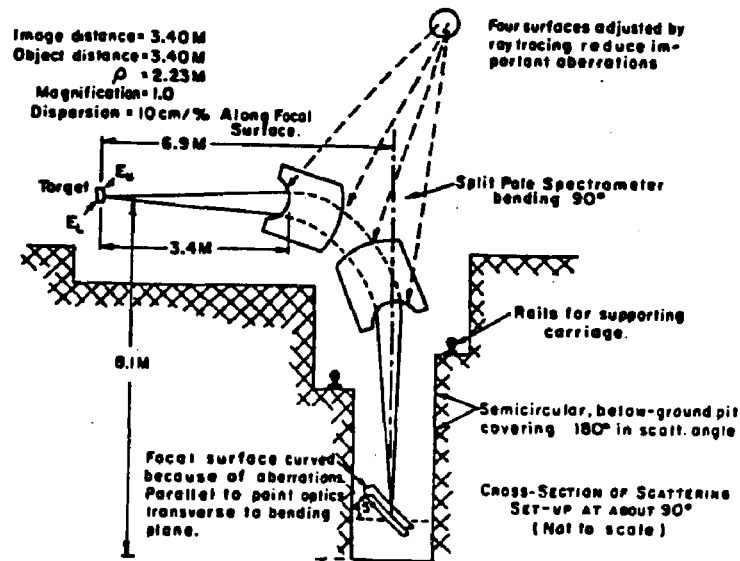
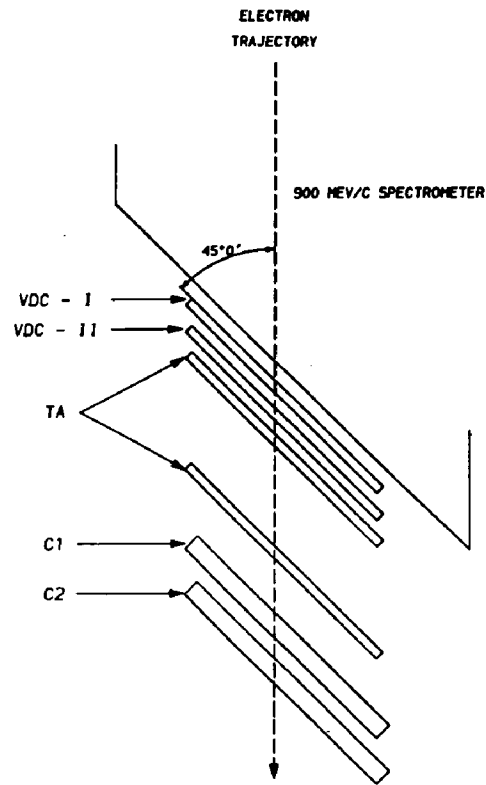


Figure 3.2 Cutaway of the spectrometer, target, and focal plane instrumentation at Bates.

detectors ( $\check{C}1$  and  $\check{C}2$ ), and the associated readout electronics. The instrumentation covers roughly half the spectrometer exit aperture giving a 6% useable momentum bite. The instrumentation is located outside of the vacuum and is separated from the spectrometer vacuum by a thin kevlar-reinforced mylar window<sup>[24]</sup>. The position of VDC-I corresponds roughly to the position of the focal surface. This arrangement is shown in *fig. 3.3*.

Shielding from background radiation is provided by two means. First the focal plane instrumentation is located roughly 7 meters below the beamline as shown in *fig. 3.2*. The pit can be covered with concrete blocks when additional shielding



**Figure 3.3** The focal plane instrumentation consists of five detectors: VDC-I, VDC-II, TA, Č1, and Č2.

is necessary. In addition 6 inch iron doors enclose the area occupied by the detectors.

The focal plane instrumentation is designed to allow reconstruction of the tracks of electrons which have passed through the spectrometer and to reject background events. The readout electronics are all gated on the accelerator gun to minimize background. Electron events are identified by requiring a coincidence between Č1 and Č2, the two Čerenkov detectors. This coincidence signal is in turn used to start the readout of VDC-I, VDC-II, and the TA. These four chambers are used to define the track.

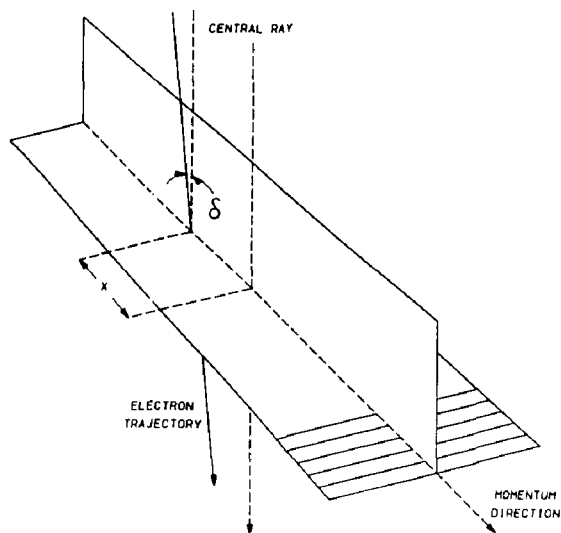


**Figure 3.4** Quantities measured by a VDC.

The VDC's are multi-wire proportional chambers (MWPC's) constructed with wires parallel to the lines of constant momentum, ie. perpendicular to the momentum direction. The signals from chamber are used to determine a position along the momentum direction, it  $x$ , and a vertical angle,  $\delta$  for each electron event as shown in *fig. 3.4* . The two chamber arrangement increases the accuracy with which these quantities (most importantly the vertical angle) can be measured. The combined two VDC readout is capable of measuring  $x$  to 0.12 mm FWHM and  $\delta$  to 17 mrad FWHM<sup>[29,24]</sup> . Some specifics of the readout system are given in Appendix A.

The TA is composed of two MWPC's which have been constructed with wires roughly parallel to the momentum direction. The readout system and geometry of the construction enable the TA to measure a displacement in the

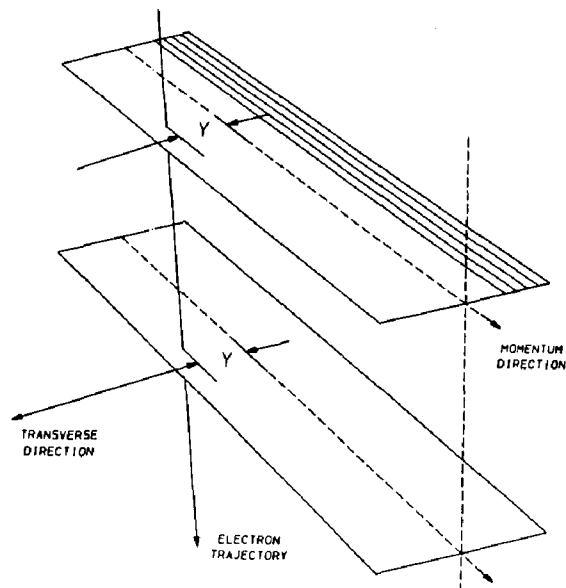


**Figure 3.5** Quantities measured by the transverse array.

transverse direction. No transverse angle is measured but the TA's are wired to eliminate tracks with transverse angles differing significantly from zero and thus are important in reducing background. This transverse angle restriction is accomplished by separating the two chambers which form the TA and requiring a coincidence between wires at a common transverse displacement. This is shown in *fig. 3.5*. The intersection of the two planes, one defined by the VDC's and one defined by the TA determines the electron track.

#### On-line Data Processing

The on-line data processing at Bates is done using a PDP-11/45 computer. Data acquisition is accomplished with a CAMAC based system which is interfaced to the computer using a Bi-Ra Multi-Branch Driver (MBD). The on-line

Isotopic Analysis	
Mo Isotope	Atomic %
92	97.37 ± 0.10
94	0.68 ± 0.10
95	0.52 ± 0.10
96	0.37 ± 0.10
97	0.18 ± 0.10
98	0.40 ± 0.10
100	0.50 ± 0.10

**Table 3.1** Data from ORNL isotopic analysis of the target.

data processing is extensive and more details are presented in Appendix A. Each 'event' must pass a series of tests to insure that it is indeed due to an electron which has scattered into the spectrometer. The track is reconstructed then corrections are applied for kinematics and spectrometer aberrations. Events are binned to form a 6144 channel spectrum. In addition, a considerable amount of diagnostic information is stored with each run. The ability to do event-by-event data collection exists but was not used for this experiment. Since only the preprocessed data are stored with each run it is important that the on-line processing be done correctly and considerable time is spent during each run to insure that this is the case.

### 3.2 TARGETS

For this experiment two molybdenum targets with thicknesses of 5.8 and 19.4  $mg/cm^2$  were purchased from Oak Ridge National Laboratories (ORNL). The targets were isotopically enriched to 97.4%  $^{92}Mo$  from the natural abundance of 14.8%. The data from the ORNL specification sheet are shown in *table 3.1*. During the analysis of the data several isotopic impurities were identified but did not cause difficulty in the analysis.

In addition to the  $^{92}Mo$  targets there were always energy calibration targets (either BeO or BeAl),  $^{12}C$  targets, and at least one other target on which data

was being taken. Data for several isotopes with significantly different masses are necessary for energy calibrations and were used whenever possible. The  $^{12}\text{C}$  targets were also used to help establish normalizations.

### 3.3 KINEMATICS

To reconstruct transition densities in a model-independent way one needs data covering a  $q$ -range up to about twice the fermi-momentum or about  $3 \text{ fm}^{-1}$ . In this range the spacing of data points should be adequate to map out the details of the form-factor. A spacing of  $0.15\text{--}0.20 \text{ fm}^{-1}$  proves to be adequate in most cases. These general considerations along with the experimental restrictions imposed by the facility ( $\theta_{lab} \geq 35^\circ$  and  $E_{lab} \leq 380 \text{ MeV}$ ) were used to determine the kinematics points taken.

#### Energy Calibrations

Incident electron energies are in principle determined by a bending magnet located in the BSY. In practice the beam energy is measured by scattering from calibration targets.

Electron scattering form factors can be expressed in terms of a single kinematic variable,  $q$ , the four-vector momentum transfer. The variable  $q$ , can be expressed as a function of the scattering angle,  $\theta$ , and the magnitudes of the initial and final electron energies,  $E_i$  and  $E_f$ , as given in eq. (2.6). Expressing the final energy in terms the initial energy,  $E_i$ , and the excitation energy,  $\omega$ , we have (to first-order in  $\omega$ ),

$$E_f = (E_i - \omega)\eta, \quad (3.1)$$

and,

$$q = 2[E_i(E_i - \omega)]^{1/2} \eta^{1/2} \sin \frac{\theta}{2}. \quad (3.2)$$

The recoil factor depends on the mass of the target nucleus,  $M_t$ , and is given in eq. (2.5).

A determination of  $q$  can be made by measuring the recoil energy difference between the elastic peaks of two nuclei of different masses. This energy difference is given by,

$$\Delta_{12} = E_i |\eta_1 - \eta_2|. \quad (3.3)$$

For  $E_i/M_t c^2 \ll 1$  this gives,

$$\Delta_{12} \simeq 2 q^2 \left| \frac{1}{M_1} - \frac{1}{M_2} \right| \quad (3.4)$$

If the two masses and  $\Delta_{12}$  are known,  $q^2$  can be found.

Although the form factors can be expressed in terms of  $q$  alone, the cross-sections have explicit energy dependence as well. It is therefore important that an accurate determination of the incident electron energy be made. Once  $q$  has been determined the incident beam energy can be determined if the scattering angle is known. The scattering angle has two components which can be controlled by the experimenter. The reference for both components is the surveyed axis of the incident beam line. The first component is the angle at which the spectrometer is set relative to this axis. If the surveying has been done correctly this component can be determined within 0.5 milliradians and the error in  $\theta$  can be ignored. The other component is the angle the incident beam actually makes with the surveyed axis. A scintillation target placed downstream from the primary target allows the experimenter to check centering at both targets which should insure that beam is on axis. This was checked after each energy change but only rarely more than that and as a result the error introduced into the scattering angle by this component is not known. Here it has been assumed that the scattering angle is known and the measurement of  $\Delta_{12}$  yields both  $q$  and  $E_i$ . *Table 3.2* contains the results of this energy calibration procedure for the forward scattering part of the experiment. *Table 3.3* contains a similiar summary for the backward scattering data.

Energy Calibration Data - Forward Scattering					
$\theta$	$E^*$	Isotope 1	Isotope 2	$\Delta_{12}$	E
45.0	190	<sup>142</sup> Ce	<sup>16</sup> O	0.625	189.7 ± 0.3
45.0	190	<sup>92</sup> Mo	<sup>16</sup> O	0.584	190.1 ± 0.2
45.0	190	<sup>16</sup> O	<sup>9</sup> Be	0.543	189.8 ± 0.3
54.8	190	<sup>142</sup> Ce	<sup>16</sup> O	0.901	189.6 ± 0.2
54.8	190	<sup>16</sup> O	<sup>9</sup> Be	0.778	189.3 ± 0.3
65.0	190	<sup>142</sup> Ce	<sup>16</sup> O	1.228	189.8 ± 0.2
65.0	190	<sup>16</sup> O	<sup>9</sup> Be	1.057	189.5 ± 0.3
76.0	190	<sup>142</sup> Ce	<sup>16</sup> O	1.604	189.5 ± 0.2
76.0	190	<sup>16</sup> O	<sup>9</sup> Be	1.380	189.6 ± 0.3
88.0	190	<sup>142</sup> Ce	<sup>16</sup> O	2.039	189.7 ± 0.2
88.0	190	<sup>16</sup> O	<sup>9</sup> Be	1.745	189.6 ± 0.3
101.0	190	<sup>16</sup> O	<sup>9</sup> Be	2.169	191.1 ± 0.2
40.0	280	<sup>142</sup> Ce	<sup>16</sup> O	1.082	279.4 ± 0.2
40.0	280	<sup>27</sup> Al	<sup>9</sup> Be	1.428	278.8 ± 0.3
92.8	100	<sup>27</sup> Al	<sup>9</sup> Be	0.818	100.0 ± 0.2
40.0	370	<sup>16</sup> O	<sup>9</sup> Be	1.595	365.0 ± 1.0
40.0	370	<sup>142</sup> Ce	<sup>16</sup> O	1.847	365.3 ± 1.0
90.0	100	<sup>16</sup> O	<sup>9</sup> Be	0.855	104.6 ± 0.2
75.0	100	<sup>27</sup> Al	<sup>9</sup> Be	0.633	104.4 ± 0.2
75.0	130	<sup>208</sup> Pb	<sup>12</sup> C	1.053	130.4 ± 0.3
40.0	370	<sup>16</sup> O	<sup>9</sup> Be	1.614	367.1 ± 1.0
40.0	370	<sup>86</sup> Sr	<sup>16</sup> O	1.666	362.3 ± 1.0
45.0	370	<sup>16</sup> O	<sup>9</sup> Be	1.986	364.7 ± 0.3
45.0	370	<sup>86</sup> Sr	<sup>16</sup> O	2.050	359.4 ± 1.5
45.0	370	<sup>86</sup> Sr	<sup>28</sup> Si	1.011	366.2 ± 1.3
50.0	370	<sup>86</sup> Sr	<sup>16</sup> O	2.550	363.4 ± 1.5
50.0	370	<sup>86</sup> Sr	<sup>28</sup> Si	1.221	364.6 ± 0.6
56.0	370	<sup>86</sup> Sr	<sup>28</sup> Si	1.510	365.4 ± 0.6
60.0	370	<sup>16</sup> O	<sup>9</sup> Be	3.360	365.6 ± 0.5
72.0	370	<sup>16</sup> O	<sup>9</sup> Be	4.639	367.7 ± 1.5
79.5	370	<sup>16</sup> O	<sup>9</sup> Be	5.502	366.7 ± 1.0

**Table 3.2** Energy calibration data for the forward scattering part of the experiment. The calibration data are grouped to reflect constant accelerator energies. All the energy variables are given in units of MeV. The uncertainty in the calibrated energy is due to the statistical uncertainty in fitting the peak positions in the calibration data.



Energy Calibration Data - Backward Scattering					
$\theta$	$E^*$	Isotope 1	Isotope 2	$\Delta_{12}$	E
155.0	125	$^{16}\text{O}$	$^9\text{Be}$	1.499	$125.7 \pm 1.0$
150.0	175	$^{16}\text{O}$	$^9\text{Be}$	2.801	$175.1 \pm 1.0$
65.0	240	$^{16}\text{O}$	$^9\text{Be}$	1.680	$239.6 \pm 1.5$
65.0	240	$^{16}\text{O}$	$^9\text{Be}$	1.683	$239.8 \pm 1.5$
65.0	220	$^{16}\text{O}$	$^9\text{Be}$	1.409	$219.2 \pm 0.8$
55.0	260	$^{16}\text{O}$	$^9\text{Be}$	1.457	$259.0 \pm 1.5$
75.0	205	$^{16}\text{O}$	$^9\text{Be}$	1.568	$204.6 \pm 0.7$
75.0	205	$^{27}\text{Al}$	$^9\text{Be}$	2.411	$204.9 \pm 0.4$
75.0	160	$^{16}\text{O}$	$^9\text{Be}$	0.499	$159.5 \pm 0.5$
60.0	140	$^{16}\text{O}$	$^9\text{Be}$	0.499	$139.4 \pm 0.6$
40.0	290	$^{16}\text{O}$	$^9\text{Be}$	1.007	$289.5 \pm 1.5$
40.0	290	$^{16}\text{O}$	$^9\text{Be}$	1.014	$290.0 \pm 0.8$
50.0	230	$^{16}\text{O}$	$^9\text{Be}$	0.960	$229.1 \pm 0.7$
160.0	80	$^{16}\text{O}$	$^9\text{Be}$	0.636	$80.4 \pm 0.5$
70.0	100	$^{16}\text{O}$	$^9\text{Be}$	0.340	$100.3 \pm 1.5$
70.0	100	$^{16}\text{O}$	$^9\text{Be}$	0.341	$100.4 \pm 1.5$

**Table 3.3** Energy calibration data for the backward scattering part of the experiment. The calibration data are grouped to reflect constant accelerator energies. All the energy variables are given in units of MeV. The uncertainty in the calibrated energy is due to the statistical uncertainty in fitting the peak positions in the calibration data.

### Forward Scattering Kinematics

The forward scattering data were taken by doing angle sweeps at five different energies. The data sets overlap in  $q$ -range to help insure proper normalization. When possible energy calibrations were done at more than one angle of a sweep to check the calibration. *Table 3.4* summarizes the kinematics for the forward scattering data set.

### Backward Scattering Kinematics

For the backward scattering data the momentum transfer was varied by changing the energy rather than making an angle sweep at a fixed energy. At each energy the spectrometer was first set at a forward angle to allow the switchyard optics to be tuned and to do energy calibration and normalization runs. This is

Forward Scattering Kinematics	
$\theta$	$E_i$ (MeV)
40.0	104.5 ± 0.4
60.0	104.5 ± 0.4
75.0	104.5 ± 0.4
90.0	104.5 ± 0.4
75.0	130.4 ± 0.4
45.0	189.6 ± 0.4
54.8	189.6 ± 0.4
65.0	189.6 ± 0.4
76.0	189.6 ± 0.4
88.0	189.6 ± 0.4
101.0	191.1 ± 0.4
40.0	279.1 ± 0.6
75.3	279.1 ± 0.6
88.4	279.1 ± 0.6
97.1	279.1 ± 0.6
40.0	365.1 ± 2.0
74.7	365.1 ± 2.0
80.5	365.1 ± 2.0
40.0	366.7 ± 2.0
50.0	366.7 ± 2.0
79.5	366.7 ± 2.0
87.0	366.7 ± 2.0
95.5	366.7 ± 2.0
105.0	366.7 ± 2.0

Backward Scattering Kinematics	
$\theta$	$E_i$ (MeV)
160.0	80.4 ± 0.5
155.0	100.3 ± 1.5
155.0	125.7 ± 1.0
155.0	139.4 ± 0.6
155.0	159.5 ± 0.5
150.0	175.1 ± 1.0
155.0	189.6 ± 0.6
155.0	204.8 ± 0.7
155.0	219.2 ± 0.8
155.0	239.7 ± 1.5
155.0	259.0 ± 1.5
155.0	289.8 ± 1.5

**Table 3.4** Summary of kinematics determined for this experiment. The uncertainty in the energy reflects the variation of the calibration as well as the statistical uncertainty.

done to save time since the counting rates at backward angles are often very small. The spectrometer was then moved to the backward angle, in principle leaving all other conditions unchanged. For the lowest q-points ( $E_i \simeq 80, 100, 125$  MeV) it was also possible to do energy calibrations at the backward angle. Table 3.4 shows the kinematics for the backward scattering data set.

## 4. Data Reduction – Cross Sections

Extracting reliable cross sections from the data is an involved and time-consuming process. This chapter outlines the procedures that were used in this process.

### 4.1 DATA FILES

The data files produced by the data acquisition program contain hardware scalers (integrator ‘clicks’, the number of pulses on Č1, Č2, VDC delay lines, etc.), software scalers (counters of events, ‘good’ events, missing-hit events, etc.), parameters used in the on-line sorting, diagnostic histograms and data histograms. The data histograms containing the number of counts (electron events) per channel are stripped from the data file. If several data files have been taken for a single q-point, the data histograms are combined. The program which combines files accounts for small shifts (an integral number of channels) which might have occurred between runs. This program also averages apertures and corrections which are specific to a single data file and allows for rebinning of the data by simply adding together groups of channels. The resulting file is used as input for the peak shape fitting code. The remaining information in the data files is used to make corrections to and diagnose problems with the data histograms.

### 4.2 PEAK-SHAPE FITTING CODE

The cross sections presented in the thesis were calculated using the program ALLFIT which was obtained from MIT.<sup>[25]</sup> The distinguishing feature of this code is the multiparameter peak-shape option which is an invaluable aid in fitting high-resolution data. Several sections of ALLFIT are taken from previous fitting codes. In particular the radiative corrections follow the work of Bergstrom,<sup>[19]</sup> Creswell,<sup>[20]</sup> and Deady.<sup>[21]</sup> Some aspects of the fitting code which affect the reliability of the data are discussed below.

ALLFIT establishes a mapping between bins of the data histograms and reaction Q-values (or excitation energy if desired) based on the location of known peaks. This mapping has traditionally been established by a separate program which models the focal plane of the spectrometer fitting parameters of the model to peak location data. When the statistics are adequate the mapping established by ALLFIT proved very reliable and avoided some of the ambiguities associated with the focal plane modelling programs. When the statistics on known levels was poor both methods of determining this mapping were used to insure a consistent and accurate description. If the position of a known level was allowed to vary, the fitted excitation energy was always within a few keV of the nominal position.

The peak shape fit to the data is a hypergaussian (a gaussian generalized so that the power to which the exponent is raised not restricted to 2) with exponential tails on the right and on the left. (Here left and right are in the same sense as *fig. 4.1*, *i.e.* right being the direction of greater inelasticity.) This shape has ten adjustable parameters: position, height, width, asymmetry, exponent, and five parameters describing the right and left tails. The characteristic peak shape of electron scattering data has a large tail extending toward the higher inelasticity end of the spectrum as shown in *fig. 4.1*. The radiation tails have been fit in one of two ways depending on the statistics of the histogram. When the tail is well defined as in *fig. 4.1*, the right exponential tail is merely adjusted to fit the data. The radiative correction is then made by integrating the peak shape out to some cut-off excitation energy. A correction based on integrating the theoretical peak shape out to the same cut-off is then applied. This correction is calculated for three different cut-off energies as a check of this procedure since the cutoff value is arbitrary. Alternatively the theoretical tail distribution can be calculated directly and convoluted with the peak shape before fitting. In this case the integral of the central peak shape (before convolution) gives the corrected cross-section. The later method is more reliable when the radiative tail is not well determined by the data but also takes considerably more computer time.

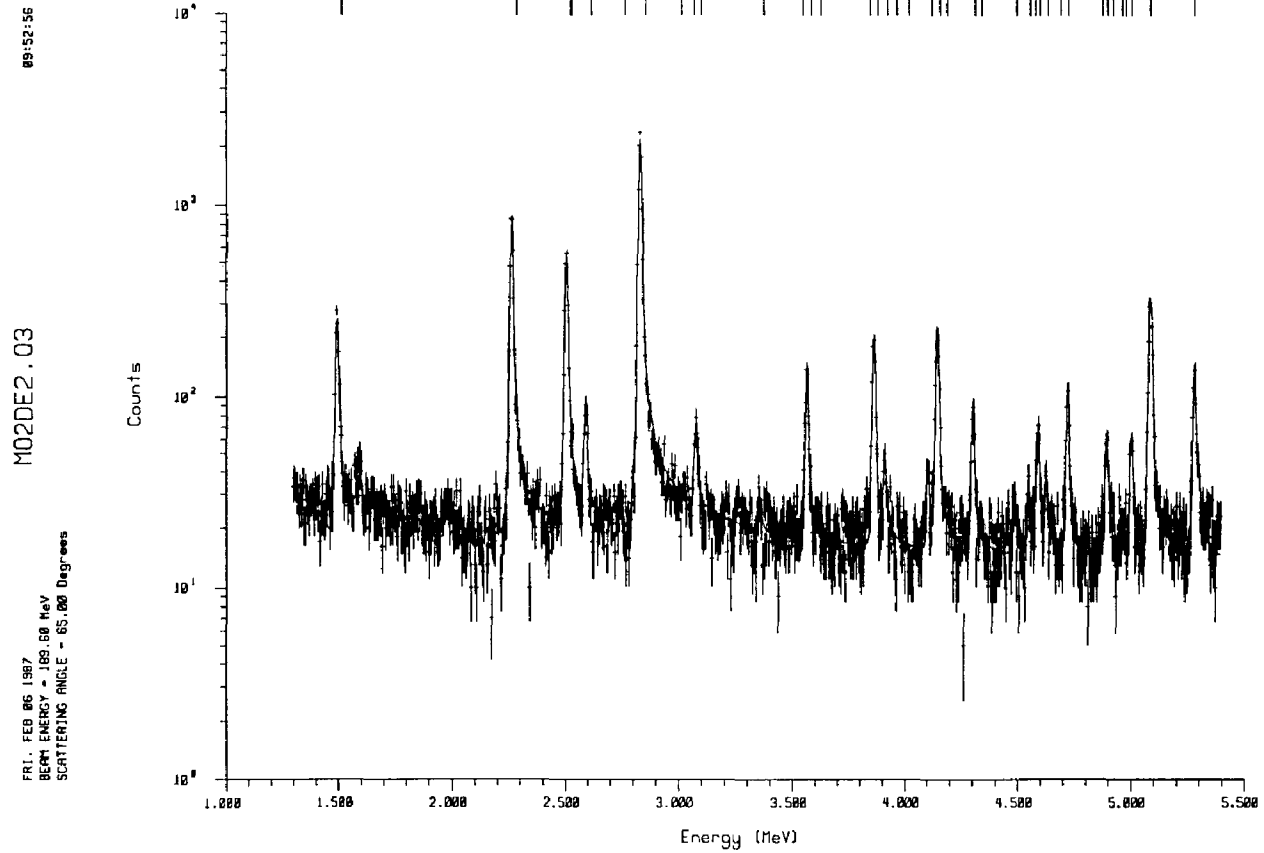


**Figure 4.1** Spectrum of inelastically scattered electrons for an incident energy of 189.6 MeV and a scattering angle of  $65.0^\circ$ . The solid curve is the result of a peak-shape fit. The known excited states are shown above the fit.

To fit background contributions to a histogram ALLFIT uses a sum of two polynomials. For our data it was only necessary to use a single polynomial with at most quadratic dependence on channel number.

The fitting procedure itself is based on the method of maximum likelihood assuming Poisson statistics. A standard Marquart search algorithm<sup>[27]</sup> is used in finding the optimum parameters. A quantity equivalent to  $\chi^2$  is calculated and used as a goodness of fit criteria. This quantity is used mainly as a guideline and only the statistical errors which result from the fit have been used.

#### 4.3 CORRECTIONS TO THE DATA

Several corrections are applied to the data while extracting cross sections. All of these corrections are applied uniformly to a spectrum, *i.e.* no channel dependent corrections were made to our data. The usual assumption is that except near the ends of the wire chambers the focal plane instrumentation has a uniform efficiency which is very near to 100%. Small scale (channel-to-channel) variations in efficiency are known to exist but tend to average out over several runs where the spectrum may shift by small amounts. In practice the assumption of uniform efficiency is justified only by discarding data sets where the non-uniformity shows up in diagnostic spectra or unreasonable cross sections. A more systematic procedure for dealing with efficiencies would greatly improve the reliability of the data.

##### Hardware Deadtime Correction

This correction accounts for data rates exceeding the the rate at which the data acquisition system can record and process the data. When the acquisition electronics receives a valid start it begins recording information. If the electronics are unable to accumulate a complete set of information on this potential event all the information (except the occurrence of a start) is discarded. For example if two starts occur within 300 ns of each other the pulses on the delay lines will

not be separable. The system stops trying to record information and waits for the next start. The hardware correction applied is given by,

$$HDTC = \frac{\text{starts}}{\text{events}}, \quad (4.1)$$

where an event is a start followed by a successful collection of a complete set of information. (Note that an event is not necessarily a good event.) This correction assumes each start is a potentially valid event and that the number of good events scales with the number of events. The improvement in consistency that this correction makes, even when it is very large, supports the validity of these assumptions.

#### Software Corrections

There are other reasons besides high data rates which cause good events to be eliminated from the data histograms. The data acquisition code will discard events for which the information gives an inconsistent or unphysical track. The electron track maybe due to background or may be a good event for which the information has been corrupted because either the signal is weak or because of background. The corrections which account for these discarded good events are loosely referred to as software corrections.

Events for which a complete set of information is accumulated in a temporary buffer in the MBD. When the buffer is full it is sent to the PDP-11/45 and the events are processed while more data are recorded. The data acquisition program first analyzes the data corresponding to the single VDC system (VDCI + TA). One correction factor, SCF1, corrects for good events which are lost in this process. Events which survive the one-chamber analysis are then processed further using information from VDCII to refine the vertical angle and aberrative corrections. A second factor, SCF2, corrects for good events lost in this process. The general form of both corrections is given by,

$$SCF = \frac{\text{good events} + \text{discarded good events}}{\text{good events}} \quad (4.2)$$

Processing for the one-chamber system first classifies all events into one of four groups: *rollovers*, *inconsistent hits*, *missing hits*, and *four-hit events*. These terms are explained in more detail in Appendix A. The *rollovers* are merely counted then discarded. Events with no consistent VDC hits are also counted and discarded. The remaining events all have at least one VDC hit which is consistent and coarse channel numbers and drift times can be calculated for these events. Coarse spectra are formed of the *missing hit events* and *inconsistent hit events* before they are also discarded. An exception is made for events which have good hits on all three VDC delay lines (ie. *missing TA only* and *inconsistent TA only* events). These events are processed further along with the *four-hit events* but do not enter the final data histograms. The remaining cuts on the *four-hit events* insure that the electron track is due to an electron which scattered from the target through the spectrometer aperture. The factor SCF1 is given by,

$$\text{SCF1} = ( \text{events in one chamber spectrum} + \\ \text{inconsistent side delay line events} + \\ f_1 \times \text{discarded four hit events} + \\ f_2 \times \text{good but missing TA events} + \\ f_3 \times \text{missing hits events} ) / \text{events in one chamber spectrum} \quad (4.3)$$

The *discarded four-hit events* do not include any *inconsistent side delay line events*. The fractions  $f_1$ ,  $f_2$ , and  $f_3$  are determined by fitting a function of the form,

$$h(x) = A_0 + A_1 \times g(x) \quad (4.4)$$

to the appropriate diagnostic spectrum. Here  $g(x)$  is the coarse spectrum of *good events* scaled to unit area,  $x$  is coarse channel number and  $A_0$  and  $A_1$  are determined in a least-square fit. The parameters  $A_0$  and  $A_1$  determine the fraction of the discarded events which have the same momentum distribution as the good events. All the *inconsistent side delay-line events* are assumed to be good. This assumption is based on two observations from our data: 1) A large



percent of the four-hit events (usually greater than 90%) are good events, 2) The fraction of this inconsistent side delay-line events which are good cannot be easily determined at present. This assumption leads to an overprediction of the correction factor. It is important to note here that the inconsistent side-delay line events are usually the dominant contribution to SCF1.

The correction factor for the two-chamber spectrum has a simpler form given by,

$$\text{SCF2} = \left( \frac{\text{events in two chamber spectrum} + f_4 \times \text{discarded two chamber events}}{\text{events in two chamber spectrum}} \right) \quad (4.5)$$

Again  $f_4$  is determined by fitting a diagnostic spectrum. It is assumed that the events which pass all the tests for the one-chamber system are good events. The total software correction factor is given by,

$$\text{SCF} = \text{SCF1} \times \text{SCF2} \quad (4.6)$$

#### 4.4 NORMALIZATIONS

Although considerable effort is spent in determining corrections to our data we have not tried to measure absolute cross sections. All the data presented were normalized using the procedure outlined below. These normalizations correct for errors in target thickness, beam current integration, solid angle readout, and also inefficiencies in the detectors.

##### Forward Scattering Data

Normalizations were based on previous elastic scattering measurements<sup>[28-30]</sup> and on muonic  $x$ -ray studies.<sup>[81]</sup> A fit to a subset of these data was performed using the program MEFIT which was originally developed at Mainz. This program now allows for the inclusion of the muonic atom data input in the form

Low-q Elastic Scattering Parameterisation		
$n$	$A_n$	$\delta A_n$
1	0.153037280	0.000019845
2	0.098567069	0.000136710
3	-0.016808402	0.000213570
4	-0.029901061	0.000110460
5	0.002969925	0.000068775
6	0.008109359	0.000136080
7	-0.000110985	0.000443940
8	-0.001078560	0.000851760
9	0.000176715	0.000619920
10	0.000072450	0.000318150

**Table 4.1** Fourier-Bessel Coefficients for the fit to the low-q scattering and muonic data only.

of Barrett moments which were taken from Schellenberg, *et al.*<sup>[31]</sup>. The fitting of the electron scattering data follows the procedures as described by Dreher, *et al.*<sup>[32]</sup> The previous electron scattering data cover a momentum transfer range of 0.5 to 2.1  $fm^{-1}$ . Table 4.1 contains the parameters which result from fitting the data from these previous experiments. Before doing this fit, the existing electron scattering data were renormalized. All the previous experiments involved relative measurements on  $^{90}Zr$  and  $^{92}Mo$ . Using our best-fit coefficients for  $^{90}Zr$ , normalizations for the  $^{90}Zr$  data were calculated. The same normalizations were then applied to the  $^{92}Mo$  data.

The cutoff radius,  $R_0$ , used in the expansion is 10  $fm$  and the form of the expansion is

$$\rho(r) = \sum_{n=1}^{10} A_n q_0^n j_0(q_0^n r)$$

where  $q_0^n R_0$  is the  $n^{th}$  zero of  $j_0$ . The rms radius of the charge density is 4.315

$\pm 0.002 \text{ fm}$ . The density has been normalized so that

$$\int_0^{R_0} \rho(r)r^2 dr = \frac{Z}{4\pi}.$$

Beyond  $q = 2.1 \text{ fm}^{-1}$  pseudodata were used to determine the coefficients.

The density obtained from this fit was used to calculate normalizations for our forward scattering data. Each angle sweep of our data set has at least one and usually more points which overlap with the momentum-transfer range of the existing data. A single normalization factor is fit for each angle sweep using in the fit only the overlapping points of that sweep. A systematic error is added in quadrature to reduce the  $\chi^2/\text{point}$  for the overlapping points of a sweep to the same value obtained in the fit for the existing data alone. Normalization factors for the forward scattering data points are summarized in *table 4.2*.

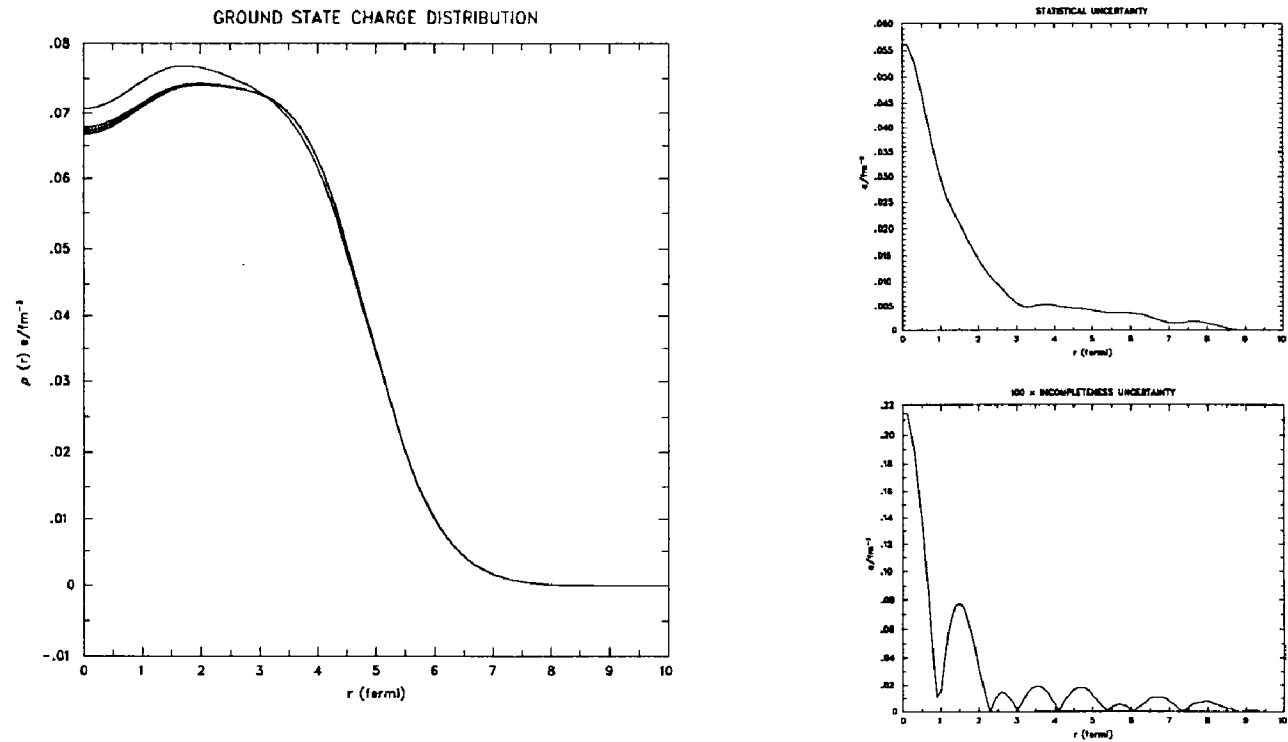


Figure 4.2 Fitted ground state density and associated uncertainties. The uncertainties are broken down into two components: statistical and incompleteness (or model dependent). The solid curve shown with the density is a Hartree-Fock Density Matrix Expansion (HFDME) calculation.

Forward Scattering Normalisations		
$\theta$ (degrees)	$E$ (MeV)	Normalisation Factor
40.0	104.5	0.914
60.0	104.5	0.914
75.0	104.5	0.914
90.0	104.5	0.914
75.0	130.4	0.914
45.0	189.6	0.957
54.8	189.6	0.957
65.0	189.6	0.957
76.0	189.6	0.957
88.0	189.6	0.957
101.0	189.6	0.957
40.0	279.1	0.871
75.3	279.1	0.871
88.4	279.1	0.871
97.1	279.1	0.871
40.0	365.1	1.034
74.7	365.1	1.034
80.5	365.1	1.034
40.0	366.7	0.957
50.0	366.7	0.957
79.5	366.7	0.957
87.0	366.7	0.957
95.5	366.7	0.957
105.0	366.7	0.957

**Table 4.2** Normalisation factors for forward scattering data.

Our normalized high- $q$  data were then used as input for a final fit to the combined data sets. This fit extends the effective momentum-transfer range to  $3.1 \text{ fm}^{-1}$ . The density obtained in this fit is shown in *fig. 4.2* along with the associated errors. The Fourier-Bessel parameters for this fit are given in *table 4.3*.

#### Backward Scattering Data

The fit to the combined data sets described above was used to normalize

Ground State Charge Density Parameterisation		
$n$	$A_n$	$\delta A_n$
1	0.153039157	0.000019740
2	0.098374069	0.000091770
3	-0.017078359	0.000160335
4	-0.029888041	0.000098280
5	0.002914800	0.000057225
6	0.008283870	0.000075600
7	-0.000722505	0.000075705
8	-0.002737560	0.000050400
9	-0.000445095	0.000063315
10	0.000231000	0.000044100

**Table 4.3** Fourier-Bessel Coefficients for the the ground state charge distribution of  $^{92}\text{Mo}$ . The fit included the normalised high- $q$  data from this experiment.

the backward scattering data. In the cases where statistics for the elastic cross section were adequate (better than 5%) we simply calculated the cross section from the parameters in *table 4.3* and scaled the data. If the statistics on the elastic were poor we used normalizations from separate runs taken specifically for normalization. These runs were forward scattering runs taken during beam tune-up just prior to the change to the backward angle. Normalization factors obtained in this way do not account for small errors in the target angle. At backward angles and in transmission mode these errors can result in large errors in target thickness which do not show up in the forward scattering point. *Table 4.4* summarizes the normalizations obtained in this way.

Backward Scattering Normalisations		
$\theta$ (degrees)	$E$ (MeV)	Normalisation Factor
160.0	80.4	1.911
155.0	100.3	0.688
155.0	125.7	1.138
155.0	139.4	0.926
155.0	159.5	0.926
155.0	175.1	0.817
155.0	189.6	0.957
155.0	204.8	0.926
155.0	219.2	0.926
155.0	239.7	0.926
155.0	259.0	0.926
155.0	289.8	0.918

**Table 4.4** Normalisations for backward scattering data.

## 5. Data Reduction – Densities

The basic procedures used to extract transition densities are those used by Heisenberg<sup>(16)</sup>. Three computer programs were used in extracting the densities, each corresponding to different assumptions about the transition density. The quality of the data and the nature of the transition determined which code was actually used. All three programs do full DWBA calculations of the cross sections. The relevant densities are parameterized in some way and these parameters are fit using a least-square procedure.

### 5.1 DENSITY FITTING PROGRAMS

The three computer programs, FOUBES1, FOUBES2 and FOUBES2A, were written by J. Heisenberg. The program FOUBES1 is used for cases where only a single density contributes to the form factor *i.e.* for natural parity transitions where the transverse contribution is negligible or for magnetic transitions. In this program the model for the transition density is an option. Three models were used here: the Fourier-Bessel Expansion (FBE), the single-particle model (SPM) using Woods-Saxon wavefunctions, and a polynomial times Gaussian (PG) model. The program FOUBES2 is used for electric transitions with a non-negligible transverse contribution to the cross section. In this case the scattering can be expressed in terms of the two densities,  $\rho_L(r)$  and  $J_{L,L+1}(r)$ . A simultaneous fit is made to the charge and current densities. These fits are done in the FBE but with starting values that can be input in a model-dependent way (*e.g.* using a SPM parameterization to obtain a starting value for the fit.) FOUBES2A is also used for simultaneous fits of the longitudinal and transverse contributions but allows the use of several models for the transition density. The model is chosen separately for the charge and current densities and for the fits presented here only the PG and SPM models were used.



## 5.2 MODELS FOR THE TRANSITION DENSITIES

Considerable effort has gone into studying “model-independent” ways of extracting nuclear densities. The FBE has emerged as a good way to parameterize the transition densities both in terms of introducing a minimal amount of restrictions to the density and in facilitating the calculations. The extra flexibility the FBE offers, however, is often a problem when the data are not of uniform quality *i.e.* when the form factor is not clearly mapped out over a large enough region of momentum transfer. In these cases by applying a more restrictive model (which decreases the number of parameters to be fit) the density can often be extracted more reliably.

The SPM constrains the densities and at the same time provides a simple interpretation in terms of individual particle orbits. When the transition is dominated by a few particle-hole components as is often the case for high spin states this model may provide a good fit with a minimum number of adjustable parameters. The PG model for the density comes somewhere between the FBE and the SPM in terms of model dependence. For transitions which have no obvious particle-hole structure a very general shape with appropriate large  $r$  behavior can be described with a few parameters.

### Fourier Bessel Expansion

The FBA expands densities as a series of spherical Bessel functions. The expansions used are for  $r \leq R_0$

$$\rho_L(r) = \sum_{\mu=1}^{15} A_{\mu} q_{\mu}^{L-1} j_L(q_{\mu}^{L-1} r) \quad (5.1)$$

$$J_{L,L+1}(r) = \frac{\hat{L}}{\sqrt{L+1}} \frac{\omega}{c} \sum_{\mu=1}^{15} B_{\mu} j_{L+1}(q_{\mu}^L r) \quad (5.2)$$

$$J_{L,L}(r) = \sum_{\mu=1}^{15} C_{\mu} j_L(q_{\mu}^L r) \quad (5.3)$$

Where  $q_\mu^L R_0$  is the  $\mu^{\text{th}}$  zero of  $j_L(x)$ . For  $r \geq R_0$  all the densities defined as zero. For the densities in  $^{92}\text{Mo}$  we have used  $R_0 = 11.00 fm$ . The expansion for an infinite number of coefficients is complete on the interval  $0 \leq r \leq R_0$ . The model dependence is a result of truncating the expansion at 15 terms. The data determine the coefficients for which  $q_\mu^L$  is closest to  $q_{max}$ , the maximum momentum transfer covered by the data. The remaining coefficients are determined by fitting additional pseudodata points in the region  $q_{max} \leq q \leq q_{15}^L$ . These points are spaced at  $0.0095 fm^{-1}$  intervals in momentum transfer space. The pseudodata are given a value of zero and an uncertainty determined by an exponential upper limit as discussed in Heisenberg<sup>[16]</sup>. Additional model dependence enters through the use of a tail bias in coordinate space. Beyond some cutoff radius an exponential tail is fit to the initial guess for the density. Differences between this exponential tail and the fitted density contribute to the  $\chi^2$  of the fit. The tail bias can be used to ensure that the shape of the density is reasonable at large radii.

### Single-Particle Model

In this model the densities are written in terms of single particle wavefunctions. The forms for the densities are given in Heisenberg and Blok<sup>[33]</sup>. The charge density in the SPM is given by,

$$\rho_L(r) = \sum_{a,b} \frac{1}{\hat{J}_f} S_{ab,L} \rho_L^{ab}(r) \quad (5.4)$$

The density is basically a sum over single-particle densities with the spectroscopic amplitudes as weighting factors. The spectroscopic amplitudes are given by,

$$S_{ab,L} = \frac{\hat{J}_f}{\hat{L}} \langle \psi_f || [a_a^\dagger \otimes \tilde{a}_b]_L || \psi_i \rangle \quad (5.5)$$

The form of the Wigner-Eckhart Theorem used is given in eq. (2.11). With this definition a pure single-particle transition has spectroscopic amplitude of 1.

The first term in the single particle density is given by

$$\rho_L^{ab}(r) = eC_{ab,L}u_a(r)u_b(r) \quad (5.6)$$

with,

$$C_{ab,L} = (-1)^{L+j_a-\frac{1}{2}} \frac{\hat{j}_a\hat{j}_b}{\sqrt{4\pi}}(j_a\frac{1}{2}j_b - \frac{1}{2}|L0) \quad (5.7)$$

The spin-orbit correction term has been included for the charge density. The current densities can similarly be expressed in terms of the single-particle wavefunctions and spectroscopic amplitudes.

The single particle wavefunctions are generated as solutions to a Woods-Saxon well with spin-orbit coupling. A separate well depth and radius parameter is used for each orbit. The well depth is adjusted for each orbit to achieve a desired separation energy. For the orbits used in the SPM fits, the separation energies which were used are shown in *table 5.1*.

Orbit	Separation Energy (MeV)
$\pi 1f_{5/2}$	8.96
$\pi 2p_{3/2}$	8.57
$\pi 2p_{1/2}$	8.37
$\pi 1g_{9/2}$	6.05
$\nu 1g_{9/2}$	11.20
$\nu 2d_{5/2}$	6.40

**Table 5.1** Separation energies used in the SPM fits for transition densities.

A spin-orbit coupling constant of 7.50 MeV, and well diffuseness parameter of 0.700 fm are taken as fixed. The parameters which are fit vary from level to level and will be discussed on an individual basis. Generally the spectroscopic amplitudes of the various single-particle components are adjusted. Occasionally the well radius and a quenching factor for the current are also fit. In addition to the single-particle components a core polarization density is added in the form

of a Fourier–Bessel expansion. The amplitude for this density is an additional parameter which can be fit. The errors for the densities extracted using the SPM do not include a component for model dependence.

The SPM densities as described above are for ‘point’ protons. The measured densities also reflect the charge distribution of the proton itself. The SPM densities are folded with the proton density before comparison with experiment. The procedure for this folding is outlined in Heisenberg, *et al.*<sup>[9]</sup>. The proton form factor is taken from Simon, *et al.*<sup>[34]</sup>.

#### Polynomial–Gaussian Model

In this model the density is expressed as,

$$\rho_L(r) = \sum_{n=1}^5 A_n (r/r_0)^{2n+L} e^{-(r/r_0)^2} \quad (5.8)$$

This expansion produces terms which fall off like  $e^{-r^2}$  at large  $r$  which is the same behavior as harmonic oscillator wavefunctions. Up to 5 terms can be used in the polynomial and the coefficients  $A_n$  and the radius parameter  $r_0$  can be fit.

A comparison of PG and FBE fits for well determined densities reveals that fitting 5 terms in the polynomial and the radius parameter is usually sufficient to provide a very good fit. For fits to the  $2_1^+$  state in  $^{92}\text{Mo}$  the  $\chi^2$  for the PG density is only 2% higher than for the FBE density using 14 coefficients. While a detailed comparison has not been made the PG expansion provides a very flexible shape and avoids the use of the high- $q$  constraint or tail bias.

## 6. Discussion of Results

This chapter contains a discussion of the transition densities which have been extracted. While a reduction of the data to transition densities is an end in itself (especially when it is done in a model independent way) one would like to make some connection with the underlying nuclear structure. Toward this goal we compare the densities obtained with predictions from model calculations. This chapter is organized in the following way. First there is a short discussion of the model calculations which are used in the discussion of the densities. This is followed by sections discussing each state or group of states for which densities have been obtained. The discussion includes details of the density fitting procedure relevant to the fit and when possible a discussion of the density in terms of nuclear physics. Appendix C contains a summary of the density parameters for the fits shown in this chapter.

### 6.1 MODEL CALCULATIONS

For elastic scattering we compare the results with a Hartree-Fock calculation using a Density Matrix Expansion for the interaction. This calculation was performed at UNH using the computer program of Negele<sup>[36]</sup>. Two other model calculations were used for comparison. These calculations provide information on excited states as well as groundstate occupations for the valence orbits.

The first calculation is a shell model calculation (SM) This calculation was done at UNH with the matrix elements and single-particle energies of Haxton and Dubach<sup>[36]</sup>. These matrix elements and energies were applied by Haxton to calculate excited state structure of <sup>90</sup>Zr and have been applied here to <sup>88</sup>Sr, <sup>89</sup>Y and <sup>92</sup>Mo without adjustment. The shell model program is a descendant of the Glasgow Code<sup>[37,38]</sup> and uses *m*-scheme coupling. The residual interaction used is a combination of a pairing force and a multipole interaction. The neutron shell is closed and proton excitations within the  $1f_{5/2}$  to  $1g_{9/2}$  orbits are allowed. The levels up to 4.0 MeV were calculated.

In  $m$ -scheme coupling the individual particle couplings are not transparent. The wavefunctions are given in terms of the occupation numbers for each orbit. In some cases however an educated guess of the couplings can be made. For example, suppose a  $2^+$  state has a dominant component with occupations of 5, 4, 1 and 4 for the  $1f_{5/2}$ ,  $2p_{3/2}$ ,  $2p_{1/2}$  and  $1g_{9/2}$  orbits respectively. An obvious coupling is  $(1f_{5/2}^{-1}, 2p_{1/2})_{2^+}$  with the remaining particles coupled in pairs to spin zero. In the discussion of the densities the SM wavefunctions will be discussed in this manner.

The second calculation is a one-broken pair calculation<sup>[39]</sup> (BP). The BP calculation was performed by Dr. K. Allaart at Vrije Universiteit, Amsterdam. This calculation uses a number-projected BCS groundstate. From that groundstate neutron  $1p1h$  excitations and proton two-quasi-particle excitations are allowed. For both neutrons and protons the  $1f_{7/2}$  through  $1h_{11/2}$  orbits are taken into account. The states below 5.2 MeV were calculated. For the calculation of  $^{88}\text{Sr}$  and  $^{90}\text{Zr}$  some adjustments were made to the single particle energies to match the energies of some particularly pure  $1p1h$  high spin states.

For both of these calculations the densities are given in terms of the one-body spectroscopic amplitudes. To construct the radial shapes of the densities we use wavefunctions generated with the HFDME calculation. A SPM model expansion for the density then allows a reconstruction of the radial shape. When using the Hartree-Fock (HF) wavefunctions a correction must be applied for the residual center-of-mass motion of the HF nucleus. This correction is applied using the procedure of Uberall<sup>[13]</sup> for harmonic oscillator wavefunctions. When using the SPM expansion for the density the result must be folded with the nucleon density before comparison with experiment as explained in Chapter 5. Both calculations give reasonable agreement for the energies of the excited states as can be seen in *fig. 6.1*.

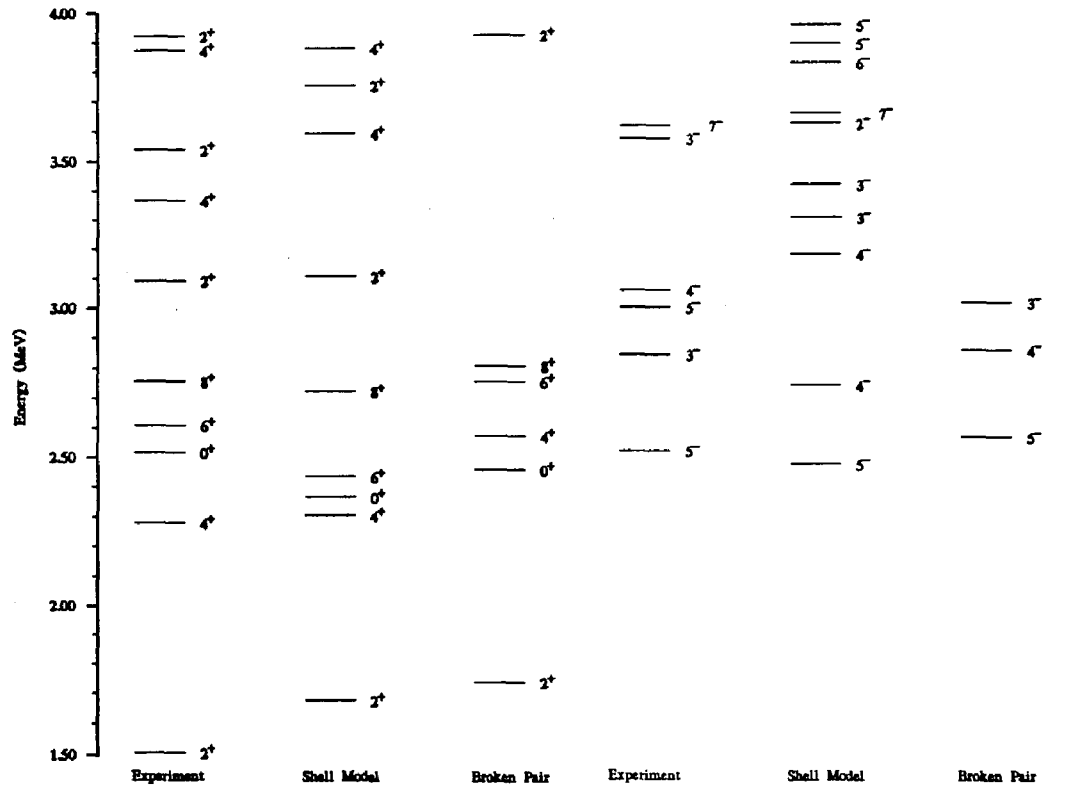


Figure 6.1 Excited states in  $^{92}\text{Mo}$  below 4.0 MeV and the predictions of two calculations.

The BP and SM calculations compliment each other when making comparisons with the extracted densities. The BP calculations when properly adjusted are very good at predicting states which are predominantly  $1p1h$  in nature. Since the BP calculation includes a large model space it includes more collectivity (*i.e.* core polarization) which can significantly increase the strength of the low lying levels. This is ideal for electron scattering which is only sensitive to the one-body parts of the charge and current operators. The SM calculation on the other hand includes the multi-particle multi-hole aspects of the structure. As will be seen in the discussion, these components appear to be important in  $^{92}\text{Mo}$ .

## 6.2 ELASTIC SCATTERING

*Figure 4.2* shows the ground state density obtained by fitting data from this experiment as well as data from previous experiments. *Figure 6.2* shows the elastic form factor with the elastic scattering data included in the fit. The high- $q$  data (above  $2.1 \text{ fm}^{-1}$ ) collected in this experiment mainly affect the density in the nuclear interior. The error bars are significantly reduced in the nuclear interior and the density itself is roughly 10% lower when these high- $q$  data are included. This is outside the one-sigma error bars of the fit done excluding these data and indicates that the incompleteness error is underestimated by the fitting program. This is in agreement with the conclusions of Dreher, *et al.*<sup>[32]</sup>. When the high- $q$  data are included in the fit, the shape of the density more closely resembles the HFDME prediction also shown in *fig. 4.2*.

Several elastic scattering studies have examined the difference in groundstate densities between  $^{92}\text{Mo}$  and  $^{90}\text{Zr}$ <sup>[28-30]</sup>. Naively, the difference should correspond to the density of the additional protons in the orbits to which they are added. For example the difference in density between  $^{92}\text{Mo}$  and  $^{90}\text{Zr}$  might correspond to the density of two protons coupled to spin zero in the  $1g_{9/2}$  orbit.



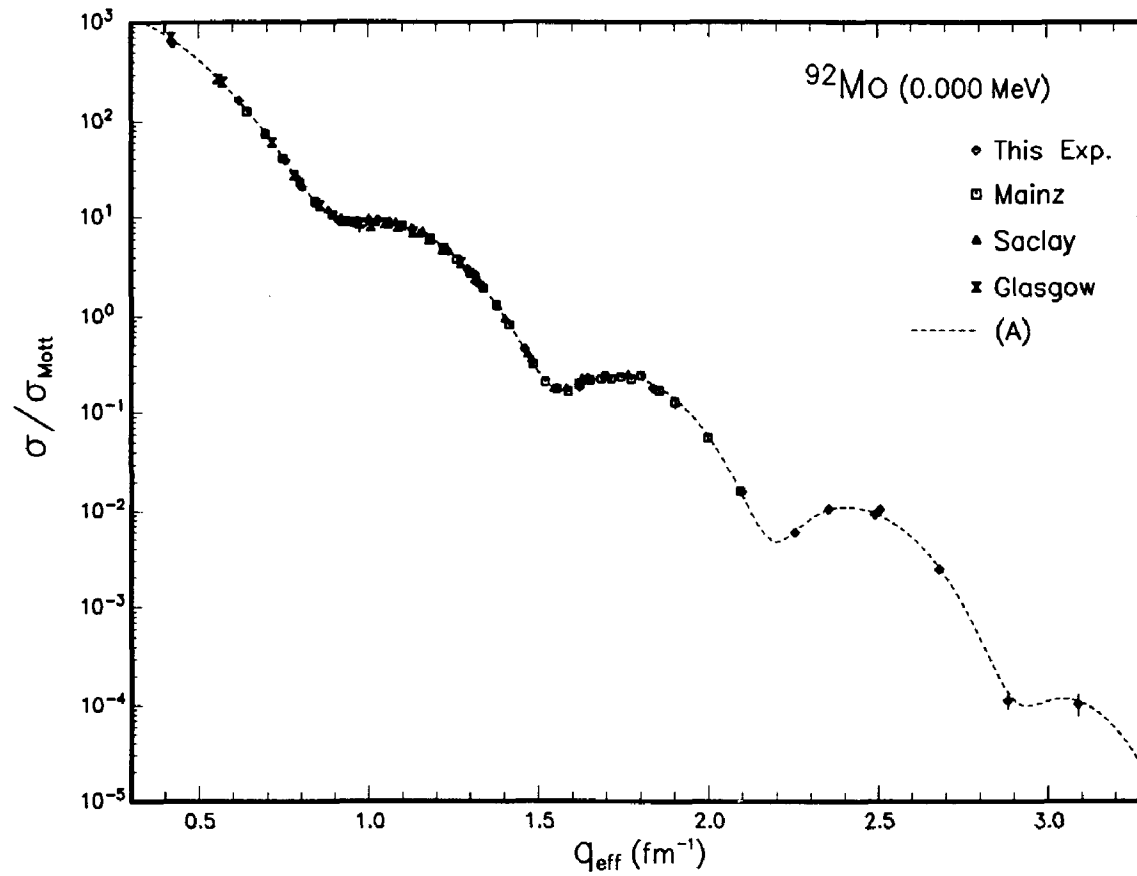
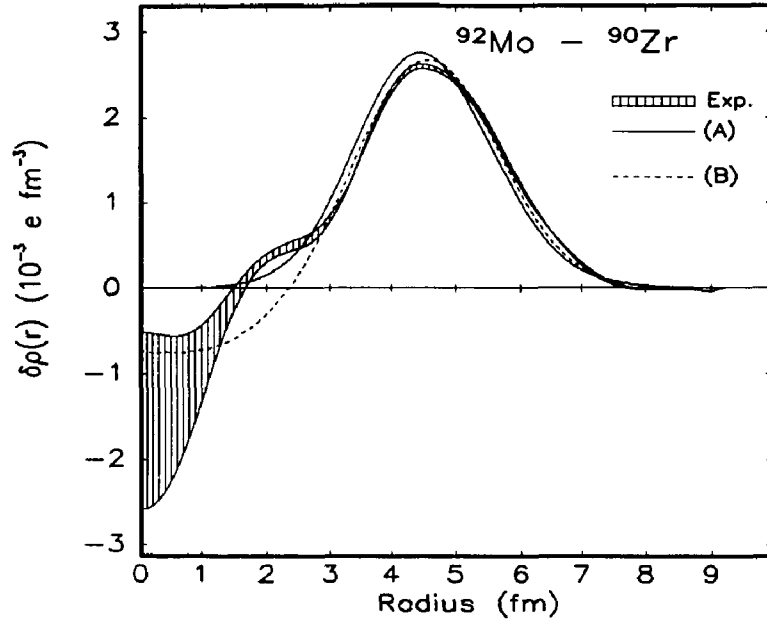


Figure 6.2 Elastic scattering form factor showing the  $(e, e')$  data included in the fit. The data have all been recalculated to 370.0 MeV. The Mainz data are taken from the thesis of B. Dreher (*ref. 19*), the Saclay data are from Ho, *et al.* (*ref. 20*) and the Glasgow data are from Singhal, *et al.* (*ref. 21*). The curve (A) is a distorted wave fit described in Chapter 4.



**Figure 6.3** The difference in the ground state charge densities between  $^{92}\text{Mo}$  and  $^{90}\text{Zr}$ . The curve is the density corresponding to a  $(\pi 1g_{9/2})_{0+}^2$  configuration which has been normalized so that  $4\pi \int_0^{10} \rho(r)r^2 dr = 2e$ . The error in the difference is taken to be the sum of the errors for the two densities.

*Figure 6.3* shows the difference in the experimental densities between  $^{92}\text{Mo}$  and  $^{90}\text{Zr}$ . The solid curve shows the  $(\pi 1g_{9/2})_{0+}^2$  density which has been normalized to have a charge of  $2e$ . While the general shape is correct, the experimental difference shows structure in the nuclear interior which cannot be reproduced by this simple picture.

The dashed curve in *fig. 6.3* is the HFDME prediction for the density difference. The HFDME prediction gives very good agreement in the general shape of the difference and clearly predicts the observed redistribution of the charge out from the nuclear interior as well as the additional charge on the surface.

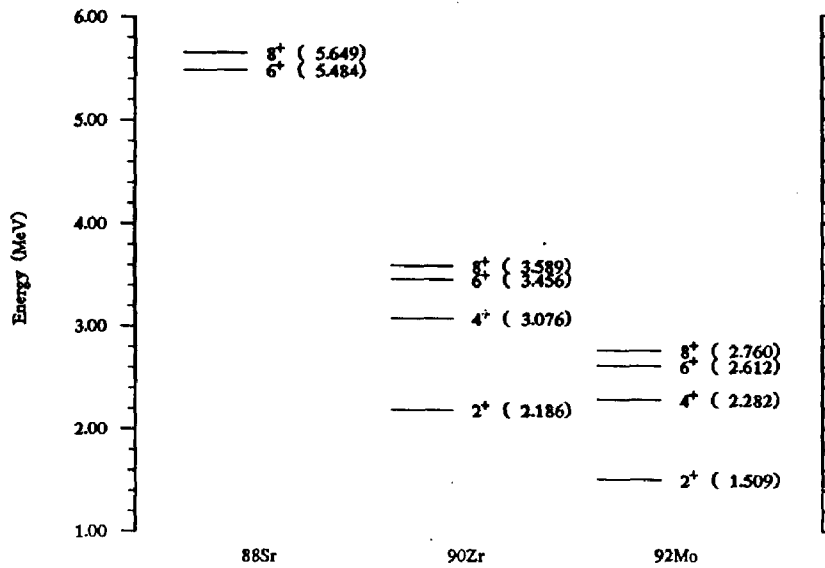


**Figure 6.4** Excitation energies of states attributed to the  $\pi(1g_{9/2})^2$  configuration.

The relatively good agreement of the HFDME difference with the experimental one is interesting especially in the nuclear interior. The HFDME prediction for the density itself is high by a significant amount at small radii. The same overprediction occurs in  $^{90}\text{Zr}$  but in the difference there is a cancellation of this effect. In a recent study of the density differences between the lead isotopes<sup>[40]</sup> a similar observation was made. While the redistribution of charge is well predicted by the HFDME calculation the value at which the density saturates is not.

### 6.3 THE $\pi(1g_{9/2})^2$ MULTIPLET

The low lying positive parity states form a  $2^+, 4^+, 6^+, 8^+$  multiplet based on the  $\pi(1g_{9/2})^2$  configuration. The same multiplet has been observed in  $^{90}\text{Zr}$  as have the  $6^+$  and  $8^+$  states in  $^{88}\text{Sr}$ . Figure 6.4 shows the excitation energies of the states attributed to this configuration in  $^{88}\text{Sr}$ ,  $^{90}\text{Zr}$  and  $^{92}\text{Mo}$ . As mentioned

in Chapter 1 the excitation of these states by electron scattering indicates the presence of  $\pi(1g_{9/2})_0^2$  components in the groundstates of these nuclei. The data for  $^{90}\text{Zr}$  and  $^{88}\text{Sr}$  have been previously reported in Heisenberg, *et al.*<sup>[3]</sup> and in the thesis of L. T. Van derBijl<sup>[41]</sup>.

The form factors for the states in  $^{92}\text{Mo}$  are shown in *fig.* 6.5. For the  $2^+$  the  $B(E2)$  value of  $1.13 \pm 0.6 \times 10^3 e^2 fm^4$  as determined in Coulomb excitation measurements<sup>[42]</sup> was included in the fit as an extra data point. The fits were done using the program FOUBES1 which uses a single density. The backward scattering data for these levels are well fit using the density obtained by fitting the forward scattering data alone. This indicates only a negligible contribution from the transition current density as is expected for recoupling of a proton pair. For the  $2^+$  and  $4^+$  states the fit was done using the FBE for the density. For the  $6^+$  the fit was done using the SPM with a density of the form  $\alpha\pi(1g_{9/2}^{-1}, 1g_{9/2}) + \beta\pi(1g_{9/2}^{-1}, 2d_{5/2})$ . The two amplitudes  $\alpha$  and  $\beta$  were fit while the radius parameter was kept fixed at a value determined in the  $8^+$  fit (1.332 *fm*). The fit gave values of  $\alpha = 0.685$  and  $\beta = 0.113$ . For the  $8^+$  state the SPM was used with a single component,  $\pi(1g_{9/2}^{-1}, 1g_{9/2})$  in the density. For the  $8^+$  both the  $1g_{9/2}$  radius and the amplitude were fit. The results of this fit are shown in *table* 6.1.

If these states were pure  $(1g_{9/2})^2$  configurations the strength of the transitions would be correlated to the  $1g_{9/2}$  occupation in the ground state. The shape of the density would likewise be determined by the shape of the  $1g_{9/2}$  radial wavefunction. Usually, however, the lowest excited states of a given multipolarity are highly collective. To use these states to obtain spectroscopic information one must first understand the collective aspects of their structure.

In a paper describing the positive parity states in  $^{90}\text{Zr}$  by Heisenberg, *et al.*<sup>[3]</sup> a shell model plus core polarization calculation for the multiplet in  $^{90}\text{Zr}$  is shown. It indicates that the contribution from core polarization decreases as the spin increases. This is a result of two factors: fewer  $1p1h$  combinations can

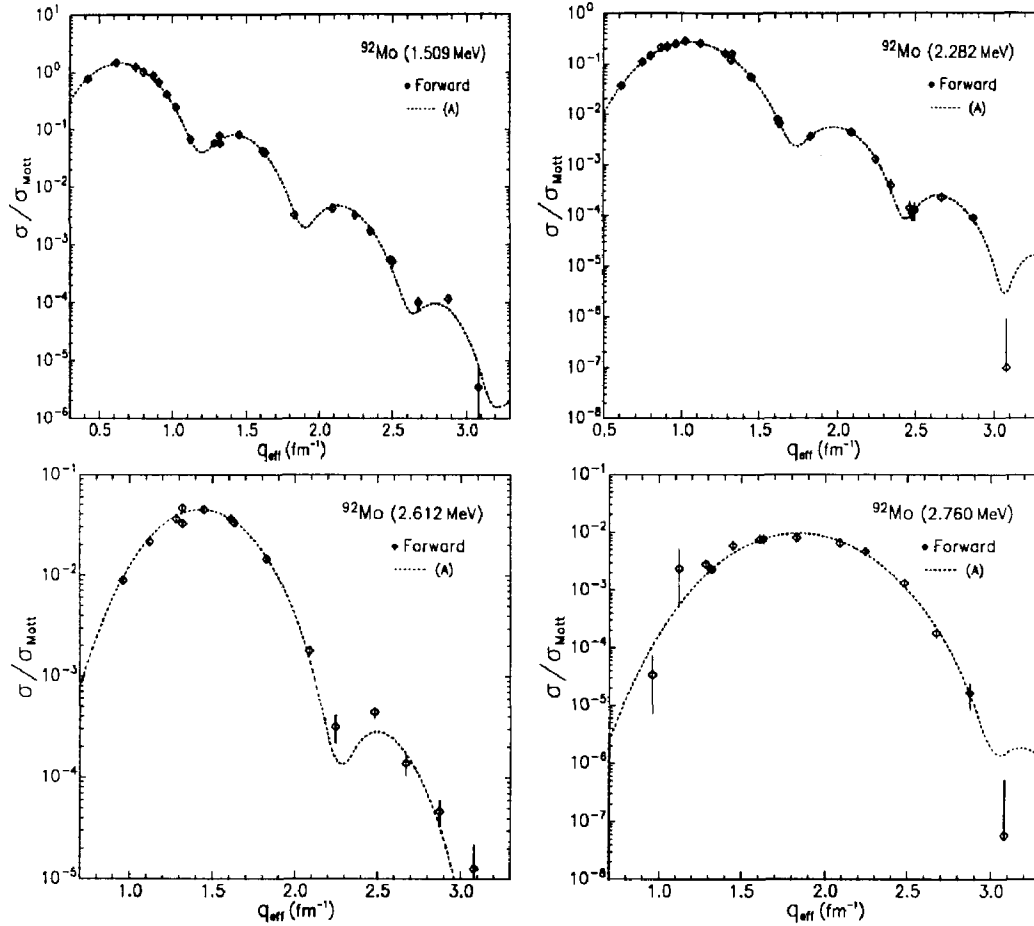


**Figure 6.5** Forward scattering form factors for the  $2^+$  through  $8^+$  states in  $^{92}\text{Mo}$ . The curves showing the DWBA fits are discussed in the text.

couple to form the higher spin states, and the residual interaction used in the calculation has a finite-range attractive component balanced by a zero-range repulsive component. In  $q$ -space the repulsive part is constant while the attractive part decreases with  $q$ . States with higher spin sample the interaction at larger values of  $q$  and therefore see a much weaker residual interaction. This effect also contributes to the energy splitting of the multiplet.

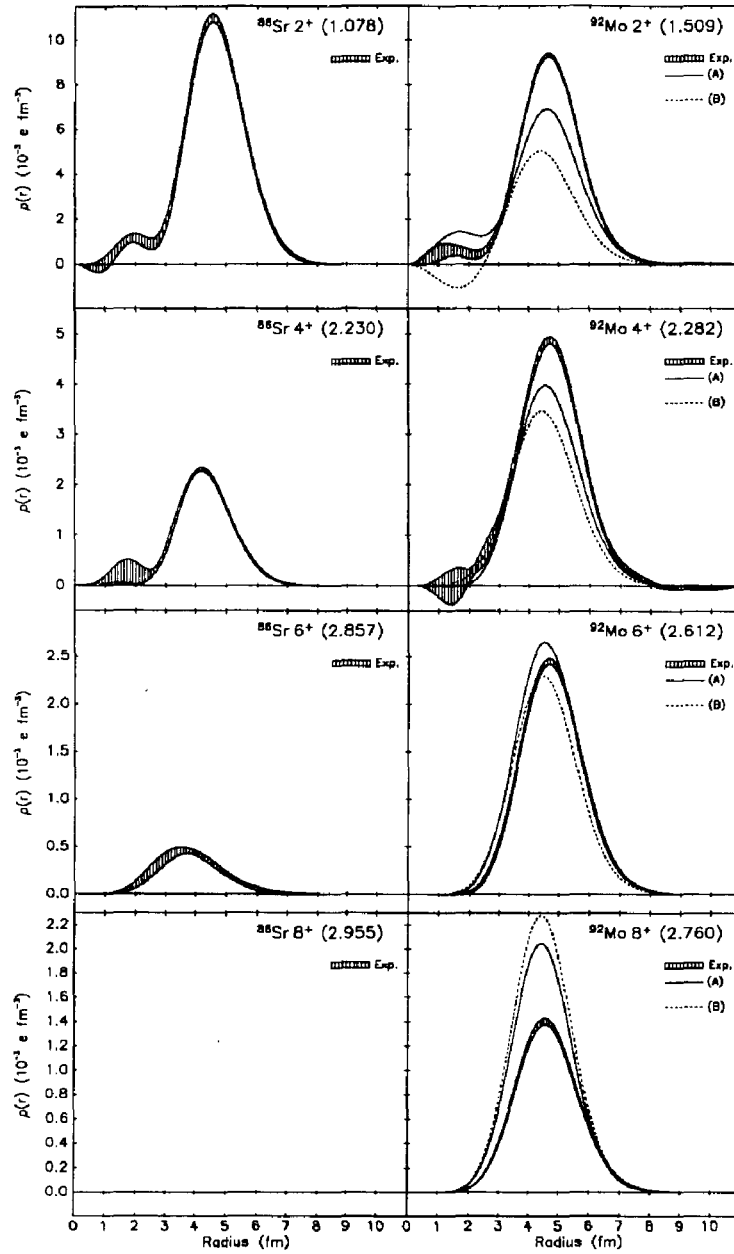


**Figure 6.6** Transition charge densities for the  $2^+$ ,  $4^+$ ,  $6^+$ ,  $8^+$  multiplets observed in  $^{86}\text{Sr}$  and  $^{92}\text{Mo}$ . In  $^{86}\text{Sr}$  the multiplet is due to  $\nu(1g_{9/2})^2$  configuration while in  $^{92}\text{Mo}$  it is due to a  $\pi(1g_{9/2})^2$  configuration.

Comparative Study of $8^+$ States				
Nucleus	$r_{rms}(fm)$	$S_8^{g^g}$	$S_8^{g^g}(BP)$	$S_8^{g^g}(SM)$
$^{88}Sr$	$4.949 \pm 0.070$	$0.360 \pm 0.015$	0.339	0.198
$^{90}Zr$	$5.035 \pm 0.040$	$0.410 \pm 0.004$	0.442	0.431
$^{92}Mo$	$5.059 \pm 0.035$	$0.582 \pm 0.010$	0.678	0.667

**Table 6.1** Summary of data on  $8^+$  states in  $^{88}Sr$ ,  $^{90}Zr$  and  $^{92}Mo$ .

This qualitative behavior of a decreasing polarization with multipolarity has been substantiated in an experiment on  $^{86}Sr$ . In  $^{86}Sr$  there are two neutron holes in the  $\nu 1g_{9/2}$  orbit which can couple to form a multiplet of states similar to the proton states found in  $^{88}Sr$ ,  $^{90}Zr$  and  $^{92}Mo$ . In electron scattering the dominant neutron component  $\nu(1g_{9/2}, 1g_{9/2}^{-1})$  will give a vanishingly small contribution to the cross section. The scattering will be sensitive mainly to the polarization density. *Figure 6.6* shows the densities for  $^{92}Mo$  and  $^{86}Sr$ . The  $2^+$  density in  $^{86}Sr$  is even larger than in  $^{92}Mo$  and also occurs at a lower energy. This indicates large collectivity for both states with additional neutron degrees of freedom for the  $^{86}Sr$  state. The densities for  $^{86}Sr$  decrease rapidly with increasing spin especially in contrast to the  $^{92}Mo$  densities. For the  $8^+$  state no peak was observed in the  $^{86}Sr$  spectrum. An upper limit on the  $8^+$  cross section can be set at roughly 1% of the  $^{92}Mo$   $8^+$  cross section. From the results of this experiment one can infer that the polarization charge for the proton  $8^+$  states is also on the order of 5% or less.

The transition densities for this multiplet provide a good observable to test models which include both the individual particle and collective aspects of the nuclear structure in this region. Also shown in *fig. 6.6* are the prediction of the two calculations, SM and BP. The solid curve labeled (A) is the BP calculation and the dotted curve labeled (B) is the SM calculation. While both calculations do a reasonable job of predicting the excitation energies of these states and predict the shapes of the densities well, quantitative agreement with the experimental densities is lacking. It is interesting to note that the largest

disagreements between theory and measurement occur for the  $2^+$  and for the  $8^+$  states. For the  $2^+$  state both calculations lack enough collectivity to account for the large strength. As would be expected the BP calculation with the much larger model space does a better job. For the  $8^+$  state however, there should be very little collectivity. Here the two calculations are in fairly close agreement but both predict too much strength.

The assumed absence of core polarization for the  $8^+$  state was the basis for a paper describing the  $\pi 1g_{9/2}$  orbit shapes in  $^{88}\text{Sr}$ ,  $^{90}\text{Zr}$  and  $^{92}\text{Mo}^{(4)}$ . Table 6.1 summarizes the results presented in that paper. The results on spectroscopic amplitudes and their relation to the ground state occupations of  $\pi 1g_{9/2}$  orbit will be discussed in more detail in the next section.

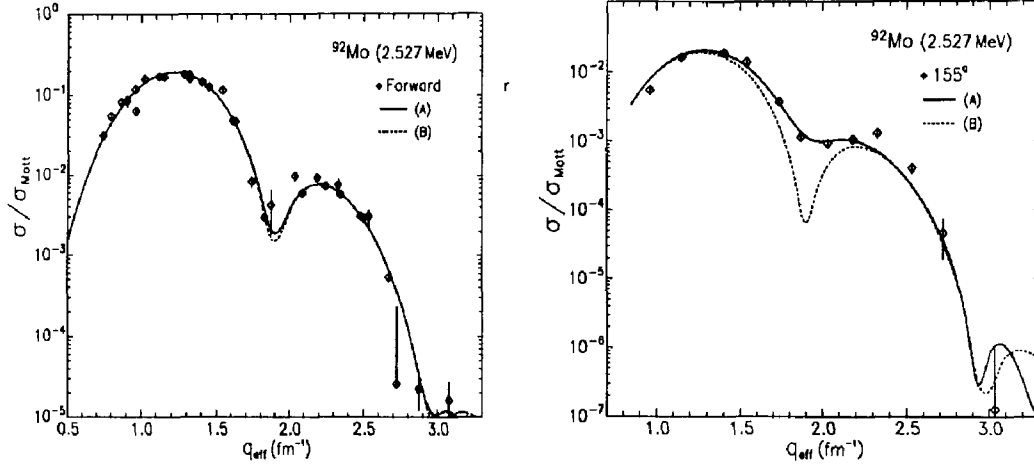
#### 6.4 THE $5^-$ STATE AT 2.527 MEV

Figure 6.7 shows the E5 form factor for the state at 2.527 MeV. The fit shown in this figure was done using the program FOUBES2 which uses the FBE for the densities. The densities obtained from these fits are shown in fig. 6.8.

Similar E5 transitions in  $^{89}\text{Y}$  (0.909 MeV) and  $^{90}\text{Zr}$  (2.319 MeV) have previously been studied. These transitions are all dominated by  $\pi(2p_{1/2}^{-1}, 1g_{9/2})$   $1p1h$  components. In the previous analysis we took the charge and current densities measured in  $^{89}\text{Y}$  to be the "effective" single-particle densities for the  $\pi(2p_{1/2}^{-1}, 1g_{9/2})$  transition. They are "effective" densities in the sense that any core polarization is included. The contribution from core polarization should vary only slowly with particle number and therefore be roughly the same in  $^{90}\text{Zr}$  and  $^{92}\text{Mo}$  as in  $^{89}\text{Y}$ .

Figure 6.8, which shows the densities for all three nuclei, illustrates dramatically the previously reported quenching of the transition current with respect to the transition charge. While the transition charge increases with  $Z$  the transition current decreases. Scaling the effective charge density from  $^{89}\text{Y}$  to fit the density in  $^{90}\text{Zr}$  or  $^{92}\text{Mo}$  would lead to an over prediction in the current density.





**Figure 6.7** Form factors for forward and backward scattering from the state at 2.527 MeV. The curves are the result of simultaneously fitting the charge and current densities in the FBA. The solid curve is the full fit and the dotted curve is the longitudinal contribution only.

This quenching has been interpreted as being due to the presence of backward going components  $\pi(1g_{9/2}^{-1}, 2p_{1/2})$ . Using the same notation as in Schwentker, *et al.*<sup>[2]</sup> we have,

$$\tilde{\rho}_{\lambda}^{ph}(r) = (u_p v_h + v_p u_h) \rho_{\lambda}^{ph}(r)$$

$$\tilde{J}_{\lambda}^{ph}(r) = (u_p v_h - v_p u_h) J_{\lambda}^{ph}(r)$$

where  $\tilde{\rho}_{\lambda}^{ph}$  and  $\tilde{J}_{\lambda}^{ph}$  are the BCS model single quasi-particle densities. The forward going amplitude,  $u_p v_h$ , and backward going amplitude,  $v_p u_h$ , add in the charge density and subtract in the current density. An increase in the backward going amplitudes as the occupation of the  $\pi 1g_{9/2}$  orbit increases from  $^{89}\text{Y}$  to  $^{92}\text{Mo}$  might explain the behavior seen in *fig.* 6.8. (The situation as described applies to even-even nuclei only. For odd-even nuclei the backward going, *i.e.* time-reversed, component has the opposite sign in both the the charge and current. We apply the same equations to  $^{89}\text{Y}$  and reverse the sign of the amplitude which is equivalent though cause for some confusion.)

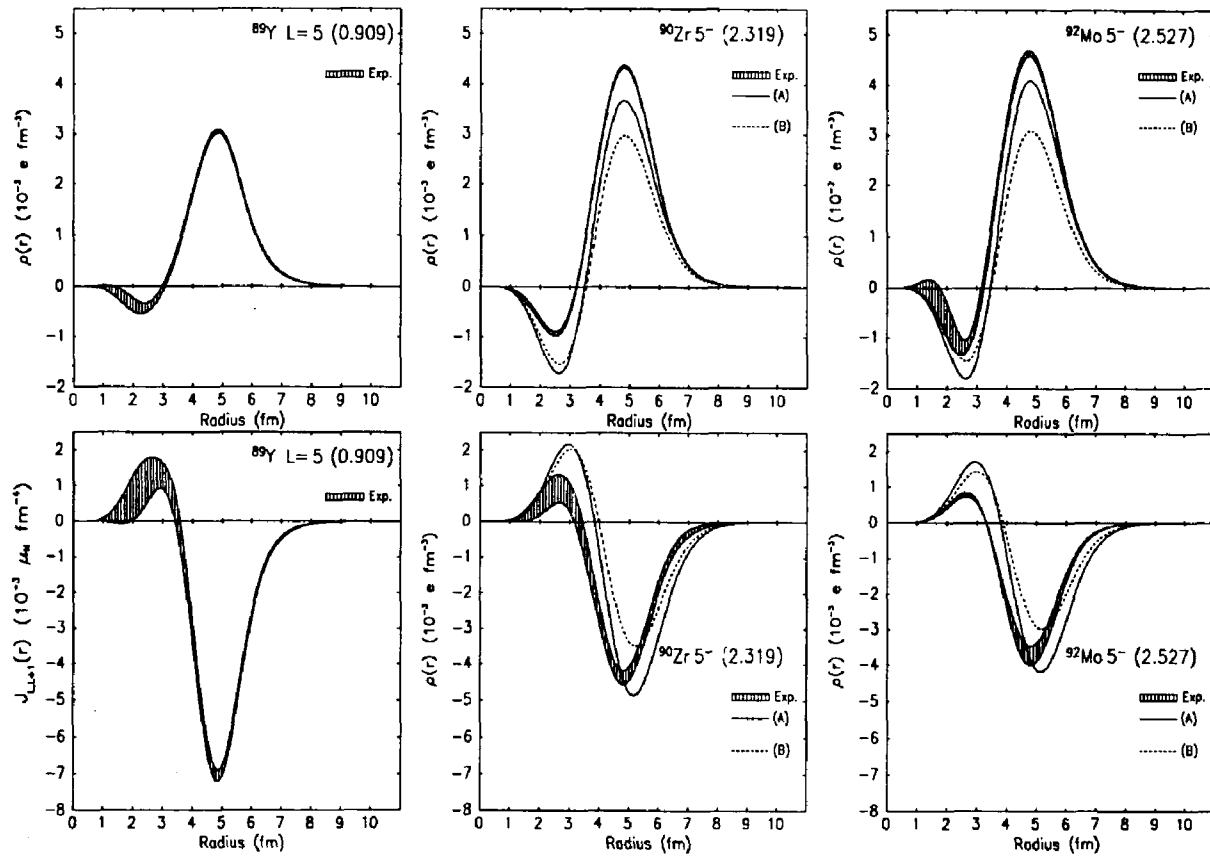


Figure 6.8 Transition densities for the E5 transitions in  $^{89}\text{Y}$ ,  $^{90}\text{Zr}$  and  $^{92}\text{Mo}$ . The strength of the transition charge increases with  $Z$  while the strength of the transition current decreases. The solid curves are the BP predictions and the dashed curves are the predictions of the SM calculation.

If we assume this mechanism for the quenching we can calculate the ratios of the backward to forward going amplitudes. The occupations can also be estimated since  $v^2 = 1 - u^2$  is the occupation probability of an orbit. We can write,

$$\rho_Y(r) = (A + \bar{A})\rho_{p \rightarrow g}(r) \quad J_Y(r) = (A - \bar{A})J_{p \rightarrow g}(r)$$

$$\rho_{Zr}(r) = (B + \bar{B})\rho_{p \rightarrow g}(r) \quad J_{Zr}(r) = (B - \bar{B})J_{p \rightarrow g}(r)$$

$$\rho_{Mo}(r) = (C + \bar{C})\rho_{p \rightarrow g}(r) \quad J_{Mo}(r) = (C - \bar{C})J_{p \rightarrow g}(r)$$

Then the ratios at a given radius can be written,

$$R_{Zr} = \left( \frac{\rho_{Zr}}{\rho_Y} \right) \left( \frac{J_Y}{J_{Zr}} \right) = \frac{(A - \bar{A})(B + \bar{B})}{(A + \bar{A})(B - \bar{B})}$$

Similarly we get,

$$R_{Mo} = \left( \frac{\rho_{Mo}}{\rho_Y} \right) \left( \frac{J_Y}{J_{Mo}} \right) = \frac{(A - \bar{A})(C + \bar{C})}{(A + \bar{A})(C - \bar{C})}$$

Taking the ratios from the maximum values of the measured densities gives,

$$R_{Zr} = 2.31 \quad \text{and} \quad R_{Mo} = 2.94$$

If the ratio  $\bar{A}/A = -0.069$  is taken from a shell model calculation for  $^{89}\text{Y}^{(43)}$  the ratios for  $^{90}\text{Zr}$  and  $^{92}\text{Mo}$  are found to be

$$\frac{\bar{B}}{B} = 0.338 \quad \text{and} \quad \frac{\bar{C}}{C} = 0.381$$

To find the corresponding occupations it is necessary to make additional assumptions. In  $^{89}\text{Y}$  the occupation probability of the  $\pi 2p_{1/2}$  orbit can be

assumed to be about 0.5. This gives  $v_h \simeq u_h$  and,

$$\frac{\bar{A}}{A} = \frac{v_p}{u_p}$$

Then combined with  $v^2 + u^2 = 1$  this gives

$$v_p = \sin(\tan^{-1}(\frac{\bar{A}}{A}))$$

This gives  $v_p = 0.07$  and an occupation probability of .005 for the  $1g_{9/2}$  orbit.

To estimate the occupation of the  $\pi 1g_{9/2}$  orbit in  $^{90}\text{Zr}$  we take the value of  $v_h^2 = 0.63$  as determined in transfer reactions.<sup>[6]</sup> From this and the ratio  $\bar{B}/B$  one gets,

$$v_p^2 = 0.163$$

For  $^{92}\text{Mo}$  one can assume that the total number of protons in the  $2p$  and  $1g$  orbits is two more than was found for  $^{90}\text{Zr}$ . This is equivalent to assuming that the depopulation of the  $1f_{5/2}$  and  $2p_{3/2}$  orbits is about the same in  $^{90}\text{Zr}$  as in  $^{92}\text{Mo}$ . This constraint can be written as,

$$2v_h^2 + 10v_p^2 = 4.89$$

and gives the values,

$$v_p^2 = 0.34 \text{ and } v_h^2 = 0.74$$

The occupations determined by making these assumptions are summarized in *table 6.2*.

Ground State Occupations		
Nucleus	$2p_{1/2}$	$1g_{9/2}$
$^{89}\text{Y}$	(1.00)	0.05
$^{90}\text{Zr}$	1.26	1.63
$^{92}\text{Mo}$	1.48	3.42

**Table 6.2** Occupation estimates of the  $2p$  and  $1g$  proton orbits from quenching of the E5 transitions.

Calculating these occupations from the quenching factors serves a dual purpose. It is a test of the proposed quenching mechanism (*i.e.* the backward going amplitudes) by checking its consistency with transfer reactions. The quenching data also represents an independent (although *model-dependent*) measurement of some of the occupations. We can compare the occupations obtained in this way with the results of transfer reactions and also with spectroscopic amplitudes from the previous section. *Table 6.3* contains a summary of information on the occupation of the  $\pi 1g_{9/2}$  orbit for several nuclei. The numbers for transfer reactions are averages over several measurements<sup>[5-8,44,45]</sup>. In general the estimates from the quenching factors are consistent with the transfer reactions. For  $^{90}\text{Zr}$  the occupation from quenching is higher than the average from the transfer reactions but there is considerable variation among the different measurements.

Groundstate Occupations of the $\pi 1g_{9/2}$ Orbit				
Nucleus	Transfer Reactions	E5 Quenching Analysis	Broken Pair (BP)	Shell Model (SM)
$^{88}\text{Sr}$	-	-	1.04	0.27
$^{89}\text{Y}$	-	0.05	-	0.18
$^{90}\text{Zr}$	1.1	1.63	1.64	1.13
$^{92}\text{Mo}$	3.4	3.42	3.18	2.83

**Table 6.3** Summary of information on the occupation of the  $\pi 1g_{9/2}$  orbit in N=50 nuclei.

It is also interesting to examine the measured spectroscopic amplitudes for the E8 transitions (shown in *table 6.1*) with the values predicted by the two calculations. In particular it would be interesting to relate the amplitudes to groundstate occupations. Unfortunately there is a large model dependence when connecting the amplitudes to occupations. The SM calculation has virtually the same spectroscopic amplitude as the BP calculation but an occupation of 2.83 protons in the  $\pi 1g_{9/2}$  orbit compared to 3.18 protons for the BP calculation. While the amplitudes do not serve as quantitative indicators of occupation they certainly must be consistent with the occupations observed. The good agreement between the  $^{90}\text{Zr}$  and  $^{88}\text{Sr}$  BP amplitudes with experiment indicates that this calculation is consistent with relatively large occupations in this orbit. The SM calculation has lower  $1g_{9/2}$  occupations for all these nuclei being considerably lower than indicated by the transfer reactions.

#### 6.5 THE $3^-$ STATE AT 2.850 MEV

The nuclei  $^{88}\text{Sr}$ ,  $^{90}\text{Zr}$  and  $^{92}\text{Mo}$  each have a strongly excited  $3^-$  state at low excitation energy (2.734, 2.748 and 2.850 MeV respectively.) The similarity in excitation energy and transition strength of these levels indicates that they are relatively independent of proton number and are collective in nature. The states in  $^{90}\text{Zr}$  and  $^{92}\text{Mo}$  have been previously studied in a comparison of collective levels in isotone pairs<sup>[46]</sup>. The more recent measurements have an order of magnitude better resolution and extend the data to higher momentum transfer.

*Figure 6.9* shows the form factor for the  $3^-$  level in  $^{92}\text{Mo}$ . The DWBA fit was done with the program FOUDES2 using the FBE for the density. The resulting densities are shown in *fig. 6.10*. The fit to the backward scattering data improves with the inclusion of the current density. The dashed curve in *fig. 6.9* shows the contribution from the charge scattering alone. The difference shows that the contribution of the current is especially important in fitting the backward scattering data near the minima of the charge form factor. In  $^{88}\text{Sr}$

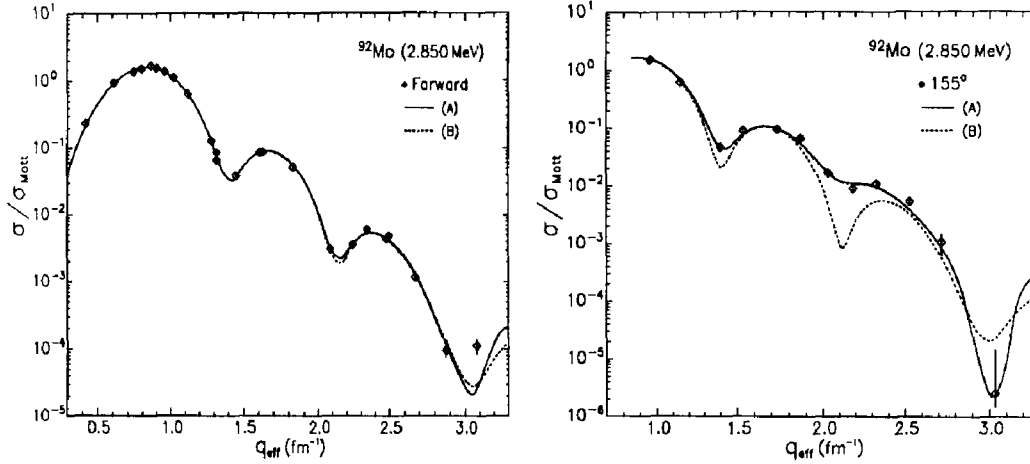


Figure 6.9 Forward and backward scattering form factors for the  $3^-$  level at 2.850 MeV. The solid curves show the full DWBA fit to the data while the dashed curves give the longitudinal contribution only.

a non-zero current density was also measured. For  $^{90}\text{Zr}$  the measurement of a current density was made impossible by the presence of an unresolved  $4^-$  state at 2.738 MeV.

Because the  $3^-$  level is thought to be highly collective the presence of any transverse strength is somewhat surprising. The collective  $3^-$  state in  $^{208}\text{Pb}$  has been shown to have very little transverse strength and the absence of the current  $J_{L,L+1}$  is generally assumed for collective states. This is equivalent to assuming that the nuclear motion can be described as the irrotational flow of an incompressible fluid. While this assumption appears to be valid for heavier nuclei, in the mass-90 region it is not.

Also shown in *fig.* 6.10 is the BP calculation of Allaart and the SM calculation. The BP transition charge density is underpredicted as is expected for a highly collective level but the qualitative agreement is good. The BP transition current density however is in remarkable agreement with the measured density. The dominant component of the calculated transition current is  $\pi(2p_{3/2}^{-1}, 1g_{9/2})$ . The SM calculation has even less collectivity and predicts neither the excitation

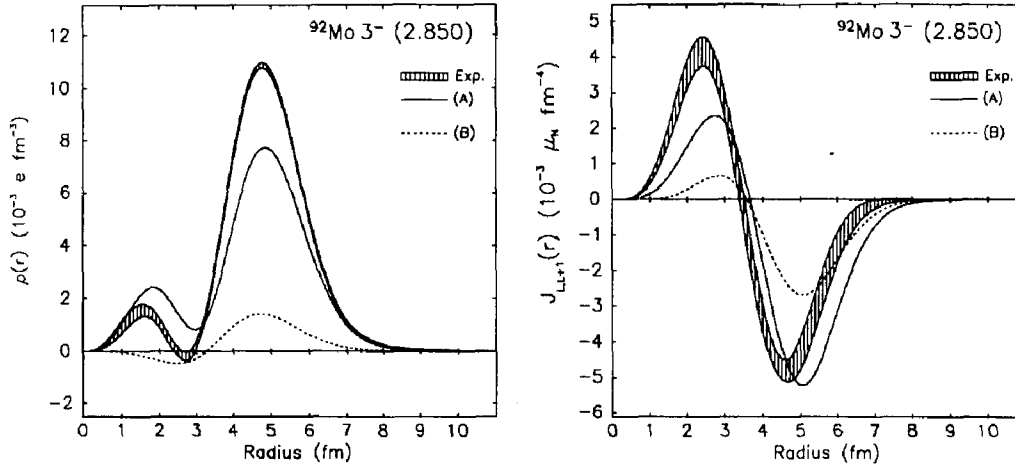


Figure 6.10 Transition charge and current densities for the  $3^-$  state at 2.850 MeV. The solid curve is the Broken-Pair prediction.

energy or transition strength with much success. The first  $3^-$  states in  $^{88}\text{Sr}$  and  $^{92}\text{Mo}$  appear to have a combination of a strong single-particle component and large polarization. While the excitation energy and transition charge density provide information on the collective aspects of the structure the shape and strength of the transition current reveals single particle aspects of the structure. This further illustrates the importance of measuring both the forward scattering and backward scattering data for understanding the nuclear structure.

#### 6.6 THE $7^-$ STATE AT 4.555 MEV

The  $5_1^-$  and  $3_1^-$  states have strong  $\pi(2p_{1/2}^{-1}, 1g_{9/2})$  and  $\pi(2p_{3/2}^{-1}, 1g_{9/2})$  components respectively. A similar state with a strong single-particle nature should exist with a  $\pi(1f_{5/2}^{-1}, 1g_{9/2})$  component. In  $^{88}\text{Sr}$  and  $^{90}\text{Zr}$   $7^-$  states corresponding to this configuration have been identified at 4.366 and 4.370 MeV respectively.

In previous reactions on  $^{92}\text{Mo}$  a state of unknown spin and parity has been observed at 4.555 MeV excitation. In the  $(e, e')$  reaction a state at this energy can be identified with the stretched  $f \rightarrow g$ ,  $7^-$  states observed in  $^{88}\text{Sr}$  and  $^{90}\text{Zr}$ .



*Figure 6.11* shows a backward scattering electron spectrum taken for  $^{90}\text{Zr}$  and  $^{92}\text{Mo}$  at roughly the same momentum transfer. The close resemblance between the two spectra made the location of the  $7^-$  state particularly easy.

*Figure 6.12* shows the form factor and fit for the 4.555 MeV state in  $^{92}\text{Mo}$ . A simultaneous fit to the forward and backward scattering data was done using the program FOUBES2. *Figure 6.13* shows the resulting transition densities. Also shown are the BP predictions (solid curve) and a pure single-particle predictions (dashed curve) using the  $\pi(1f_{5/2}^{-1}, 1g_{9/2})$  configuration.

In  $^{88}\text{Sr}$ ,  $^{90}\text{Zr}$  and  $^{92}\text{Mo}$  the E7 strength observed is considerably less than for a pure particle-hole transition. Relative to one single particle strength the transition charge densities are quenched by 0.77, 0.73 and 0.66 respectively. This situation is surprising and as yet unexplained. One possible explanation is that configuration mixing causes the strength to be spread out over several levels. This explanation seems unlikely for two reasons. First in  $^{88}\text{Sr}$  the 4.366 MeV state is the lowest known  $7^-$  state. Usually the configuration mixing tends to enhance the transition charge density for the lowest level of a given multipolarity. Instead there is a reduction of roughly 20%. Secondly in  $^{92}\text{Mo}$  where there is another known  $7^-$  state at a lower energy (3.626 MeV) it has very little single particle strength. (This state will be discussed in more detail in a later section.) The strength of the transition charge for the state at 3.626 MeV has only about 10% of one single particle strength while the particle-hole state in  $^{92}\text{Mo}$  is reduced by about 30%. If we add the single particle strengths of both of these states we again find only 80% of the pure particle-hole transition.

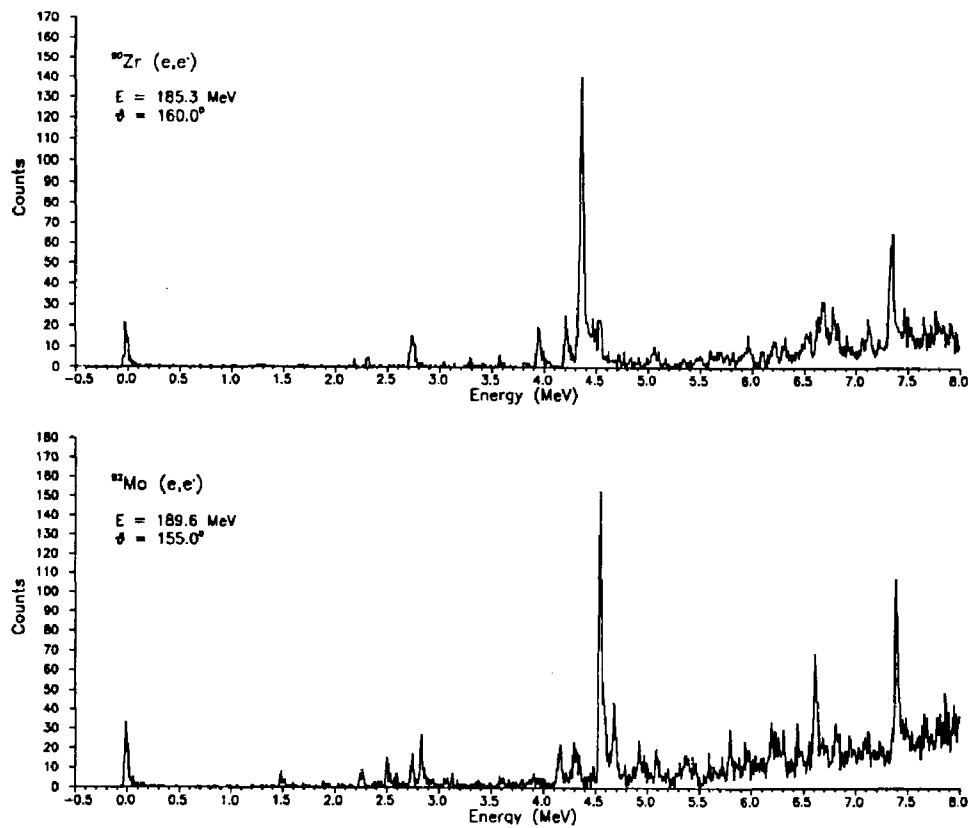
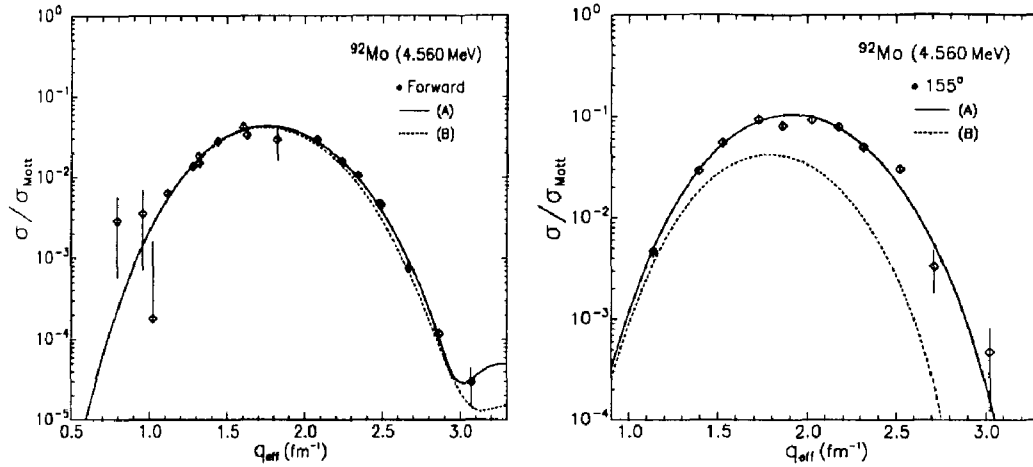


Figure 6.11 Spectra of electrons scattered from  $^{90}\text{Zr}$  (top) and  $^{92}\text{Mo}$  (bottom) at backward angles. The momentum transfer of the two spectra have roughly the same value. The strong  $7^-$  states stand out clearly at the backward angles and high momentum transfers.



**Figure 6.12** Forward and backward scattering form factors for the  $7^-$  state at 4.555 MeV. The solid curve is the full DWBA fit. The dashed curve gives the longitudinal contribution only.

In addition to the density fit described above a fit was done using the SPM with a single component,  $\pi(1f_{5/2}^{-1}, 1g_{9/2})$ , for the density. Because the transitions involve mainly two single particle orbits, the  $\pi 1f_{5/2}$  and  $\pi 1g_{9/2}$ , the results of the fits can provide detailed information on the radial shapes of the wavefunctions. Since the shapes of the  $\pi 1g_{9/2}$  orbits have already been established by studying the  $8^+$  transitions the fits to the E7 transitions depend only on the shape of the  $\pi 1f_{5/2}$  orbit.

In the SPM fit Woods-Saxon wavefunctions were used with a fixed diffuseness parameter, spin-orbit strength and separation energies for the  $\pi 1f_{5/2}$  and  $\pi 1g_{9/2}$  orbits. The  $\pi 1f_{5/2}$  radius was left as an adjustable parameter and was fit to the data along with the transition amplitude. The fit was done with the program FOUBES2A which does a simultaneous fit to forward and backward scattering data. The  $\chi^2$  for this fit was much worse than the fit using an FBE model for the density. To improve the fit the densities were constructed so that different  $\pi 1f_{5/2}$  wavefunctions were used for the charge and current densities and the two radius parameters were fit. In this manner a good fit was obtained comparable

to the FBE fit. The radii determined in these fits are shown in *table 6.4*. In addition to the statistical uncertainties the quoted uncertainties include contributions from the varying the fixed parameters. For the fixed parameters a variation of 10% in the diffuseness parameter and spin-orbit strength was included along with a 1.5 MeV variation of the separation energies.

A surprising feature of the densities is found. *Table 6.4* shows the results of fitting the full data set and fitting separately the forward and backward scattering data. The fitted radius for the forward scattering data is significantly larger than the radius fit for the backward scattering data. The sum of the  $\chi^2$ 's for the separate fits is about half of the  $\chi^2$  for the combined fit indicating a much better fit if different radii are used for the longitudinal and transverse components. While about half the uncertainty of the radius values comes from uncertainty in the fixed parameters the uncertainty in the difference of the radii is dominated by the statistical uncertainty. This indicates that it is really the data which are determining this quantity.

While still unexplained, these results appear to be consistent with other observations involving orbit radii. In the study of the  $\pi 1g_{9/2}$  radial shape it was noted that the *rms* radius obtained for  $^{93}\text{Nb}$  from a magnetic elastic scattering experiment<sup>[47]</sup> was considerably smaller than the orbit radii for either  $^{90}\text{Zr}$  or  $^{92}\text{Mo}$  obtained from fitting the  $8^+$  form factors. The magnetic scattering is sensitive mainly to the magnetization current of the unpaired nucleon while the  $8^+$  measurement involves only the transition charge density. Again the measurement involving the transition current gave a smaller radius. A similar study<sup>[48]</sup> of the  $1f_{7/2}$  orbit was made by comparing the results of scattering from  $^{50}\text{Ti}$  and  $^{51}\text{V}$  showed again that a much smaller radius was needed to explain the magnetic scattering data. The results for the E7 transitions are particularly interesting in that they involve a simultaneous measurement of the charge and current densities. As a result they are not subject to explanations involving odd-even effects or mass difference effects.

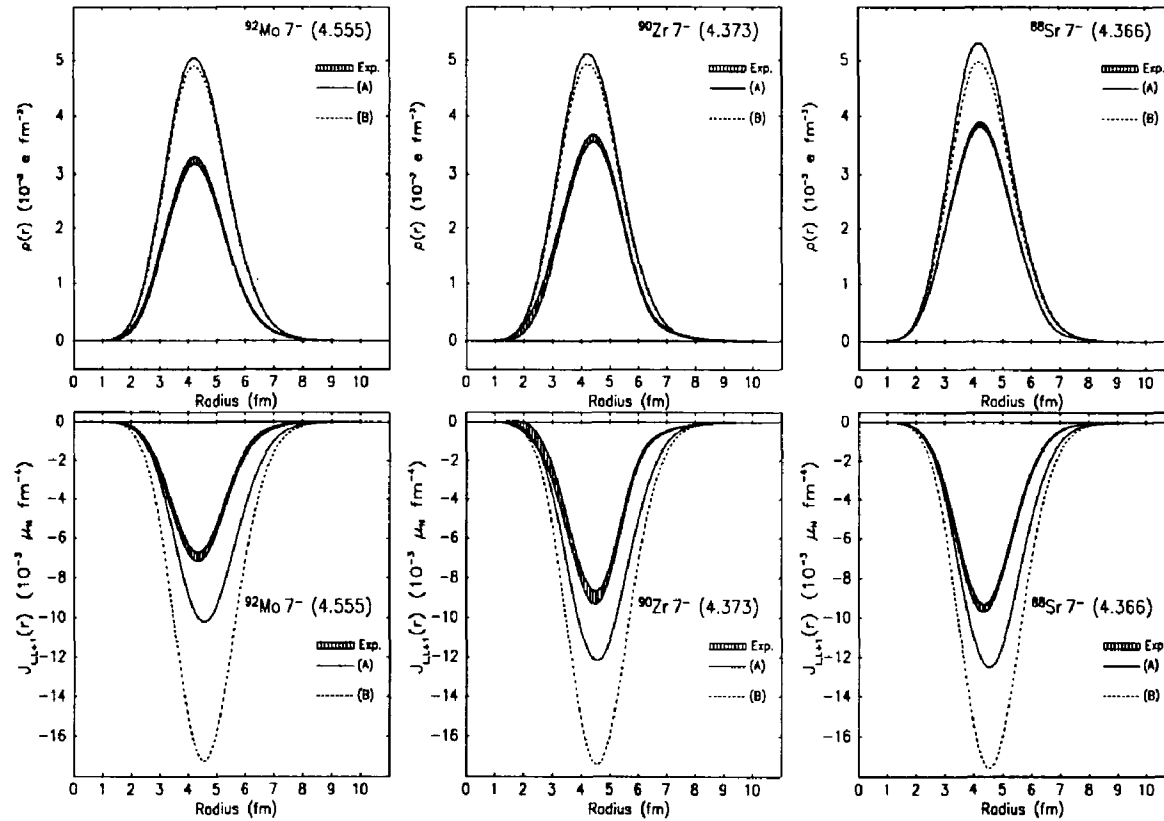


Figure 6.13 The transition charge and current densities for the  $7^-$  states in  $^{88}\text{Sr}$ ,  $^{90}\text{Zr}$  and  $^{92}\text{Mo}$ . The solid curve labeled (A) is the broken-pair prediction. The dashed curve labeled (B) is the prediction of a pure single-particle transition.

$\pi 1f_{5/2}$ Orbit Radius Determination				
Nucleus	Single Radius Fit	Separate Radii Fit		
		Charge	Current	$\Delta$
$^{92}\text{Mo}$	$4.280 \pm 0.090$ fm	$4.353 \pm 0.080$ fm	$3.953 \pm 0.100$ fm	$0.400 \pm 0.060$ fm

**Table 6.4** Radius of the  $\pi 1f_{5/2}$  orbit determined by fitting the E7 form factors in  $^{92}\text{Mo}$ .

### 6.7 STATES BETWEEN 3.0 AND 4.0 MEV

*Figure 6.1* shows excited states of  $^{92}\text{Mo}$  below 5.1 MeV where spin and parity assignments have been established. Also shown are the excitation spectra of the SM calculation and the BP calculation. Below 3 MeV the calculations both do a reasonable job of predicting the spins and parities of the observed levels. Between 3 and 4 MeV the calculations differ considerably and the BP calculation predicts only one state, a  $2^+$  state around 3.93 MeV. This indicates that the structure of the states in this region is complicated and in general dominated by  $2p2h$  components relative to the ground state. The shell model wavefunctions support this observation. Since in electron scattering we only observe the one-body densities one would expect low cross sections for these  $2p2h$  states.

In this experiment we measured cross sections for seven states between 3 and 4 MeV. In general the cross sections were all small and the backward scattering data showed little transverse strength. The  $(e, e')$  data reveal the smaller  $1p1h$  components of these states and indicate the extent of mixing between the  $1p1h$  and  $2p2h$  components. Identification of all the states discussed below relied heavily on three sources of information: Nuclear Data Sheets<sup>[42]</sup>, a thesis by E. J. Kaptein<sup>[49]</sup> describing a high-resolution  $(p, p')$  experiment, and a table of excited states observed in the  $(\alpha, \alpha'\gamma)$  reaction<sup>[60]</sup>.

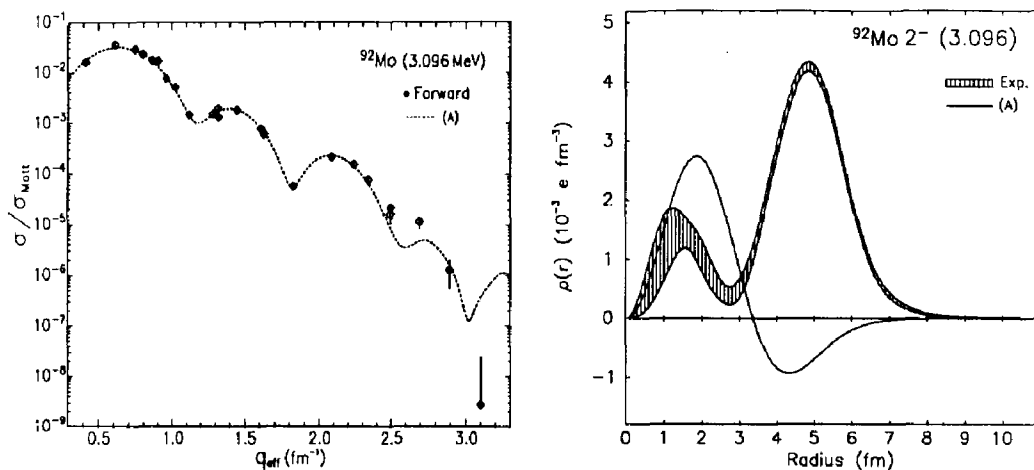


**Figure 6.14** Form factor and transition charge density for the second  $2^+$  state at 3.092 MeV.

#### The $2^+$ State at 3.092 MeV

The form factor for this state is shown in *fig. 6.14*. Also shown in *fig. 6.14* is the transition charge density extracted for this state. The fit was done using the program FOUBES1 and the FBE for the density. The data are consistent with the absence of a transition current density although a small current density does improve the fit slightly.

The SM prediction for this state is shown with the experimental density. Judging by the poor agreement with experiment the calculation provides no quantitative information on this state. The experimental density is very nearly the same shape as the density for the first  $2^+$  and therefore probably has a strong  $\pi 1g_{9/2} \rightarrow 1g_{9/2}$  component. The shell model wavefunction is suggestive of configurations in which there are two pairs each coupled to  $2^+$ . The energy of this state being very close to twice that for the first  $2^+$  suggests a  $\pi((1g_{9/2}^2)_{2+} \otimes (1g_{9/2}^2)_{2+})_{2+}$  coupling.

#### The L=4 State at 3.369

The state at 3.369 has been observed before in  $(p, p')$  and  $(\alpha, \alpha' \gamma)$  reactions. In the later reaction an L=4 assignment was made with a tentative negative parity assignment. The  $(p, p')$  reactions were consistent with the L=4 assignment.

*Figure 6.15* shows the form factor and the fitted density for this state. The fact that this state was observed in forward scattering and not at  $155^\circ$  practically rules out a  $4^-$  assignment. The fit was done assuming  $J^\pi = 4^+$ . The program FOUBES1 was used with the FBE model for the density. The good fit indicates that this assignment is correct. Also shown is a SPM fit to the data using Woods-Saxon wavefunctions. This density is a combination of two components,  $\pi(1g_{9/2}^{-1}, 1g_{9/2})_{4^+}$  and  $\pi(1g_{9/2}^{-1}, 2d_{5/2})_{4^+}$ . The amplitudes of the two components were fit and were found to be 0.08 and 0.12 respectively. The node in the density is indicative of a transition between orbitals of different oscillator shells. The  $\pi(1f_{5/2}^{-1}, 2p_{3/2})_{4^+}$  has a similar shape but peaks farther into the interior than the experimental density.

#### The $2^+$ State at 3.545 MeV

This state was only weakly excited in our experiment. *Figure 6.15* shows the forward scattering form factor for this state. The fit was done to the forward scattering data alone with the FBE model for the density. The shape of the transition charge density is very similar to the shape obtained for the state at 3.929 MeV, the fourth  $2^+$  state.



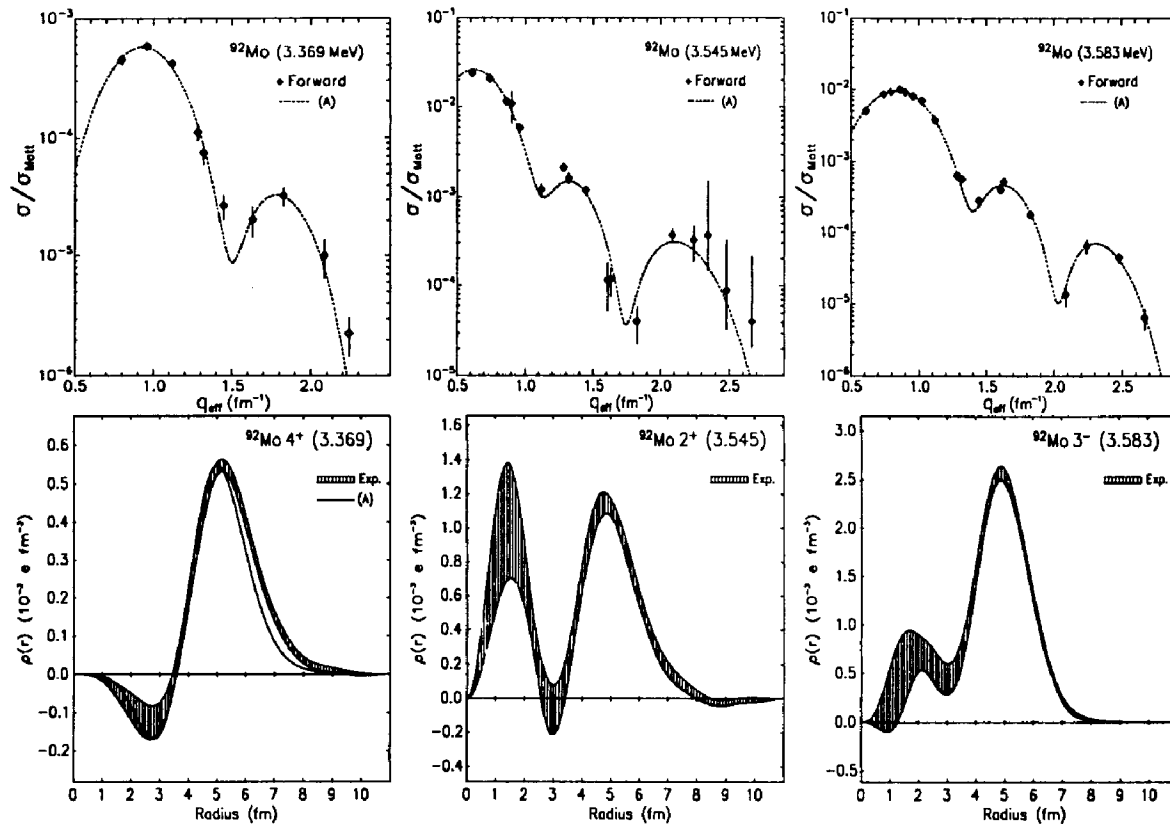


Figure 6.15 Form factors and transition charge densities for the states at 3.369, 3.545 and 3.583 MeV. The solid curves in the form factor plots are the DWBA fits as described in the text.

### The 3<sup>-</sup> State at 3.583 MeV

The positive parity states between 3 and 4 MeV are probably built from configurations like:

$$\pi((1g_{9/2}^2)_{2+} \otimes (1g_{9/2}^2)_{2+})_{J+} \text{ and } \pi((2p_{3/2}^{-1}2p_{1/2})_{2+} \otimes (1g_{9/2}^2)_{2+})_{J+}$$

In other words they involve the excitation of two quadrupole phonons. Similarly negative parity two-phonon states can arise by coupling a 3<sup>-</sup> or 5<sup>-</sup> excitation with a 2<sup>+</sup> excitation. This is probably the type of configuration on which the states at 3.583 and 3.626 MeV are built. The form factor for the 3<sup>-</sup> state at 3.583 MeV is shown in *fig. 6.15*. The shape of the density resembles that for the 3<sub>1</sub><sup>-</sup> and 5<sub>1</sub><sup>-</sup> states. The fit was done with FOUBES1 and using the FBE for the density. No indication of transverse strength was observed.

### The 7<sup>-</sup> State at 3.626 MeV

This state has been observed before in the studies of the high-spin metastable states of <sup>92</sup>Mo. The cascade 11<sup>-</sup> → 9<sup>-</sup> → 7<sup>-</sup> → 5<sup>-</sup> → 3<sup>-</sup> was observed after <sup>64</sup>Ni and <sup>65</sup>Cu were bombarded with <sup>32</sup>S at 132 MeV. The SM calculation predicts a 7<sup>-</sup> state at nearly this energy (3.370 MeV) and with a configuration suggestive of a  $\pi(1f_{5/2}^{-1}, 1g_{9/2})_{5-} \otimes (2^+)$ . The fit shown in *fig. 6.16* was done by fitting the density obtained for the 7<sub>2</sub><sup>-</sup> (4.560 MeV) state to the data for the 7<sub>1</sub><sup>-</sup> state. The amplitude for this fit is 0.163 ± 0.031 and can be used as a measure of the mixing between *1p1h* and *2p2h* components. Also shown with the density are two curves. The solid curve labeled (A) is a fit using the SPM and a single component,  $\pi(1f_{5/2}^{-1}, 1g_{9/2})$  for the density. Only the amplitude is fit with the result 0.11 ± 0.03. The other curve labeled (B) is the SM prediction.

### The 4<sup>+</sup> State at 3.879

This state has an order of magnitude larger cross section than the state at 3.369 MeV. *Figure 6.16* shows the form factor and fitted density. The fit was done with FOUBES1 using the FBE for the density. The shape of the density is very similar to the 4<sub>1</sub><sup>+</sup> density and indicates a large  $\pi(1g_{9/2}^{-1}, 1g_{9/2})$  component to the transition.

### The 2<sup>+</sup> State at 3.929 MeV

The LP calculation predicts a 2<sup>+</sup> state at 3.930 MeV. The predicted density for this state has approximately equal amplitudes for the

$$\pi(2p_{3/2}^{-1}, 2p_{1/2}), \pi(1f_{5/2}^{-1}, 2p_{1/2}), \text{ and } \pi(1g_{9/2}^{-1}, 1g_{9/2})$$

components. In addition there is a strong  $\nu(1g_{9/2}^{-1}, 2d_{5/2})$  component. *Figure 6.16* shows the fitted density and the BP calculation. The fit was done using FOUBES1 and the FBE model for the density. The shape of the BP density is qualitatively correct and is also of roughly the right magnitude. The shape of the experimental density is very similar to that for the 2<sub>2</sub><sup>+</sup> (3.307 MeV) state in <sup>90</sup>Zr and the 2<sub>1</sub><sup>+</sup> (1.836 MeV) state in <sup>88</sup>Sr. This suggests that the state in <sup>90</sup>Zr and (<sup>92</sup>Mo) is a pair (two pair) of protons coupled to a <sup>88</sup>Sr core in its first excited state.

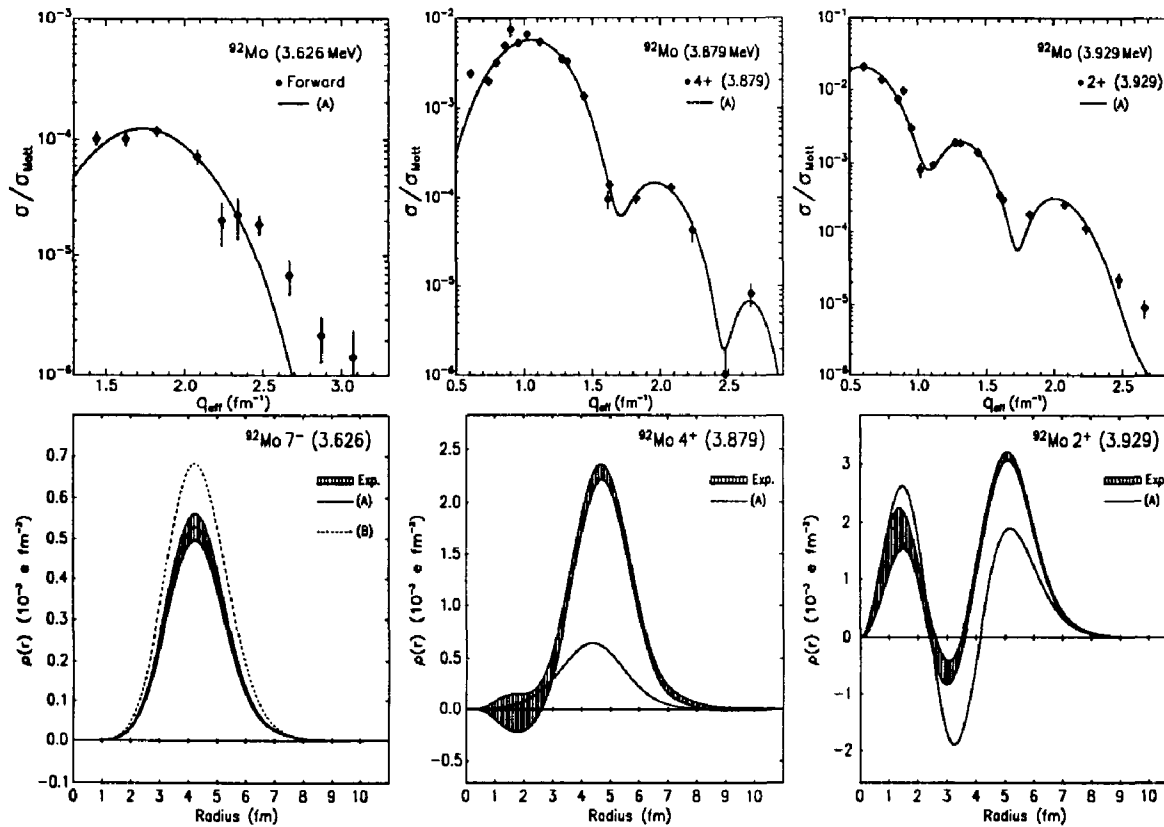


**Figure 6.16** Form factors and transition charge densities for the states at 3.626, 3.879 and 3.925 MeV. The solid curves in the form factor plots are the DWBA fits as described in the text.

## 6.8 STATES BETWEEN 4.0 AND 5.2 MEV

The density of excited states increases rapidly above 4.0 MeV. Neutron pickup reactions on  $^{91}\text{Zr}$  indicate that neutron  $1p1h$  states in  $^{90}\text{Zr}$  begin to appear at an excitation energy of 4.2 Mev. The same situation applies to  $^{92}\text{Mo}$ . The positive parity states based on the  $\nu(1g_{9/2}^{-1}, 2d_{5/2})$  configuration should occur in this excitation region and in part account for the increased level density.

*Figure 6.17* shows a fitted electron spectrum for this excitation region. Above the spectrum are listed the energies at which peaks were included in the peak shape fits. The state at 4.555 MeV has been discussed in a previous section. The two states at 4.690 and 4.925 have backward scattering form factors which indicate that they have unnatural parity and will be discussed in the next section on magnetic transitions. The remaining states in this region for which form factors could be extracted are discussed here.

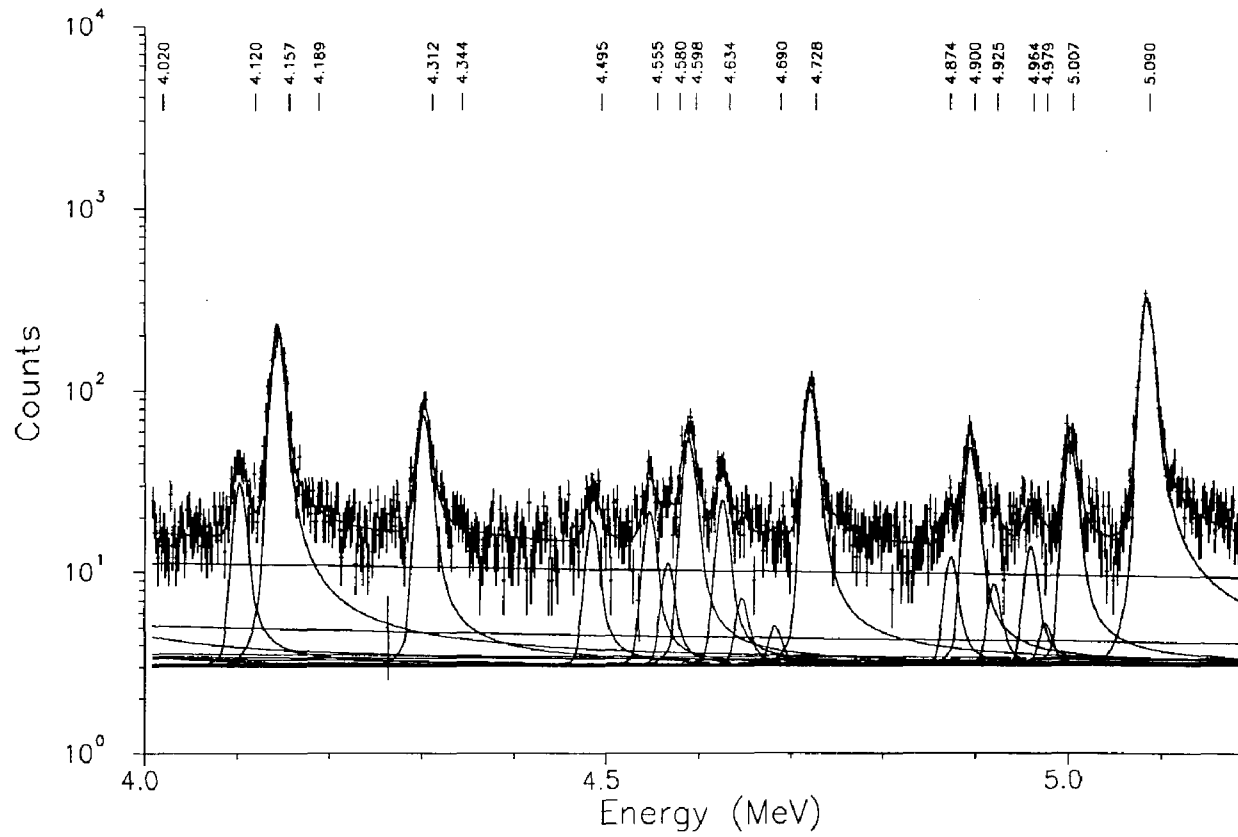


Figure 6.17 Spectrum of 189.6 MeV electrons scattered at  $65.0^\circ$  for the excitation region 4.0 to 5.3 MeV. The energies listed above the spectrum indicate the levels which have been included in the peak shape fits.

### The $5^-$ States at 4.159 and 4.312 MeV

These levels have been observed previously in  $(p, p')$  and  $(\alpha, \alpha' \gamma)$  reactions. The state at 4.159 is actually a doublet of a  $4^+$  state at 4.144 MeV and a  $5^-$  state at 4.159 MeV. The two states are unresolved in this experiment. When the position of the peak in the spectrum is allowed to vary the fitted value of the excitation energy averages to  $4.159 \pm 0.010$  MeV but usually is very near to the energy of the  $5^-$ . In the peak shape fits a single peak width provides a good fit to the data. Both of these observations indicate that the cross section measured is predominantly from the  $5^-$  state.

The BP calculation predicts the second and third  $5^-$  states at 4.323 and 4.549 MeV. A  $4^+$  state which is almost a pure  $\nu(1g_{9/2}^{-1}, 2d_{5/2})$  configuration is predicted at 4.290 MeV. If the  $4^+$  state of this doublet corresponds to the neutron  $1p1h$  state one would expect a rather small  $(e, e')$  cross section. This might explain why there is little evidence for the 4.159 MeV state being a doublet. These BP  $5^-$  states are dominated by  $\pi(1f_{5/2}^{-1}, 1g_{9/2})$  and  $\pi(2p_{3/2}^{-1}, 1g_{9/2})$  components, the two states being roughly orthogonal mixtures of the two components.

*Figure 6.18* shows the form factors for the two levels and the DWBA fits which were done assuming  $J^\pi = 5^-$  for both states. Simultaneous fits were done to the forward and backward scattering data using the program FOUDES2. The densities corresponding to these fits are shown in *fig. 6.19*. Also shown are the densities from the BP calculation.

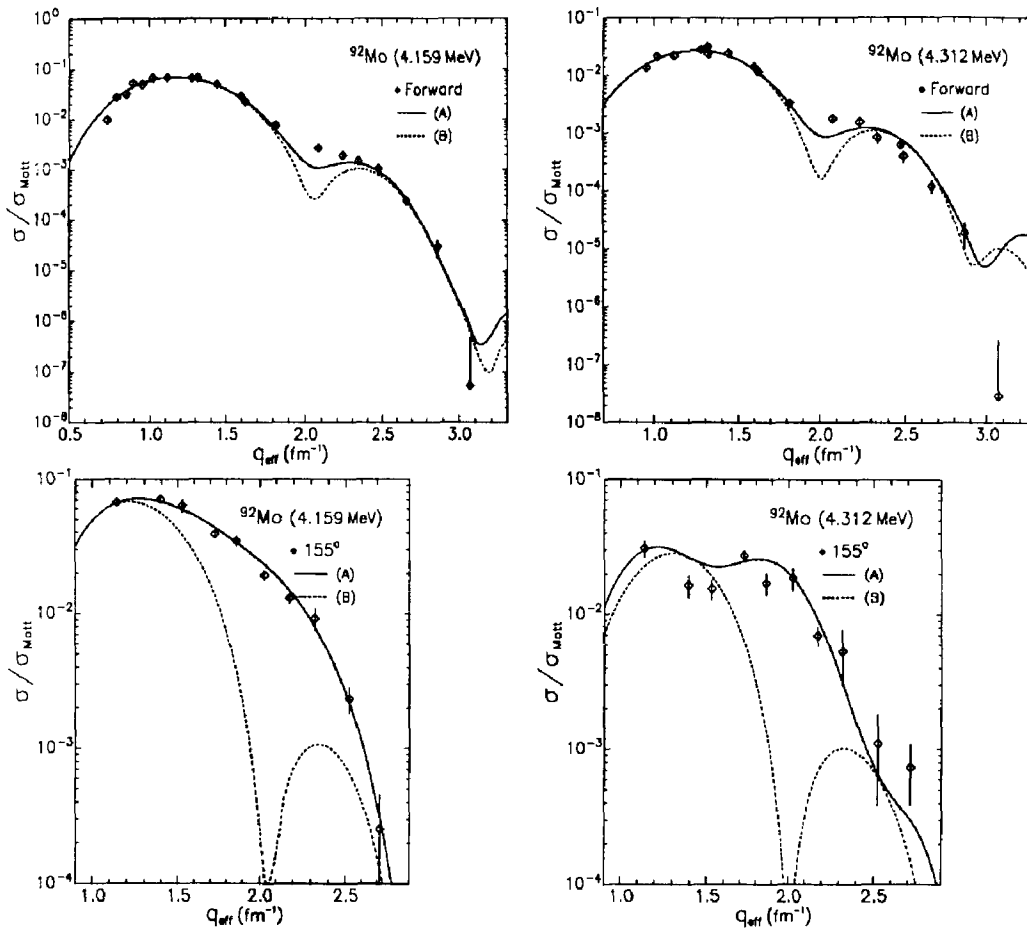
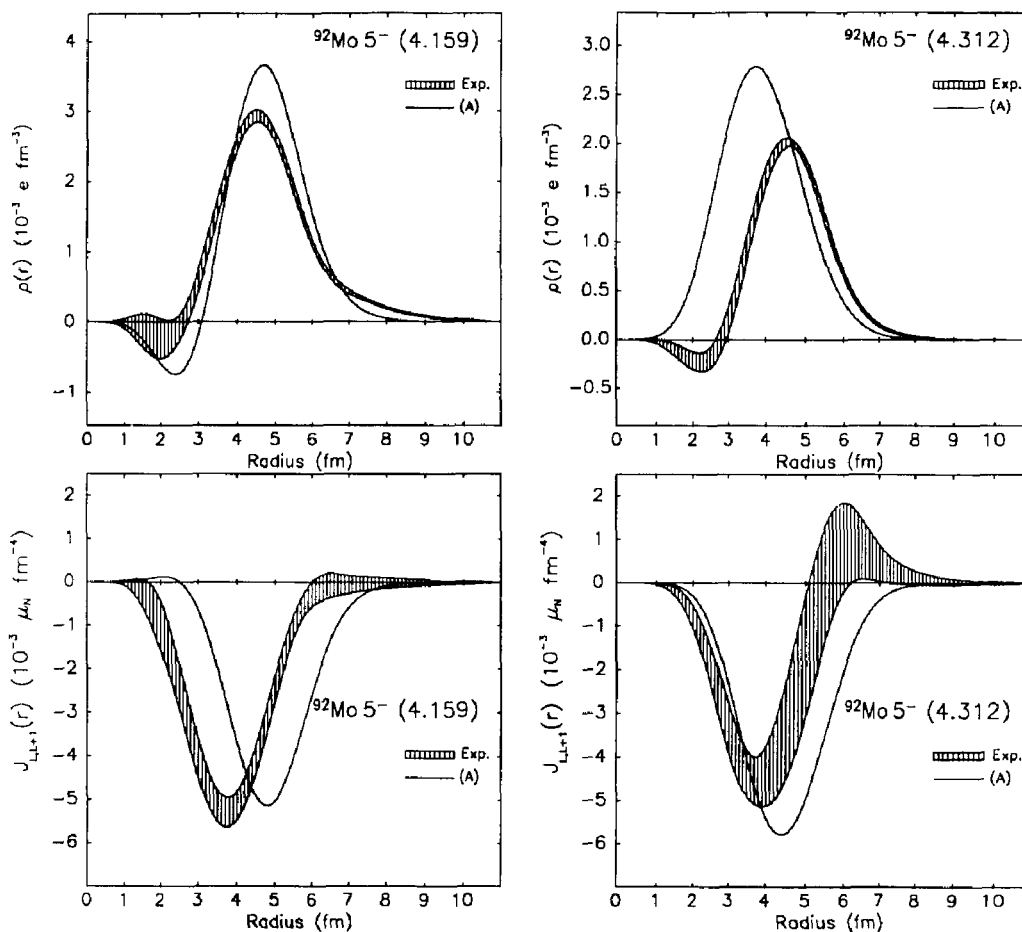


Figure 6.18 Form factors for the states at 4.159 and 4.312 MeV.

### The $2^+$ State at 4.495 MeV

Figure 6.20 shows the form factor and transition density for the  $2^+$  state at 4.495 MeV. The shape of the density indicates a transition between orbitals of different oscillator shells. The most likely  $1p1h$  components are  $\pi(1f_{5/2}^{-1}, 2p_{1/2})$  and  $\pi(1g_{9/2}^{-1}, 2d_{5/2})$ . The broken pair calculation predicts  $2^+$  states, one at 4.479 and the other 4.874 MeV. The state at 4.479 MeV has a dominant component of  $\pi(2p_{3/2}^{-1}, 2p_{1/2})$ . From eq. 5.5 the dominant term in the density is given by the





**Figure 6.19** Densities extracted for the states at 4.159 and 4.312 MeV.

$2p$  radial wavefunction squared. Unlike the measured density this shape will not have a node. The density for the 4.874 MeV BP state is shown in *fig. 6.20* and has a shape which resembles the measured density but which peaks at a larger radius. This BP state has a dominant component of  $\pi(1g_{9/2}^{-1}, 2d_{5/2})$ . The shape of the density favors a strong  $\pi(1f_{5/2}^{-1}, 2p_{1/2})$  component and therefore does not correspond well with either of the BP states.

#### The state at 4.598 MeV

This state is very close to the strong  $7^-$  state at 4.555 MeV. The energy of 4.598 MeV was taken from a state of unknown spin and parity observed in the  $(p, p')$  reaction. From the fits in which the position of the peak could be fit we find the excitation to be  $4.595 \pm 0.010$  MeV. The form factor for this state is shown in *fig. 6.20*. The fit shown was done assuming  $J^\pi = 2^+$  and gives reasonable agreement with the data. This choice of spin and parity was made because of the resemblance between the form factor of this state and that of the  $2^+$  state in  $^{90}\text{Zr}$  at 4.232 MeV. The good agreement supports the assignment of  $J^\pi = 2^+$  but is far from conclusive.

#### The $4^+$ State at 4.724 MeV.

This state was observed in the  $(p, p')$  reaction with  $L=4$  and was given a probable  $J^\pi = 4^+$  assignment. *Figure 6.20* shows the form factor and density for the state at 4.724 MeV. The fitted density has an odd shape due to the excess cross section where the first minimum occurs. There are two possibilities which could explain this. Either there is some transverse strength or there is an unresolved level which contributes to the cross section measured in this q-region. Because this state is in the radiation tail of the state at 4.690 MeV which has a strong transverse form factor no backward scattering data could be obtained for this state. Clearly backward scattering data on this state are necessary to determine the transition charge density.

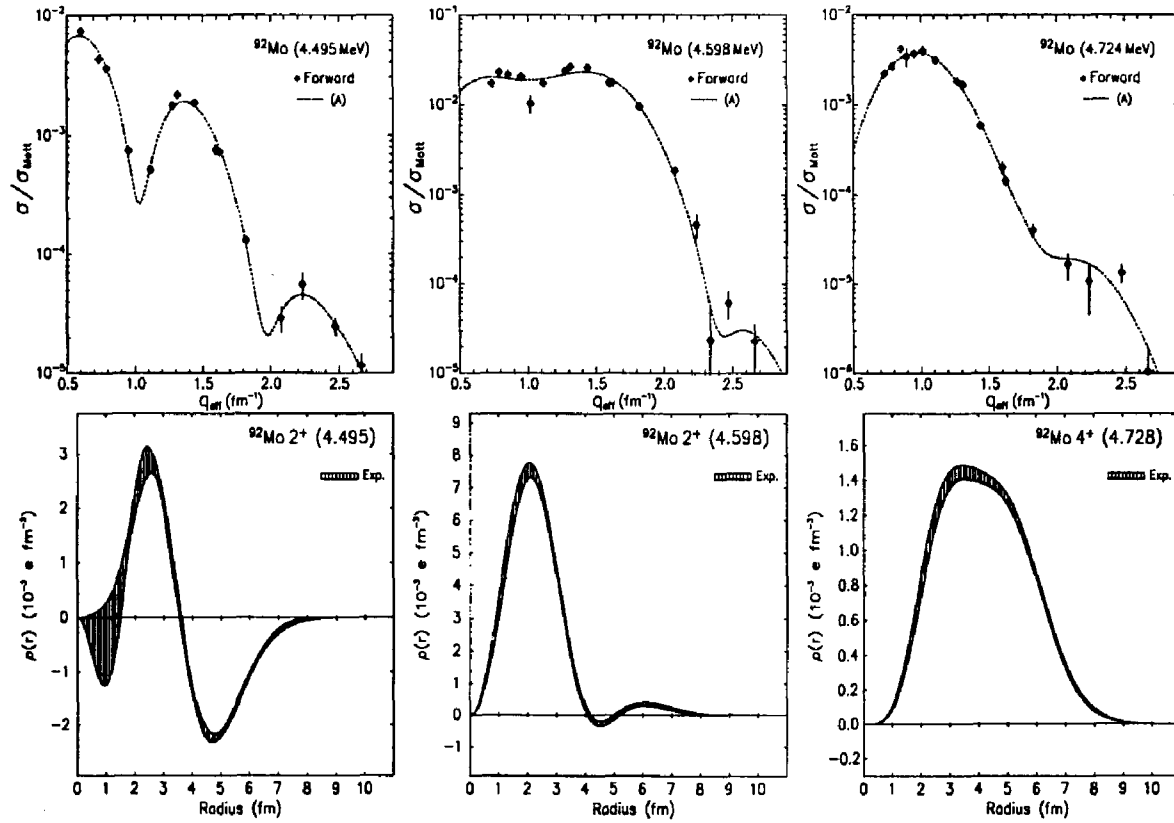
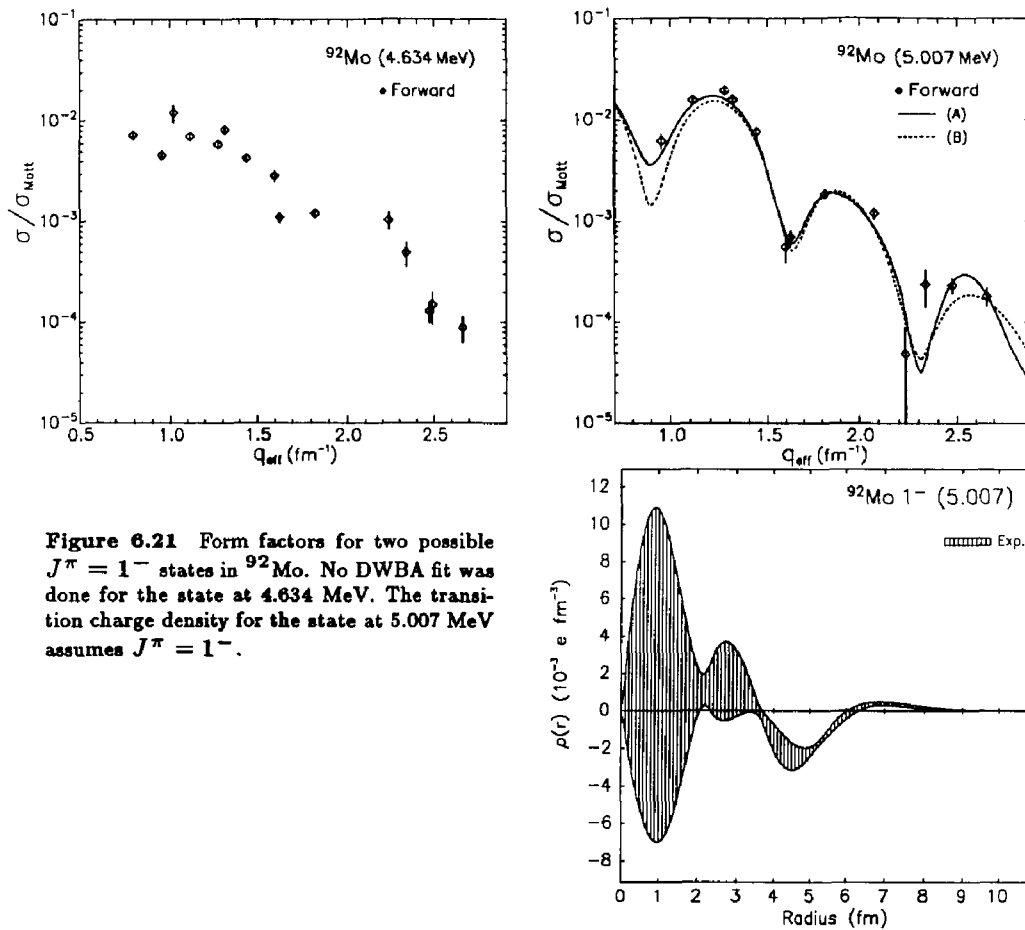


Figure 6.20 Form factors and transition charge densities for the states at 4.495, 4.598, and 4.724 MeV.



**Figure 6.21** Form factors for two possible  $J^\pi = 1^-$  states in  $^{92}\text{Mo}$ . No DWBA fit was done for the state at 4.634 MeV. The transition charge density for the state at 5.007 MeV assumes  $J^\pi = 1^-$ .

**Possible  $1^-$  States at 4.634 and 5.007 MeV**

The BP calculation showed no  $1^-$  states for the excitation region calculated. There are however indications from the  $(\gamma, \gamma')$  reaction that the state at 4.634 MeV is a  $1^-$  state, possibly a two-phonon,  $(E2 \otimes E3)_{1^-}$  state. A similar report was made for the state in  $^{88}\text{Sr}$  at 4.742 MeV. In the analysis of the  $^{88}\text{Sr}$  data the presence of a  $6^-$  state at the same energy prevented the measurement of a form factor for this state. The form factor measured for the 4.634 MeV state in  $^{92}\text{Mo}$  is shown in *fig. 6.21*. Because of the poor quality of the peak shape fits in

this excitation region for the weaker states no DWBA fit was attempted for this level.

The 5.007 MeV state has been observed before but no spin parity assignments have been established. *Figure 6.21* shows the data along with a DWBA fit which was done assuming  $J^\pi = 1^-$ . Many fits were attempted with  $J^\pi = 2^+, 4^+$  and  $1^-$  and making various assumptions about the form of the transition densities. The result of these attempts were that only by letting  $J^\pi = 1^-$  and including two densities (*i.e.* using the program FOUDES2) could a reasonable fit be achieved. In  $^{88}\text{Sr}$  a  $1^-$  state was found at 6.002 MeV but no evidence was found for states at lower energies. The forward scattering data for the state in  $^{88}\text{Sr}$  was well fit assuming a  $\pi(2p_{1/2}^{-1}, 3s_{1/2})$  configuration. This configuration gives a density which peaks well into the interior unlike the density obtained here. A possible  $1^-$  state at 5.089 MeV in  $^{90}\text{Zr}$  was identified in the  $(p, p')$  reaction on  $^{90}\text{Zr}$ <sup>[41]</sup>. No configuration could be found to match the angular distribution of this state. It is likely that the state in  $^{92}\text{Mo}$  at 5.007 corresponds to a similar configuration.

#### The state at 5.088 MeV

This state is part of an unresolved doublet of states at 5.072 MeV ( $L = 4$ ) and 5.088 MeV ( $4^+$ ) both of which were observed in the  $(p, p')$  reaction. The level at 5.088 MeV has also been reported in  $(\alpha, \alpha')$ ,  $(p, t)$  and  $(\alpha, \alpha'\gamma)$  measurements. In the  $(p, p')$  reaction both states were strongly excited, with the 5.074 MeV state having the greater strength. In the analysis of the proton scattering data the 5.074 MeV state was well fit assuming  $L = 4$  while the 5.088 MeV state was not. Its spin parity assignment is from the Nuclear Data Sheets<sup>[42]</sup>.

The  $(e, e')$  data are well fit using a single peak width for the peak shape fits. The energy determined from the location of well isolated levels indicates that the strong peak observed is at  $5.090 \pm 0.010$  MeV. These observations indicate that the cross section observed is mostly due to the single state at 5.088 MeV. *Figure 6.22* shows the form factor and transition density extracted for this state. The fit was

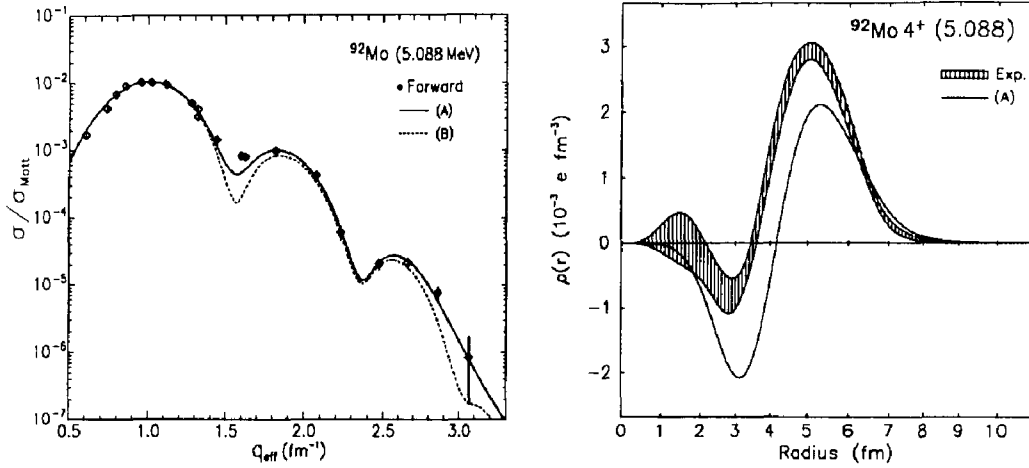


**Figure 6.22** Form factor and transition charge density for the state at 5.088 MeV. The solid curve in the density plot is the BP prediction for a  $4^+$  state at 5.099 MeV.

done for the forward scattering data alone using a FB expansion for the density. This figure also shows the BP calculation for a  $4^+$  state predicted at 5.099 MeV. The main component of this state is  $\pi(1g_{9/2}^{-1}, 2d_{5/2})$ . The experimental density is much larger than a pure  $\pi(1g_{9/2}^{-1}, 2d_{5/2})$  configuration near the surface which probably indicates admixtures of  $\pi(1g_{9/2}^{-1}, 1g_{9/2})$  components.

### 6.9 THE STATES AT 4.690 AND 4.925 MeV

The backward scattering data between 4.0 and 5.3 MeV show three states at 4.555, 4.690 and 4.925 which have transverse form factors which peak at large momentum transfer. This signature is characteristic of high spin states. The  $7^-$  state at 4.555 has been identified and discussed in a previous section. The remaining two states have form factors which indicate that they have unnatural parity and by analogy with the  $^{90}\text{Zr}$  data can be tentatively identified as a  $6^-$  state (4.690 MeV) and a  $7^+$  state (4.925 MeV).

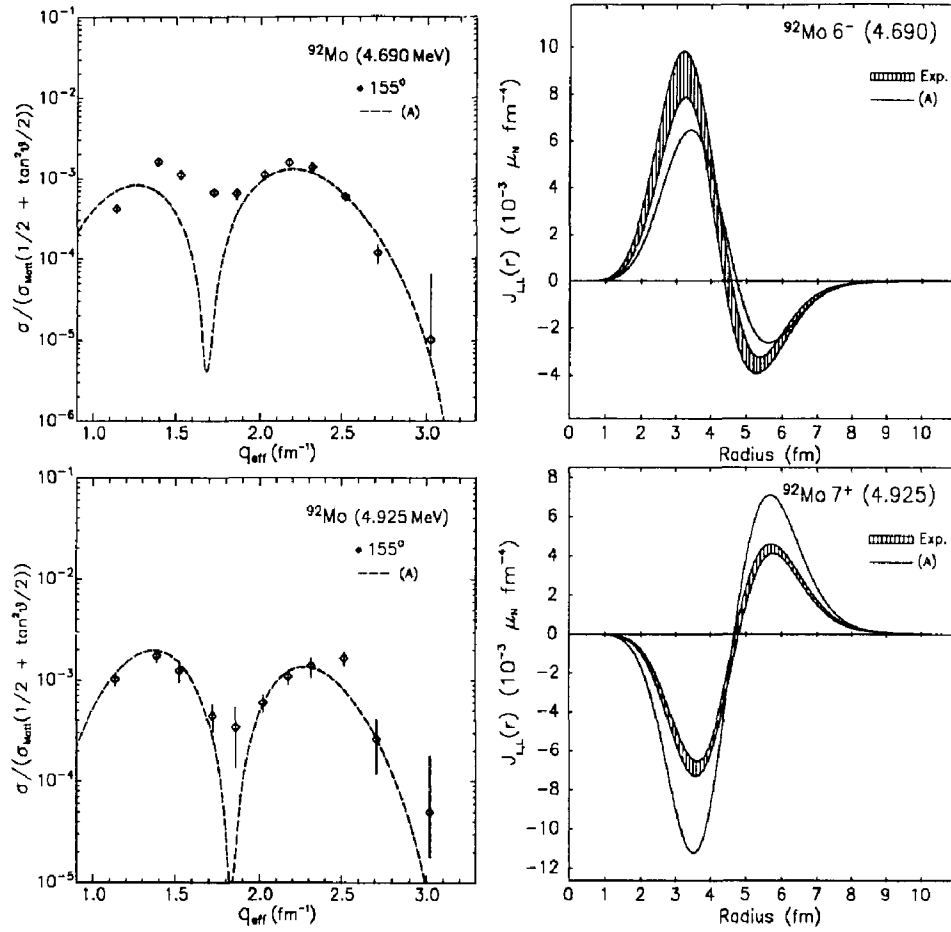


**Figure 6.23** Form factors for the states at 4.690 and 4.925 MeV. Also shown are the transition current densities for states and the BP predictions for the first  $6^-$  and  $7^+$  states.

The data for these states is shown in *fig. 6.23* along with the fits to the M6 and M7 form factors. Both fits were done to the backward scattering data alone using the SPM. The form of the density for the  $6^-$  state was taken to be  $\alpha\pi(1f_{5/2}^{-1}, 1g_{9/2}) + \beta\pi(2p_{3/2}^{-1}, 1g_{9/2})$ . The Woods-Saxon well radius for the  $\pi 1g_{9/2}$  orbit was fixed at 1.332 times  $A^{1/3} \text{ fm}$ . A single radius parameter for the

$\pi 2p_{3/2}$  and  $\pi 1f_{5/2}$  orbits and the amplitudes  $\alpha$  and  $\beta$  were fit. For the  $7^+$  fit a single component a  $\nu(1g_{9/2}^{-1}, 2d_{5/2})$  was used and the amplitude and a single radius parameter for both orbits were fit.

Both states appear to be unresolved from nearby states. The low- $q$  forward scattering data show excess cross section indicative of a nearby natural parity state while the high- $q$  forward scattering data agree well with the fits. A known  $3^-$  state at 4.920 MeV is the most likely source of the excess cross section for the  $7^+$  state. While several states near 4.690 MeV have been identified in the  $(p, p')$  reaction the spin and parity of these states have not been established. Further analysis and/or additional data are necessary to separate the magnetization densities accurately. The densities that were fitted are shown in *fig. 6.23* along with the BP predictions for the first  $6^-$  and  $7^+$  states. The BP states were predicted at excitation energies of 4.624 and 4.778 MeV respectively.



## 7. Summary and Conclusions

In this experiment differential cross sections have been measured for over 30 states in  $^{92}\text{Mo}$ . The determination of the groundstate charge density has been improved by extending the range of momentum transfer over which elastic scattering cross sections have been measured to  $3.1\text{ fm}^{-1}$ . This improvement allows a more accurate determination of the groundstate charge difference between  $^{90}\text{Zr}$  and  $^{92}\text{Mo}$ . In particular the difference has been determined well into the nuclear interior where structure is observed similar to that predicted in an HFDME calculation. An extension of this analysis to include  $^{88}\text{Sr}$  and  $^{89}\text{Y}$  would allow a comparison for  $N=50$  nuclei similar to the comparison for the  $Z=82$  nuclei.

A great deal of information has been collected on the excited states of  $^{92}\text{Mo}$  and cross sections have been measured for over 30 states. We have identified a strongly excited  $7^-$  state at 4.555 MeV. Two other high-spin states a likely  $6^-$  at 4.690 MeV and a  $7^+$  at 4.925 MeV have also been identified. These three states should provide useful information for establishing single particle energies used in model calculations. The state at 3.369 MeV previously given a tentative spin-parity assignment of  $4^-$  now can be identified as a  $4^+$ . A state at 5.007 MeV has been tentatively identified as a  $1^-$  state.

DWBA fits to the cross section data enabled the extraction of transition densities for 22 excited states below 5.2 MeV. A comparison of these densities with nuclear model calculations provides insight both into the structure of the states and also into the models used for comparison. In general the models give only qualitative agreement but the comparisons point to several densities which should provide ideal test cases for further modeling efforts.

The densities for the  $2^+$  to  $8^+$  multiplet have now been accurately determined for both  $^{90}\text{Zr}$  and  $^{92}\text{Mo}$ . Both of the calculations used for comparison here do not include enough collectivity to account for the strength of the E2 transition. At the same time both calculations overpredict the strength of the E8 transition to the  $8^+$  state which has been shown to have very little collectivity. The densities all

arise from the same dominant configuration , but with different amounts of core polarization depending on the multipolarity. Correctly predicting the densities for all four states provides a stringent test for model calculations.

The transition densities for the  $3^-$  state at 2.850 Mev also provide useful information on the collectivity which must be included in a realistic model. It has been shown that this state has a non-zero transition current density. This current density is well described both in shape and strength by the BP calculation which predicts a strong  $\pi(2p_{3/2}^{-1}, 1g_{9/2})$  component to the transition. The BP prediction for strength of the transition charge density however is considerably smaller than measured. Again the model does not include enough collectivity for the transition charge. The good agreement with the current density seems to indicate that the particle-hole nature of the state is well predicted.

The comparison of the E5 transition strengths has been extended to  $^{92}\text{Mo}$ . The quenching of the transition current relative to the transition charge was again observed. The analysis of the  $^{92}\text{Mo}$  data further supports the idea that the quenching is due to backward going particle-hole amplitudes. The quenching factors determined for  $^{89}\text{Y}$ ,  $^{90}\text{Zr}$  and  $^{92}\text{Mo}$  should provide a clear signature for the correctness of model groundstate occupations.

Finally, the most intriguing data comes from the particle-hole  $7^-$  state at 4.555 MeV. The particle-hole states based on the  $\pi(1f_{5/2}^{-1}, 1g_{9/2})$  configuration have now been identified in  $^{88}\text{Sr}$ ,  $^{90}\text{Zr}$  and  $^{92}\text{Mo}$ . In all three nuclei the strength of the transition for both the current and charge densities is significantly less (20 to 30%) than would be found for a pure particle-hole transition. This quenching is as yet unexplained and very surprising for a state which should have a simple configuration. Another interesting feature of this state is that the transition current density peaks farther into the nuclear interior than is expected. A fit using the SPM and a single component for the density does not provide a good fit to both the forward scattering and backward scattering data. If a separate radius parameter is fit for the current density calculation a good fit can be achieved.

Again, this is unexplained and neither the quenching nor the radius shift seem to be within the scope of the conventional nuclear models employed in this analysis.

## Bibliography

1. O. Schwentker, J. Dawson, J. Robb, J. Heisenberg, J. Lichtenstadt, C. N. Papanicolas, J. Wise, J. S. McCarthy, L. T. van der Bijl and H. P. Blok, *Phys. Rev. Lett.* **50** (1983) 15.
2. O. Schwentker, J. Dawson, S. McCaffrey, J. Robb, J. Heisenberg, J. Lichtenstadt, C. N. Papanicolas, J. Wise, J. S. McCarthy, N. Hintz, and H. P. Blok, *Phys. Lett.* **112B** (1982) 40.
3. J. Heisenberg, J. F. Dawson, T. Milliman, O. Schwentker, J. Lichtenstadt, C. N. Papanicolas, J. Wise, J. S. McCarthy, N. Hintz, and H. P. Blok,, *Phys. Rev.* **C29** (1984) 97.
4. T. E. Milliman, J. H. Heisenberg, F. W. Hersman, J. P. Connelly, C. N. Papanicolas, J. E. Wise, H. P. Blok, L. T. van der Bijl, *Phys. Rev.* **C32** (1985) 805.
5. G. Vourvopoulos and J. D. Fox, *Phys. Rev.* **177** (1969) 1558.
6. M. R. Cates, et al., *Phys. Rev.* **187** (1969) 1682.
7. K. T. Knopfle, M. Rogge, C. Mayer-Boricke, J. Pedersen and D. Burch, *Nucl. Phys.* **A159** (1971) 642.
8. W. J. Courtney and H. T. Fortune, *Phys. Lett.* **41B** (1972) 4.
9. B. Frois, J. M. Cavedon, D. Goutte, M. Huet, Ph. Leconte, C. Papanicolas, X.-H. Phan, S. K. Platchkov, S. E. Williamson, *Nucl. Phys.* **A396** (1983) 409c.
10. V. R. Pandharipande, C. N. Papanicolas and J. Wambach, *Phys. Rev. Lett.* **53** (1984) 1133.
11. T. deForest and J. D. Walecka, "Electron Scattering and Nuclear Structure", *Adv. in Phys.* **15** (1966) 1.
12. H. Uberall, *Electron Scattering from Complex Nuclei*, (Academic, New York, 1971).

13. J. D. Walecka, *Electron Scattering - Lectures given at Argonne National Laboratory*, NTIS Report ANL-83-50 (1983).
14. R. Hofstadter, "Nuclear and Nucleon Scattering of High-Energy Electrons", *Ann. Rev. Nucl. Sci.* **7** (1971) 231.
15. J. Heisenberg, "Nuclear Transition Density Determination from Inelastic Electron Scattering", *Adv. Nucl. Phys.* **12** (1981) 61.
16. S. T. Tuan, L. E. Wright, D. S. Onley, *Nucl. Instrum. and Meth.* **60** (1968) 70.
17. H. C. Lee, Atomic Energy of Canada, Report AECL-4839, Chalk River, Ontario (1975).
18. J. Bergstrom, MIT 1967 Summer Study: Medium Energy Nuclear Physics with Electron Linear Accelerators, (1967) 251.
19. L. Maximon, MIT 1967 Summer Study: Medium Energy Nuclear Physics with Electron Linear Accelerators, (1967) 249.
20. M. Deady, Ph. D. Thesis, MIT, 1981 (unpublished).
22. W. Bertozzi, M. V. Hynes, C. P. Sargent, W. Turchinets, and C. Williamson, *Nucl. Instrum. Methods* **162** (1979) 211.
23. W. Bertozzi, M. V. Hynes, C. P. Sargent, C. Cresswell, P. C. Dunn, A. Hirsh, M. Seitch, B. Norum, F. N. Rad, T. Sasanuma, *Nucl. Instrum. Methods* **141** (1977) 457.
24. F. W. Hersman, Ph. D. Thesis, MIT 1983 (unpublished).
25. A copy of this program can be obtained from Jim Kelly, Physics Department, Univ. of Maryland
26. C. Creswell, MIT Internal Report No. 761 (1976).
27. P. R. Bevington, *Data Reduction and Data Analysis*, McGraw-Hill, New York (1969).

28. B. Dreher, Ph. D. thesis, Universitat Mainz, 1974 (unpublished).
29. Phan Xuan Ho, J. B. Bellicard, A. Bussiere, Ph. Leconte, and M. Priou, *Nucl. Phys.* **A179** (1972) 529.
30. R. P. Singhal, S. W. Brain, C. S. Curran, T. E. Drake, W. A. Gillespie, A. Johnston and E. W. Lees, *Nucl. Phys.* **A216** (1973) 29.
31. L. Schellenberg, B. Robert-Tissot, K. Kaser, L. A. Schaller, H. Schneuwly, G. Fricke, S. Glukert, G. Mallot, E. B. Shera, *Nucl. Phys.* **A333** (1980) 333.
32. B. Dreher, J. Friedrich, K. Merle, and G. Luhrs, *Nucl. Phys.* **A235** (1974) 219.
33. J. Heisenberg and H. P. Blok, "Inelastic Electron Scattering from Nuclei", *Ann. Rev. Nucl. Part. Sci.* **33** (1983) 569.
34. G. G. Simon, C. Schmitt, F. Borkowski, and F. W. Walther, *Nucl. Phys.* **A333** (1980) 381.
35. J. W. Negele and D. Vautherin, *Phys. Rev.* **C5** (1972) 1472.
36. W. C. Haxton, private communication. See also M. M. Gazzaly, N. M. Hintz, M. A. Franey, J. Dubach, and W. C. Haxton, *Phys. Rev.* **C28** (1983) 294.
37. R. R. Whitehead, *Nucl. Phys.* **A182** (1972) 290.
38. R. R. Whitehead, A. Watt, B. J. Cole, I. Morrison, "Computational Methods for Shell-Model Calculations", *Adv. Nucl. Phys.* **9** (1977) 123.
39. K. Allaart, Vrije Universiteit, Private communication.
40. J. M. Cavedon, B. Frois, D. Goutte, M. Huet, Ph. Leconte, X. H. Phan, S. K. Platchkov, C. N. Papanicolas, S. E. Williamson, W. Boeglin, I. Sick, and J. Heisenberg, to be published.
41. L. T. van der Bijl, Ph. D. Thesis, Vrije Universiteit, 1982 (unpublished).

42. P. Luksch, *Nucl. Data Sheets* **30** (1980) 573.
43. J. Heisenberg, *Com. Nucl. Part. Phys.* **13** (1984) 267.
44. J. Piccard and G. Bassani, *Nucl. Phys.* **A131** (1969) 636.
45. R. L. Kozub and D. H. Youngblood, *Phys. Rev.* **C4** (1971) 535.
46. P. X.-Ho, J. Bellicard, Ph. Leconte, and I. Sick, *Nucl. Phys.* **A210** (1973) 189.
47. S. Platchkov, J. B. Bellicard, J. M. Cavedon, B. Frois, D. Goutte, M. Huet, P. Leconte, Phan Xuan Ho, P. K. A. deWitt Huberts, L. Lapikas, and I. Sick, *Phys. Rev.* **C25** (1982) 2318.
48. A. M. Selig, I. E. Zacharov, P. K. A. de Witt Huberts, S. K. Platchkov, to be published.
49. E. J. Kaptein, Ph. D. Thesis, Vrije Universiteit, 1978 (unpublished).
50. R. Klein, Ph. D. Thesis, Heidleberg, 1984.

## Appendix A

### On-line Data Processing

The on-line data processing must be done correctly for the data to be meaningful. An understanding of the details of this processing is not essential for understanding the results. Some of these details do however effect the reliability of the results. In particular, understanding the corrections applied to the data requires some knowledge of the on-line processing. A brief overview is presented here to define some of the terms and concepts used in discussing the corrections to the data. The discussion assumes some familiarity with multi-wire proportional chambers. The one-chamber readout system is described in detail in Bertozzi, *et al.*<sup>[23]</sup>.

The rawdata used to reconstruct the electron track and eventually the data histograms is all in the form of digitized times. A coincidence between two Čerenkov detectors provides reference relative to which these times are measured. This coincidence signal is labeled a *start* and all *starts* are counted with a hardware scaler. If two starts occur within 300ns the times associated with neither start can be recorded and both starts are 'vetoed.' These *vetoed* are counted with a hardware scaler. If the data rate is high the rate at which data buffers are being filled may exceed the capacity the system . The information will be lost outside of being recorded as a *start*. It is also possible that the data buffers are filled at a rate which exceeds the rate at which they can be processed. This will result in some buffers not being processed. These *unprocessed buffers* are also counted but the contents of the buffer is lost. An *event* refers to a data buffer which has been sucessfully recorded and processed.

The time information for *events* comes from the remaining detectors shown in *fig. 3.3*. The VDC's each use a three delay-line readout system as is described in Bertozzi, *et al.*<sup>[23]</sup>. Briefly, each delay line yields two times, one for each end of the delay line. The difference in the two times determines which wire on the



delay-line has registered a pulse (has been 'hit') and the sum of the two times is used to determine a drift-time. In principle an electron which has passed through the spectrometer will produce a 'hit' on each of the three delay-lines for a VDC corresponding to three adjacent wires in the chamber. The wire numbers and drift-times can then be used to calculate the position and vertical angle for the electron as it passed through the VDC. The readout for the TA is simpler in that there is a single delay line and only the transverse position (*i.e.* wire number) is calculated.

Following a *start* the TDC's record stops from the delay lines for 300ns. The TDC's then digitize the times which takes about about 20  $\mu$ s. After the times are digitized an interrupt is generated, the data buffer is transferred to the PDP-11/45 for further processing and the TDC's are reset. The data are first processed according to the one-chamber system (VDCI + TA). The *events* are first classified as follows,

*four-hit events* all 4 delay-lines (3 for VDCI and 1 for the TA) recorded times on both ends.

*missing hits* - Neither of the two times for at least one delay-line were recorded. The remaining delay lines all had 'good hits' (*i.e.* times were recorded for both ends of the delay line.)

*inconsistent hits* - At least one delay-line recorded only a single time. The two ends of the delay-line were not consistent.

*rollovers* - No delay-line recorded a 'good hit.'

The *rollovers* are merely counted then discarded. Buffers with no consistent VDC hits are also counted and discarded. The remaining buffers all have at least one VDC hit which is consistent and coarse channel numbers and drift times can be calculated for these buffers. Coarse spectra are formed of the *missing hits* and *inconsistent hits* before they are also discarded. An exception is made for

buffers which have good hits on all three VDC delay lines (ie. *missing TA only* and *inconsistent TA only* data). These buffers are processed further along with the *four-hit events* but do not enter the final data histograms.

The remaining cuts on the *four-hit events* insure that the electron track is due to an electron which scattered from the target through the spectrometer without obstruction. The majority of *four-hit events* end up in the 1-chamber data histograms and are labeled *good 1-chamber events*. The *four-hit events* which are discarded fall in to several categories,

1. *early delay-line time out-of-range*
2. *early delay-line position out-of-range*
3. *TA time out-of-range*
4. *TA position out-of-range*
5. *inconsistent side delay-line*
6. *vertical angle out-of-range*

These categories are for the most part self-explanatory. If a quantity is out-of-range it leads to a calculated trajectory which could not have passed through the spectrometer cleanly. Category 5 consists of the buffers for which the wire with the shortest drift time is not in the middle of the the 3 wires which recorded the hits. Coarse diagnostic spectra are formed of the categories 2, 3, 5, and 6 before these buffers are discarded. *Events* which survive all the cuts are labeled *good one-chamber events*. A fine (3072 channel) spectra of these data which includes kinematic and aberrative corrections is formed. If the second VDC is not operational this spectra serves as the final data histograms.

If the second VDC is operational all the data which survive the one-chamber cuts are processed further. For each event buffer the times from the three delay-lines of the second chamber are analyzed along the same lines as for VDCI. An

*event* for the second chamber is a *good one-chamber event*. Buffers which have *missing hits, inconsistent hits* or are *rollovers* with respect to VDCII are counted then discarded. The remaining cuts for the second chamber are equivalent to the categories 1, 2, 5 and 6 for the *four-hit events* of the first chamber. Events which survive all these cuts are *good two-chamber events*. The additional information from the second VDC is used to refine the vertical angle calculation. With new values the kinematic and aberrative corrections are calculated and an extra-fine (6144 channel) spectrum is formed. This spectrum normally serves as the final data histogram.

## Appendix B

### Cross Section Summary

This Appendix contains a summary of the data analysis for the  $^{92}\text{Mo}$  experiment. *Table B.1* shows the levels included in the forward scattering peak-shape fitting. Following *table B.1* there is a one-page summary of the cross section data for each level discussed in Chapter 6. *Table B.2* contains the equivalent information for the backward scattering data. Again this is followed by a one page summary for each level observed.

A considerable amount of the data received only a cursory analysis. In particular peak-shape fitting for the excitation region between 5.3 and 7.6 Mev was done only for the 189.6 MeV data set. The high level density in this region demands that considerable care be taken when doing the peak-shape fitting. In addition the reliability of the channel-to-energy calibrations must be questioned in excitation regions where there are few known levels. *Figure B.32* , which shows one of the fits for this region, illustrates the difficulty involved and the information that is available.

Summary of Forward Scattering Data Analysis				
N	$E^*$ (MeV)	$J^\pi$	Number of $q$ -points	DWBA fit done (yes/no)
1	1.509	$2^+$	28	yes
2	2.282	$4^+$	25	yes
4	2.527	$5^-$	28	yes
5	2.612	$6^+$	24	yes
6	2.760	$8^+$	19	yes
7	2.850	$3^-$	28	yes
8	3.096	$2^+$	27	yes
9	3.369	$4^+ \dagger$	14	yes
10	3.545	$2^+$	21	yes
11	3.583	$3^-$	24	yes
12	3.626	$7^-$	12	yes
13	3.879	$4^+$	24	yes
14	3.929	$2^+$	23	yes
15	4.020		3	no
16	4.120		12	no
17	4.159	$5^-$	23	yes
18	4.189		3	no
19	4.312	$5^-$	21	yes
20	4.344		4	no
21	4.495	$2^+$	23	yes
22	4.555	$7^- \dagger$	20	yes
23	4.598	$2^+ \dagger$	21	yes
24	4.634		19	no
25	4.690	$(6^-) \dagger$	18	yes
26	4.724	$4^+$	22	yes
27	4.879		14	no*
28	4.900	$4^+$	15	no*
29	4.925	$7^+ \dagger$	23	yes
30	4.964		14	no
31	4.979	$L=4$	15	no
32	5.007	$(1^-) \dagger$	21	yes
33	5.090	$4^+$	25	yes

\*DWBA fit may be possible but was not attempted.  
†Spin-parity assignment determined in this experiment.

Table B.1 Summary of forward scattering data analysis. The spin-parity assignment were taken from *Refs.* 48, 49 or 50 unless otherwise noted.

Normalized Cross Sections for level at 0.000 MeV					
$E(\text{MeV})$	$\theta$ ( $^\circ$ )	$d\theta$ ( $^\circ$ )	$d\phi$ ( $^\circ$ )	$\sigma(\text{mb/sr})$	$d\sigma(\text{mb/sr})$
189.6	45.0	0.26	0.55	1.344E-01	2.690E-03
189.6	54.8	0.30	0.91	2.582E-02	5.180E-04
189.6	65.0	0.37	1.46	1.128E-02	2.260E-04
189.6	76.0	0.55	2.14	2.417E-03	4.870E-05
189.6	88.0	0.56	3.27	1.766E-04	3.650E-06
189.6	101.0	0.56	3.27	3.631E-05	8.760E-07
279.1	75.3	0.75	3.64	5.865E-05	2.380E-06
279.1	88.4	0.75	3.64	2.373E-06	1.150E-07
279.1	97.1	0.75	3.64	5.670E-07	4.540E-08
365.1	74.7	0.75	3.64	1.722E-06	1.150E-07
104.5	40.0	0.08	0.07	2.334E+01	8.520E-01
104.5	60.0	0.68	0.22	1.284E+00	4.510E-02
104.5	75.0	0.68	0.36	1.204E-01	4.270E-03
130.4	75.0	0.19	1.82	1.593E-02	5.880E-04
364.6	40.0	0.68	3.27	5.384E-03	1.890E-04
364.6	50.0	0.68	3.27	1.941E-04	6.990E-06
366.7	79.5	0.68	3.27	1.245E-06	6.990E-08
366.7	79.5	0.68	3.27	1.257E-06	5.940E-08
366.7	87.0	0.68	3.27	2.180E-07	1.330E-08
366.7	95.5	0.75	3.64	6.310E-09	1.160E-09
366.7	105.0	0.75	3.64	8.141E-10	4.300E-10

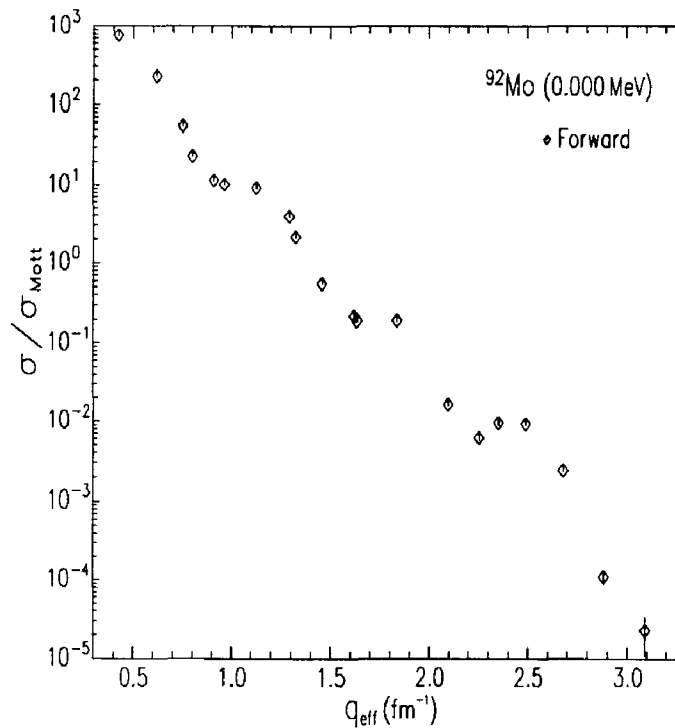


Figure B.1 Data for elastic scattering in forward directions.

Normalized Cross Sections for level at 1.509 MeV					
$E(\text{MeV})$	$\theta$ ( $^\circ$ )	$d\theta$ ( $^\circ$ )	$d\phi$ ( $^\circ$ )	$\sigma(\text{mb/sr})$	$d\sigma(\text{mb/sr})$
189.6	45.0	0.26	0.55	6.021E-03	1.240E-04
189.6	54.8	0.30	0.91	1.099E-03	2.380E-05
189.6	65.0	0.37	1.46	8.634E-05	2.390E-06
189.6	76.9	0.55	2.14	3.880E-05	1.010E-06
189.6	88.0	0.56	3.27	2.944E-05	6.990E-07
189.6	101.0	0.56	3.27	7.987E-06	2.810E-07
279.1	75.3	0.75	3.64	9.889E-07	6.530E-08
279.1	88.4	0.75	3.64	6.337E-07	4.240E-08
279.1	97.1	0.75	3.64	3.039E-07	3.130E-08
365.1	74.7	0.75	3.64	2.818E-07	4.270E-08
104.5	40.0	0.60	0.20	2.102E-02	8.030E-04
104.5	90.0	0.75	3.27	9.635E-04	3.500E-05
104.5	60.0	0.68	0.22	8.625E-03	4.240E-04
104.5	60.0	0.56	2.55	8.293E-03	2.990E-04
104.5	75.0	0.68	0.36	2.921E-03	1.490E-04
104.5	75.0	0.60	2.91	2.847E-03	1.030E-04
130.4	75.0	0.19	1.82	1.055E-03	6.110E-05
364.6	40.0	0.68	3.27	1.900E-04	7.530E-06
364.6	50.0	0.68	3.27	3.499E-05	1.410E-06
366.7	79.5	0.68	3.27	6.957E-08	1.330E-08
366.7	79.5	0.68	3.27	7.690E-08	1.030E-08
366.7	87.0	0.68	3.27	9.113E-09	2.280E-09
366.7	95.5	0.75	3.64	6.690E-09	1.210E-09
366.7	105.0	0.75	3.64	6.720E-10	3.940E-10

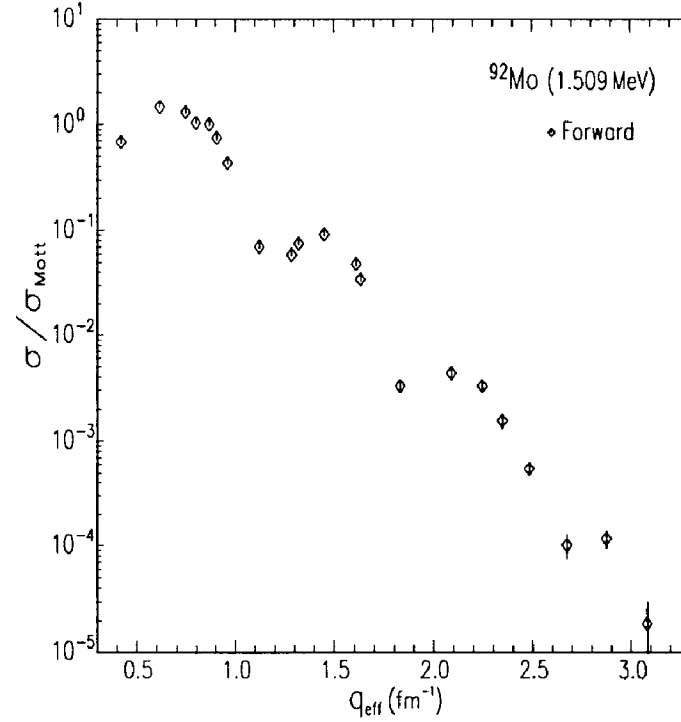


Figure B.2 Data for scattering in forward directions from state at 1.509 MeV.

Normalised Cross Sections for level at 2.282 MeV					
$E(\text{MeV})$	$\theta$ (°)	$d\theta$ (°)	$d\phi$ (°)	$\sigma(\text{mb/sr})$	$d\sigma(\text{mb/sr})$
189.6	45.0	0.26	0.55	$7.814E-04$	$1.930E-05$
189.6	54.8	0.30	0.91	$6.022E-04$	$1.390E-05$
189.6	65.0	0.37	1.46	$3.109E-04$	$6.970E-06$
189.6	76.0	0.55	2.14	$1.077E-04$	$2.460E-06$
189.6	88.0	0.56	3.27	$2.010E-05$	$5.080E-07$
189.6	101.0	0.56	3.27	$1.101E-06$	$8.930E-08$
279.1	75.3	0.75	3.64	$1.106E-06$	$7.070E-08$
279.1	88.4	0.75	3.64	$6.292E-07$	$4.240E-08$
279.1	97.1	0.75	3.64	$1.135E-07$	$1.830E-08$
365.1	74.7	0.75	3.64	$6.484E-08$	$2.020E-08$
104.5	90.0	0.75	3.27	$1.658E-04$	$6.990E-06$
104.5	60.0	0.56	2.55	$1.518E-04$	$1.110E-05$
104.5	75.0	0.60	2.91	$1.825E-04$	$9.010E-06$
130.4	75.0	0.19	1.82	$2.741E-04$	$2.670E-05$
364.6	40.0	0.68	3.27	$3.872E-04$	$1.450E-05$
364.6	50.0	0.68	3.27	$5.868E-06$	$3.530E-07$
366.7	79.5	0.68	3.27	$1.886E-08$	$6.870E-09$
366.7	79.5	0.68	3.27	$1.506E-08$	$4.470E-09$
366.7	87.0	0.68	3.27	$2.026E-08$	$3.470E-09$
366.7	95.5	0.75	3.64	$5.110E-09$	$1.060E-09$
366.7	105.0	0.75	3.64	$3.045E-12$	$2.640E-11$

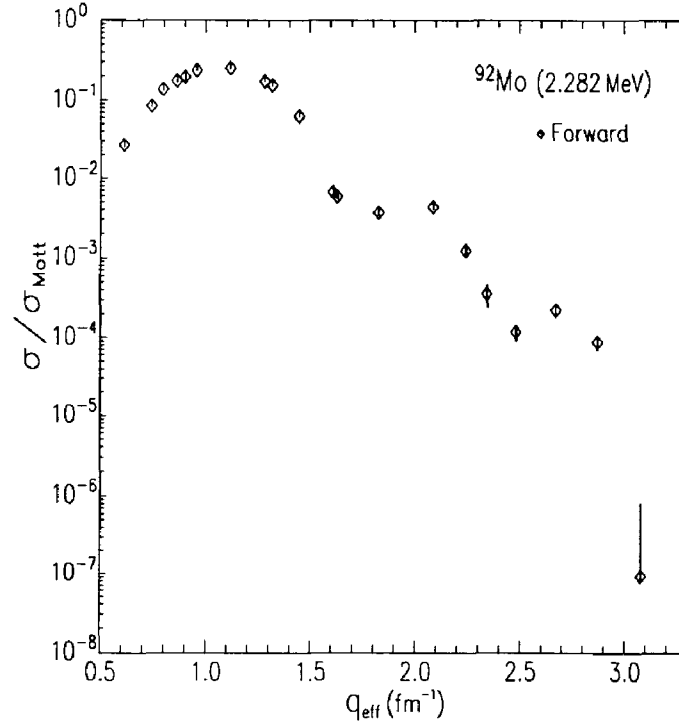


Figure B.3 Data for scattering in forward directions from state at 2.282 MeV.



Normalized Cross Sections for level at 2.527 MeV					
$E(\text{MeV})$	$\theta$ ( $^\circ$ )	$d\theta$ ( $^\circ$ )	$d\phi$ ( $^\circ$ )	$\sigma(\text{mb/sr})$	$d\sigma(\text{mb/sr})$
189.6	45.0	0.28	0.55	2.849E-04	8.880E-06
189.6	54.8	0.30	0.91	2.818E-04	7.340E-06
189.6	65.0	0.37	1.46	2.015E-04	4.760E-06
189.6	76.0	0.55	2.14	1.161E-04	2.630E-06
189.6	88.0	0.56	3.27	4.416E-05	9.980E-07
189.6	101.0	0.56	3.27	9.505E-06	3.180E-07
279.1	75.3	0.75	3.64	1.123E-06	7.170E-08
279.1	88.4	0.75	3.64	8.771E-07	5.350E-08
279.1	97.1	0.75	3.64	6.989E-07	5.230E-08
365.1	74.7	0.75	3.64	9.485E-07	8.220E-08
104.5	90.0	0.75	3.27	5.821E-05	3.090E-06
104.5	75.0	0.60	2.91	4.655E-05	3.600E-06
130.4	75.0	0.19	1.82	1.006E-04	1.550E-05
364.6	40.0	0.68	3.27	4.489E-04	1.660E-05
364.6	50.0	0.68	3.27	4.283E-05	1.690E-06
366.7	79.5	0.68	3.27	4.300E-07	3.610E-08
366.7	79.5	0.68	3.27	4.363E-07	2.840E-08
366.7	87.0	0.68	3.27	5.297E-08	5.810E-09
366.7	95.5	0.75	3.64	1.509E-09	5.700E-10
366.7	105.0	0.75	3.64	7.600E-10	4.250E-10

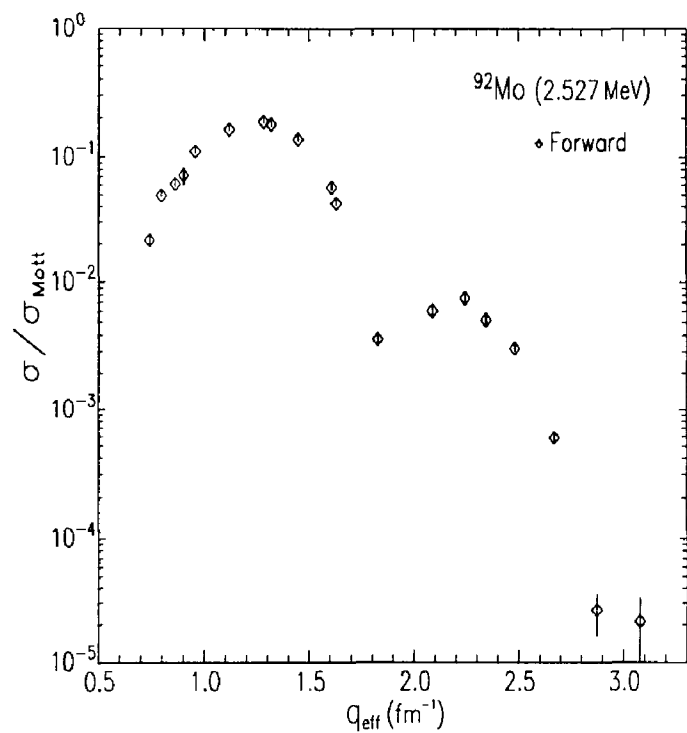


Figure B.4 Data for scattering in forward directions from state at 2.527 MeV.

Normalized Cross Sections for level at 2.612 MeV					
$E(\text{MeV})$	$\theta$ ( $^\circ$ )	$d\theta$ ( $^\circ$ )	$d\phi$ ( $^\circ$ )	$\sigma(\text{mb/sr})$	$d\sigma(\text{mb/sr})$
189.6	54.8	0.30	0.91	1.985E-05	1.310E-06
189.6	65.0	0.37	1.46	2.473E-05	1.020E-06
189.6	76.0	0.55	2.14	2.221E-05	7.010E-07
189.6	88.0	0.56	3.27	1.511E-05	4.070E-07
189.6	101.0	0.56	3.27	6.660E-06	2.520E-07
279.1	75.3	0.75	3.64	4.515E-06	2.130E-07
279.1	88.4	0.75	3.64	2.357E-07	2.300E-08
279.1	97.1	0.75	3.64	2.950E-08	9.160E-09
364.6	40.0	0.68	3.27	1.122E-04	4.790E-06
364.6	50.0	0.68	3.27	3.307E-05	1.340E-06
366.7	79.5	0.68	3.27	6.252E-08	1.270E-08
366.7	79.5	0.68	3.27	6.228E-08	9.310E-09
366.7	87.0	0.68	3.27	1.282E-08	2.750E-09
366.7	95.5	0.75	3.64	2.678E-09	7.640E-10
366.7	105.0	0.75	3.64	1.911E-12	1.910E-11

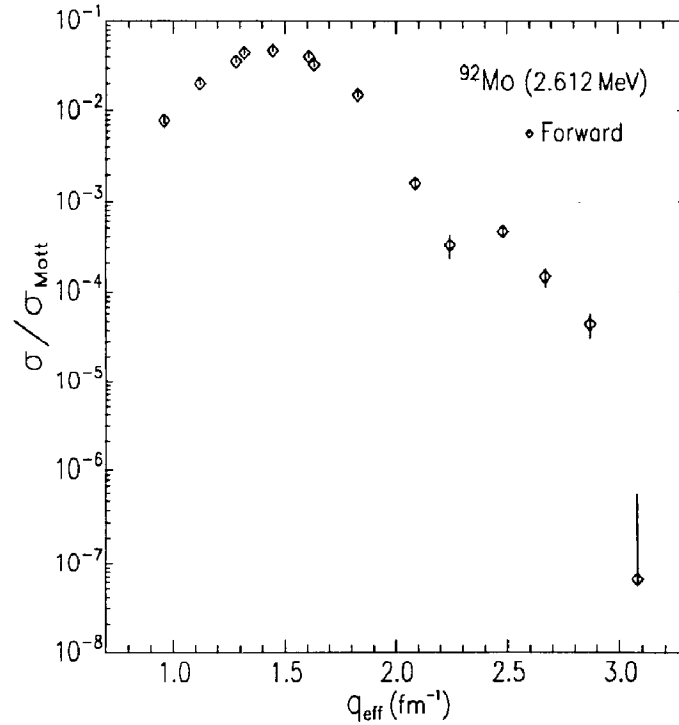


Figure B.5 Data for scattering in forward directions from state at 2.612 MeV.

Normalised Cross Sections for level at 2.760 MeV					
$E(\text{MeV})$	$\theta$ ( $^\circ$ )	$d\theta$ ( $^\circ$ )	$d\phi$ ( $^\circ$ )	$\sigma(\text{mb/sr})$	$d\sigma(\text{mb/sr})$
189.6	54.8	0.30	0.91	$6.750E-08$	$7.750E-08$
189.6	65.0	0.37	1.46	$2.336E-06$	$2.780E-07$
189.6	76.0	0.55	2.14	$1.469E-06$	$1.420E-07$
189.6	88.0	0.56	3.27	$1.653E-06$	$9.580E-08$
189.6	101.0	0.56	3.27	$1.157E-06$	$9.210E-08$
279.1	75.3	0.75	3.64	$2.423E-06$	$1.270E-07$
279.1	88.4	0.75	3.64	$9.582E-07$	$5.710E-08$
279.1	97.1	0.75	3.64	$4.464E-07$	$3.960E-08$
365.1	74.7	0.75	3.64	$3.570E-07$	$4.850E-08$
364.6	40.0	0.68	3.27	$4.539E-06$	$5.740E-07$
364.6	50.0	0.68	3.27	$7.728E-06$	$4.270E-07$
366.7	79.5	0.68	3.27	$1.896E-07$	$2.280E-08$
366.7	79.5	0.68	3.27	$1.818E-07$	$1.680E-08$
366.7	87.0	0.68	3.27	$1.648E-08$	$3.130E-09$
366.7	95.5	0.75	3.64	$9.799E-10$	$4.600E-10$
366.7	105.0	0.75	3.64	$1.440E-10$	$1.850E-10$

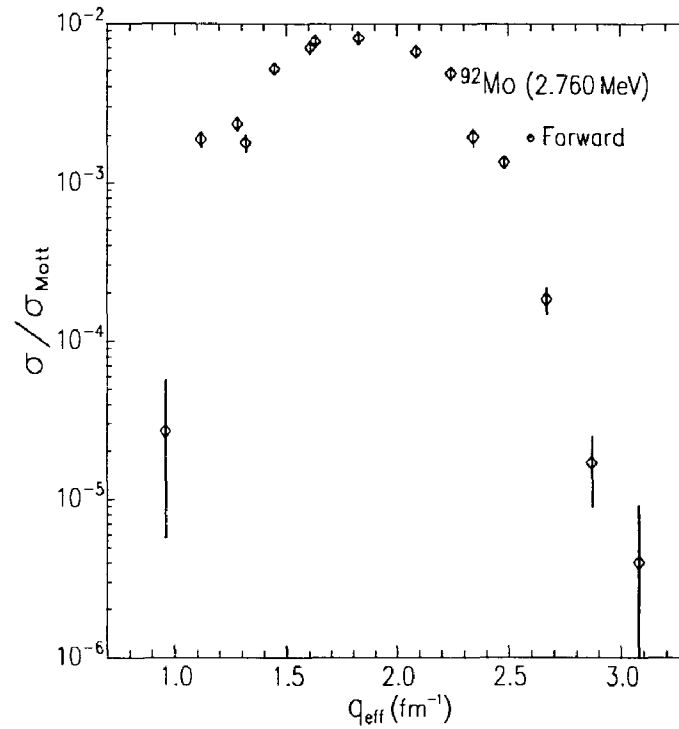


Figure B.6 Data for scattering in forward directions from state at 2.760 MeV.

Normalized Cross Sections for level at 2.850 MeV					
$E(\text{MeV})$	$\theta$ ( $^\circ$ )	$d\theta$ ( $^\circ$ )	$d\phi$ ( $^\circ$ )	$\sigma(\text{mb/sr})$	$d\sigma(\text{mb/sr})$
189.6	45.0	0.26	0.55	8.516E-03	1.740E-04
189.6	54.8	0.30	0.91	3.567E-03	7.330E-05
189.6	65.0	0.37	1.46	8.341E-04	1.750E-05
189.6	76.0	0.55	2.14	8.603E-05	2.020E-06
189.6	88.0	0.56	3.27	1.049E-05	3.090E-07
189.6	101.0	0.56	3.27	1.510E-05	4.420E-07
279.1	75.3	0.75	3.64	1.638E-05	6.890E-07
279.1	88.4	0.75	3.64	4.354E-07	3.340E-08
279.1	97.1	0.75	3.64	3.175E-07	3.250E-08
365.1	74.7	0.75	3.64	9.573E-07	8.280E-08
104.5	40.0	0.60	0.20	5.567E-03	2.560E-04
104.5	90.0	0.75	3.27	1.635E-03	5.850E-05
104.5	60.0	0.68	0.22	5.136E-03	2.940E-04
104.5	60.0	0.56	2.55	4.612E-03	1.700E-04
104.5	75.0	0.68	0.36	2.858E-03	1.480E-04
104.5	75.0	0.60	2.91	2.740E-03	9.900E-05
130.4	75.0	0.19	1.82	2.247E-03	1.070E-04
364.6	40.0	0.68	3.27	2.106E-04	8.270E-06
364.6	50.0	0.68	3.27	8.862E-05	3.300E-06
366.7	79.5	0.68	3.27	5.608E-07	4.240E-08
366.7	79.5	0.68	3.27	6.248E-07	3.620E-08
366.7	87.0	0.68	3.27	1.051E-07	8.610E-09
366.7	95.5	0.75	3.64	5.587E-09	1.110E-09
366.7	105.0	0.75	3.64	9.051E-10	4.660E-10

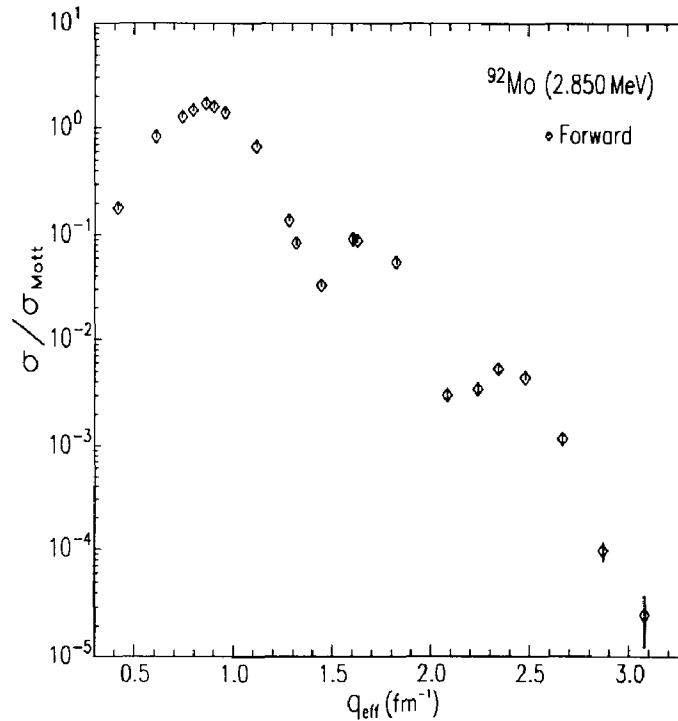


Figure B.7 Data for scattering in forward directions from state at 2.850 MeV.

Normalized Cross Sections for level at 3.096 MeV					
$E(\text{MeV})$	$\theta$ ( $^\circ$ )	$d\theta$ ( $^\circ$ )	$d\phi$ ( $^\circ$ )	$\sigma(\text{mb/sr})$	$d\sigma(\text{mb/sr})$
189.6	45.0	0.26	0.55	1.388E-03	3.160E-05
189.6	54.8	0.30	0.91	2.094E-04	5.850E-06
189.6	65.0	0.37	1.46	1.739E-05	8.260E-07
189.6	76.0	0.55	2.14	1.015E-05	4.200E-07
189.6	88.0	0.56	3.27	6.779E-06	2.280E-07
189.6	101.0	0.56	3.27	1.508E-06	1.060E-07
279.1	75.3	0.75	3.64	1.769E-07	2.340E-08
279.1	88.4	0.75	3.64	3.259E-07	2.800E-08
279.1	97.1	0.75	3.64	1.488E-07	2.140E-08
365.1	74.7	0.75	3.64	1.369E-07	2.970E-08
104.5	40.0	0.60	0.20	4.415E-03	2.150E-04
104.5	90.0	0.75	3.27	1.967E-04	8.100E-06
104.5	60.0	0.68	0.22	2.135E-03	1.680E-04
104.5	60.0	0.56	2.55	2.062E-03	8.080E-05
104.5	75.0	0.68	0.36	7.778E-04	6.310E-05
104.5	75.0	0.60	2.91	6.803E-04	2.680E-05
130.4	75.0	0.19	1.82	2.714E-04	2.680E-05
364.6	40.0	0.68	3.27	4.623E-05	2.400E-06
364.6	50.0	0.68	3.27	5.495E-06	3.390E-07
366.7	79.5	0.68	3.27	2.878E-08	8.590E-09
366.7	79.5	0.68	3.27	2.693E-08	6.070E-09
366.7	87.0	0.68	3.27	1.012E-08	2.450E-09
366.7	95.5	0.75	3.64	7.542E-10	4.050E-10
366.7	105.0	0.75	3.64	4.876E-10	3.430E-10

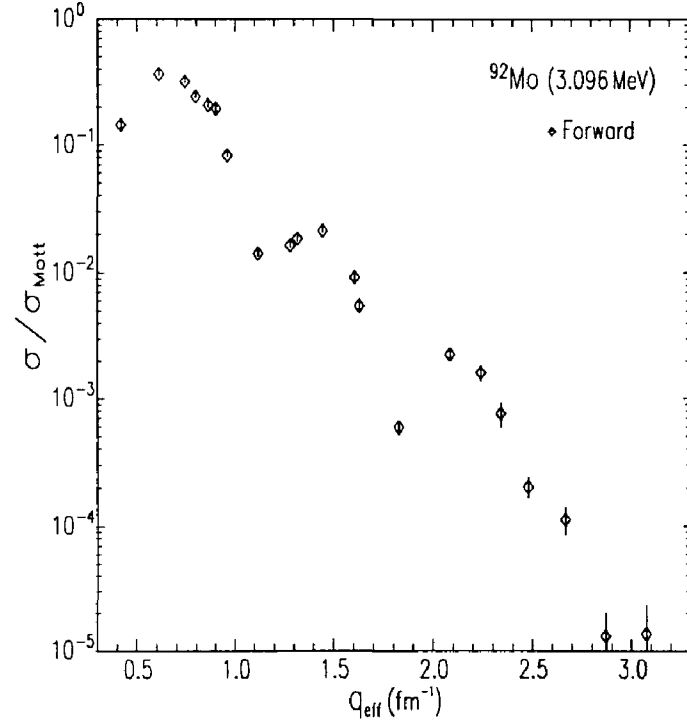


Figure B.8 Data for scattering in forward directions from state at 3.096 MeV.

Normalized Cross Sections for level at 3.369 MeV					
$E(\text{MeV})$	$\theta$ ( $^\circ$ )	$d\theta$ ( $^\circ$ )	$d\phi$ ( $^\circ$ )	$\sigma(\text{mb/sr})$	$d\sigma(\text{mb/sr})$
189.6	45.0	0.26	0.55	$2.428E-05$	$2.060E-06$
189.6	54.8	0.30	0.91	$1.451E-05$	$1.120E-06$
189.6	65.0	0.37	1.46	$4.462E-06$	$3.910E-07$
189.6	76.0	0.55	2.14	$7.404E-07$	$1.010E-07$
189.6	88.0	0.56	3.27	$9.248E-08$	$2.140E-08$
189.6	101.0	0.56	3.27	$8.916E-09$	$8.240E-09$
279.1	75.3	0.75	3.64	$9.543E-08$	$1.690E-08$
279.1	88.4	0.75	3.64	$1.409E-08$	$5.200E-09$
279.1	97.1	0.75	3.64	$2.193E-10$	$7.810E-10$
365.1	74.7	0.75	3.64	$1.786E-08$	$1.070E-08$
364.6	40.0	0.68	3.27	$1.799E-07$	$1.140E-07$
364.6	50.0	0.68	3.27	$1.813E-07$	$5.150E-08$

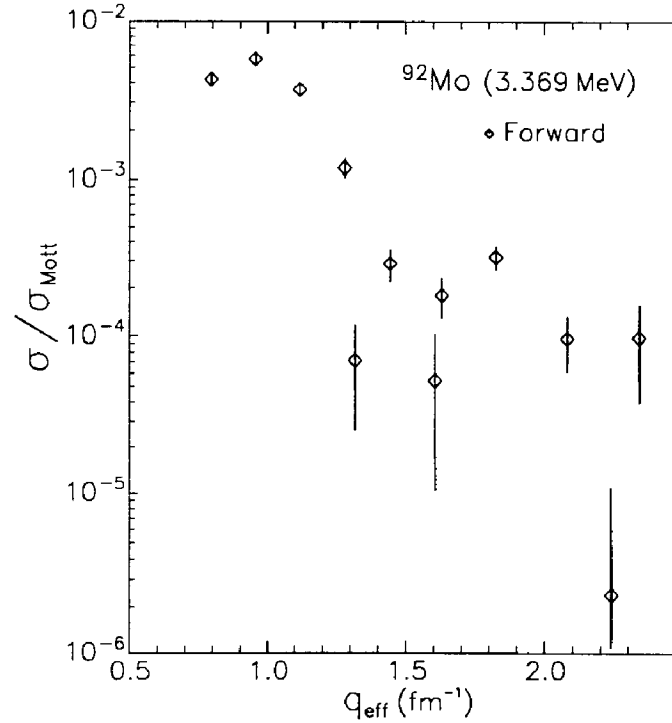


Figure B.9 Data for scattering in forward directions from state at 3.369 MeV.

Normalized Cross Sections for level at 3.545 MeV					
$E(\text{MeV})$	$\theta$ ( $^\circ$ )	$d\theta$ ( $^\circ$ )	$d\phi$ ( $^\circ$ )	$\sigma(\text{mb}/\text{sr})$	$d\sigma(\text{mb}/\text{sr})$
189.6	45.0	0.26	0.55	$5.780E-05$	$3.310E-06$
189.6	54.8	0.30	0.91	$1.527E-05$	$1.150E-06$
189.6	65.0	0.37	1.46	$1.440E-06$	$2.180E-07$
189.6	76.0	0.55	2.14	$1.276E-06$	$1.330E-07$
189.6	88.0	0.56	3.27	$4.759E-07$	$4.960E-08$
189.6	101.0	0.56	3.27	$2.509E-08$	$1.350E-08$
279.1	75.3	0.75	3.64	$1.493E-08$	$6.550E-09$
279.1	88.4	0.75	3.64	$5.980E-08$	$1.090E-08$
279.1	97.1	0.75	3.64	$1.727E-08$	$7.070E-09$
365.1	74.7	0.75	3.64	$6.581E-08$	$2.060E-08$
104.5	90.0	0.75	3.27	$1.152E-05$	$1.120E-06$
104.5	60.0	0.56	2.55	$1.480E-04$	$1.110E-05$
104.5	75.0	0.60	2.91	$4.921E-05$	$3.750E-06$
130.4	75.0	0.19	1.82	$1.559E-05$	$6.060E-06$
364.6	40.0	0.68	3.27	$3.033E-06$	$4.670E-07$
364.6	50.0	0.68	3.27	$1.192E-07$	$4.180E-08$
366.7	79.5	0.68	3.27	$8.834E-09$	$4.770E-09$
366.7	79.5	0.68	3.27	$1.585E-08$	$4.660E-09$
366.7	87.0	0.68	3.27	$3.900E-09$	$1.520E-09$
366.7	105.0	0.75	3.64	$3.432E-12$	$2.870E-11$

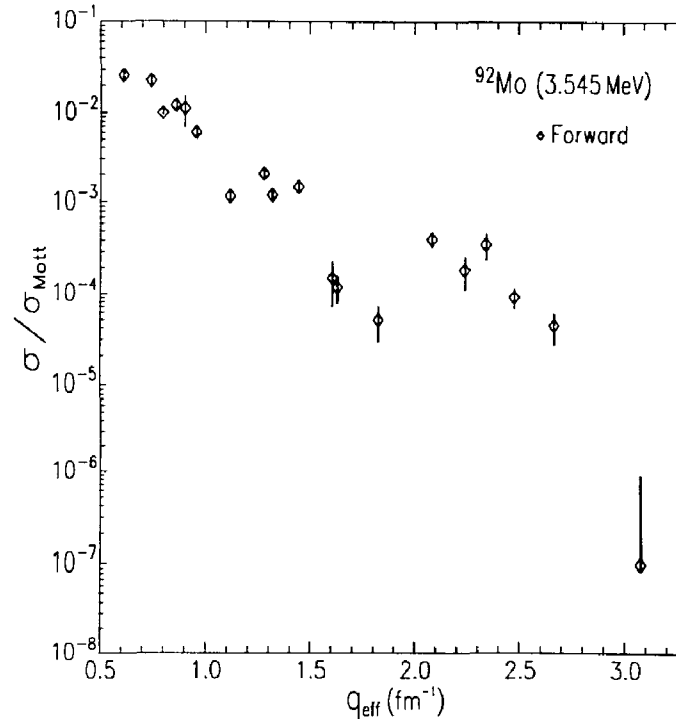


Figure B.10 Data for scattering in forward directions from state at 3.545 MeV.

Normalized Cross Sections for level at 3.583 MeV					
$E(\text{MeV})$	$\theta$ ( $^\circ$ )	$d\theta$ ( $^\circ$ )	$d\phi$ ( $^\circ$ )	$\sigma(\text{mb/sr})$	$d\sigma(\text{mb/sr})$
189.6	45.0	0.26	0.55	5.327E-04	1.420E-05
189.6	54.8	0.30	0.91	2.110E-04	5.890E-06
189.6	65.0	0.37	1.46	4.908E-05	1.600E-06
189.6	76.0	0.55	2.14	4.490E-06	2.620E-07
189.6	88.0	0.56	3.27	7.971E-07	6.500E-08
189.6	101.0	0.56	3.27	7.281E-07	7.300E-08
279.1	75.3	0.75	3.64	5.877E-07	4.720E-08
279.1	88.4	0.75	3.64	1.629E-08	5.610E-09
279.1	97.1	0.75	3.64	5.968E-08	1.330E-08
365.1	74.7	0.75	3.64	1.792E-07	3.430E-08
104.5	90.0	0.75	3.27	9.817E-05	4.590E-06
104.5	60.0	0.68	0.22	5.309E-04	7.770E-05
104.5	60.0	0.56	2.55	2.354E-04	1.480E-05
104.5	75.0	0.68	0.36	2.336E-04	3.250E-05
104.5	75.0	0.60	2.91	1.682E-04	8.530E-06
130.4	75.0	0.19	1.82	1.340E-04	1.830E-05
364.6	40.0	0.68	3.27	1.337E-05	1.060E-06
364.6	50.0	0.68	3.27	4.765E-06	3.110E-07
366.7	79.5	0.68	3.27	8.056E-08	1.470E-08
366.7	79.5	0.68	3.27	6.054E-08	9.300E-09
366.7	87.0	0.68	3.27	6.017E-09	1.900E-09
366.7	105.0	0.75	3.64	6.815E-10	4.080E-10

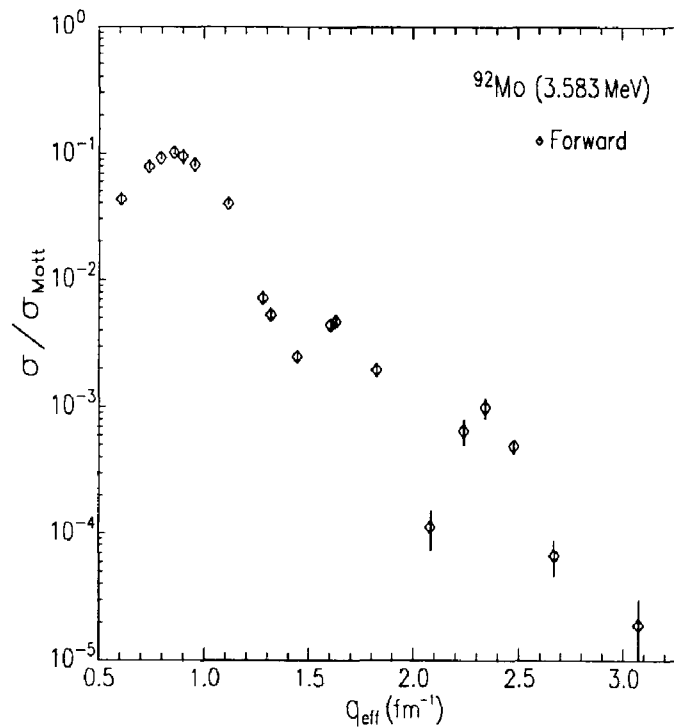


Figure B.11 Data for scattering in forward directions from state at 3.583 MeV.



Normalized Cross Sections for level at 3.626 MeV					
$E(\text{MeV})$	$\theta$ ( $^\circ$ )	$d\theta$ ( $^\circ$ )	$d\phi$ ( $^\circ$ )	$\sigma(\text{mb/sr})$	$d\sigma(\text{mb/sr})$
189.6	88.0	0.56	3.27	$3.282E-07$	$4.100E-08$
279.1	75.3	0.75	3.64	$3.555E-07$	$3.480E-08$
279.1	88.4	0.75	3.64	$1.043E-07$	$1.470E-08$
279.1	97.1	0.75	3.64	$1.805E-08$	$7.240E-09$
365.1	74.7	0.75	3.64	$2.474E-08$	$1.260E-08$
364.6	50.0	0.68	3.27	$1.029E-06$	$1.270E-07$
366.7	79.5	0.68	3.27	$2.177E-08$	$7.530E-09$
366.7	79.5	0.68	3.27	$3.096E-08$	$6.570E-09$
366.7	87.0	0.68	3.27	$6.197E-09$	$1.920E-09$
366.7	95.5	0.75	3.64	$1.266E-09$	$5.300E-10$
366.7	105.0	0.75	3.64	$3.062E-12$	$2.700E-11$

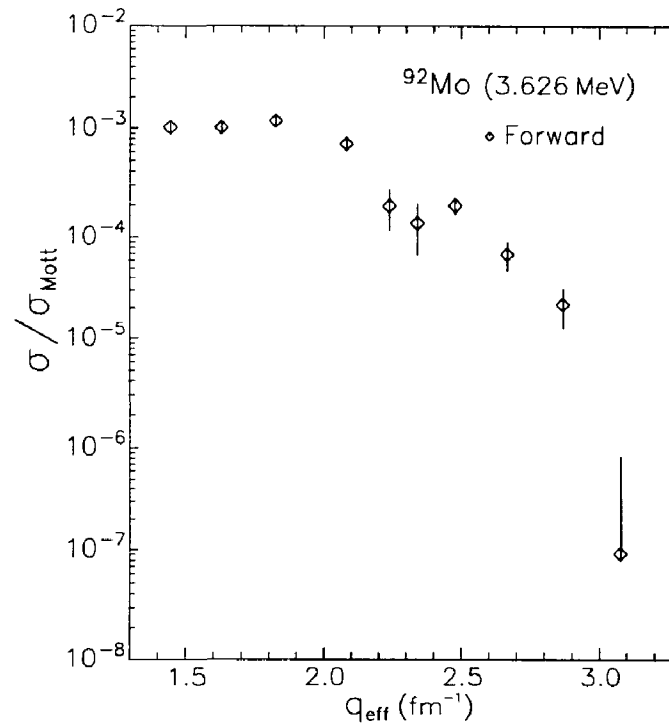


Figure B.12 Data for scattering in forward directions from state at 3.626 MeV.

Normalized Cross Sections for level at 3.879 MeV					
$E(\text{MeV})$	$\theta$ ( $^\circ$ )	$d\theta$ ( $^\circ$ )	$d\phi$ ( $^\circ$ )	$\sigma(\text{mb/sr})$	$d\sigma(\text{mb/sr})$
189.6	45.0	0.26	0.55	1.687E-04	6.290E-06
189.6	54.8	0.30	0.91	1.284E-04	4.130E-06
189.6	65.0	0.37	1.46	6.615E-05	1.980E-06
189.6	76.0	0.55	2.14	2.303E-05	7.250E-07
189.6	88.0	0.56	3.27	4.699E-06	1.810E-07
189.6	101.0	0.56	3.27	1.470E-07	3.250E-08
279.1	75.3	0.75	3.64	2.885E-07	3.100E-08
279.1	88.4	0.75	3.64	2.007E-07	2.120E-08
279.1	97.1	0.75	3.64	4.098E-08	1.100E-08
365.1	74.7	0.75	3.64	1.360E-08	9.370E-09
104.5	90.0	0.75	3.27	3.940E-05	2.380E-06
104.5	60.0	0.68	0.22	2.465E-04	5.240E-05
104.5	60.0	0.56	2.55	9.996E-05	8.820E-06
104.5	75.0	0.68	0.36	7.048E-05	1.760E-05
104.5	75.0	0.60	2.91	3.349E-05	3.010E-06
130.4	75.0	0.19	1.82	9.537E-05	1.540E-05
364.6	40.0	0.68	3.27	7.943E-05	3.630E-06
364.6	50.0	0.68	3.27	1.263E-06	1.430E-07
366.7	79.5	0.68	3.27	2.622E-09	2.610E-09
366.7	79.5	0.68	3.27	1.218E-09	1.290E-09
366.7	87.0	0.68	3.27	7.466E-09	2.120E-09
366.7	105.0	0.75	3.64	3.163E-12	2.760E-11

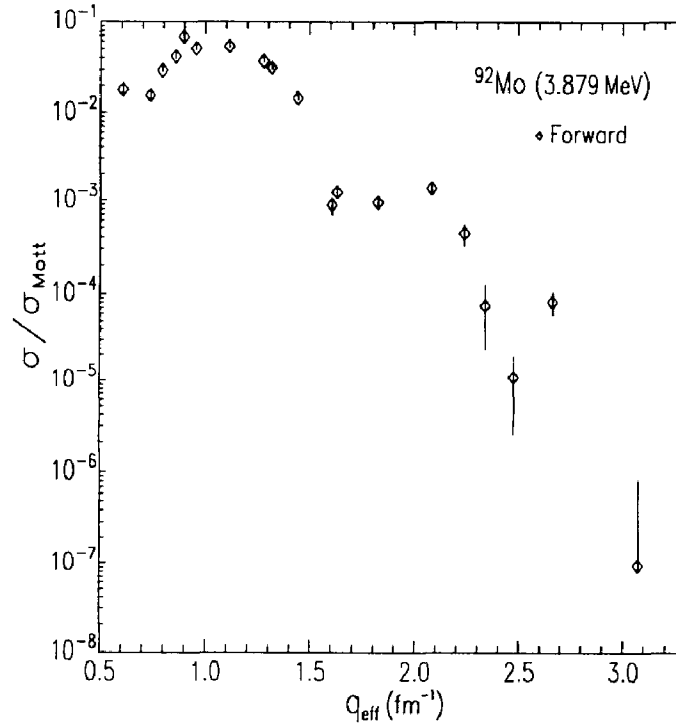


Figure B.13 Data for scattering in forward directions from state at 3.879 MeV.

Normalized Cross Sections for level at 3.929 MeV					
$E(\text{MeV})$	$\theta$ ( $^\circ$ )	$d\theta$ ( $^\circ$ )	$d\phi$ ( $^\circ$ )	$\sigma(\text{mb/sr})$	$d\sigma(\text{mb/sr})$
189.6	54.8	0.30	0.91	$8.343E-05$	$3.090E-06$
189.6	65.0	0.37	1.46	$1.146E-05$	$6.560E-07$
189.6	76.0	0.55	2.14	$1.258E-05$	$4.840E-07$
189.6	88.0	0.56	3.27	$5.249E-06$	$1.940E-07$
189.6	101.0	0.56	3.27	$6.605E-07$	$6.980E-08$
279.1	75.3	0.75	3.64	$5.582E-07$	$4.590E-08$
279.1	88.4	0.75	3.64	$3.848E-07$	$3.130E-08$
279.1	97.1	0.75	3.64	$1.121E-07$	$1.860E-08$
365.1	74.7	0.75	3.64	$1.192E-07$	$2.800E-08$
104.5	90.0	0.75	3.27	$8.290E-05$	$4.040E-06$
104.5	60.0	0.68	0.22	$1.322E-03$	$1.280E-04$
104.5	60.0	0.56	2.55	$1.150E-03$	$4.870E-05$
104.5	75.0	0.68	0.36	$3.643E-04$	$4.160E-05$
104.5	75.0	0.60	2.91	$3.198E-04$	$1.410E-05$
130.4	75.0	0.19	1.82	$1.548E-04$	$1.990E-05$
364.6	40.0	0.68	3.27	$4.748E-05$	$2.460E-06$
364.6	50.0	0.68	3.27	$2.658E-06$	$2.180E-07$
366.7	79.5	0.68	3.27	$3.302E-08$	$9.340E-09$
366.7	79.5	0.68	3.27	$2.907E-08$	$6.400E-09$
366.7	87.0	0.68	3.27	$8.387E-09$	$2.260E-09$
366.7	105.0	0.75	3.64	$7.291E-10$	$4.260E-10$

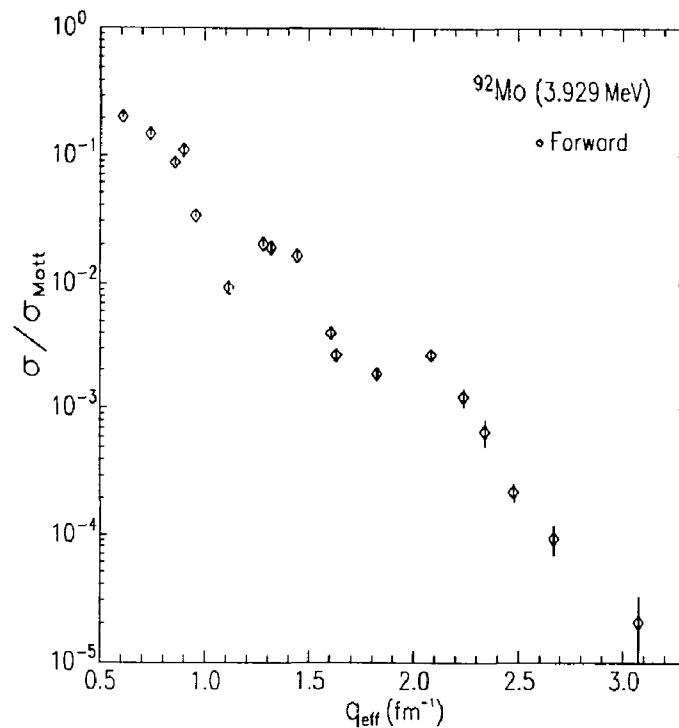


Figure B.13 Data for scattering in forward directions from state at 3.929 MeV.

Normalized Cross Sections for level at 4.159 MeV					
$E(\text{MeV})$	$\theta$ ( $^\circ$ )	$d\theta$ ( $^\circ$ )	$d\phi$ ( $^\circ$ )	$\sigma(\text{mb/sr})$	$d\sigma(\text{mb/sr})$
189.6	45.0	0.26	0.55	1.588E-04	6.070E-06
189.6	54.8	0.30	0.91	1.267E-04	4.100E-06
189.6	65.0	0.37	1.46	8.376E-05	2.360E-06
189.6	76.0	0.55	2.14	4.084E-05	1.110E-06
189.6	88.0	0.56	3.27	1.595E-05	4.280E-07
189.6	101.0	0.56	3.27	4.762E-06	2.080E-07
279.1	75.3	0.75	3.64	2.288E-06	1.230E-07
279.1	88.4	0.75	3.64	3.940E-07	3.190E-08
279.1	97.1	0.75	3.64	1.779E-07	2.390E-08
365.1	74.7	0.75	3.64	2.715E-07	4.280E-08
104.5	90.0	0.75	3.27	3.027E-05	2.010E-06
104.5	75.0	0.60	2.91	2.129E-05	2.340E-06
130.4	75.0	0.19	1.82	7.334E-05	1.350E-05
364.6	40.0	0.68	3.27	1.641E-04	6.670E-06
364.6	50.0	0.68	3.27	2.270E-05	9.830E-07
366.7	79.5	0.68	3.27	1.743E-07	2.230E-08
366.7	79.5	0.68	3.27	1.277E-07	1.400E-08
366.7	87.0	0.68	3.27	2.154E-08	3.690E-09
366.7	95.5	0.75	3.64	1.687E-09	6.200E-10
366.7	105.0	0.75	3.64	9.018E-10	4.790E-10

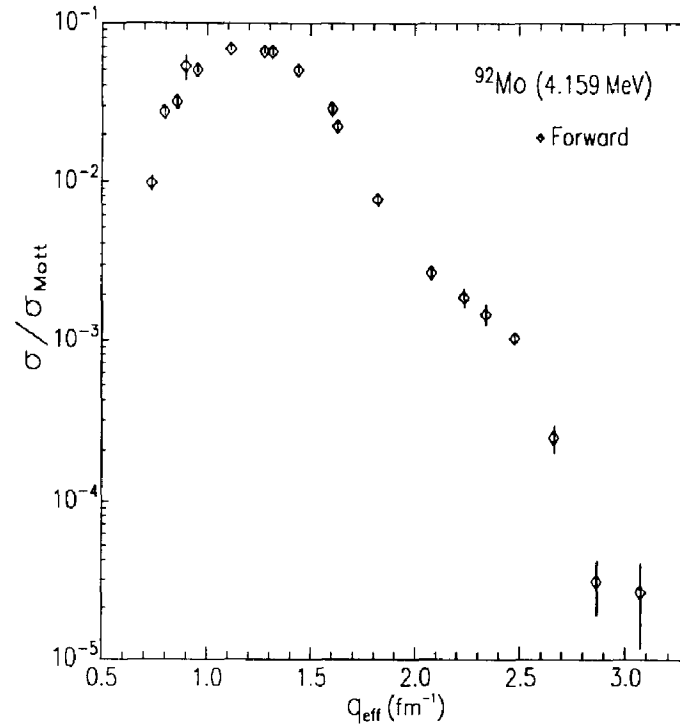


Figure B.14 Data for scattering in forward directions from state at 4.159 MeV.

Normalized Cross Sections for level at 4.312 MeV					
$E(\text{MeV})$	$\theta$ ( $^\circ$ )	$d\theta$ ( $^\circ$ )	$d\phi$ ( $^\circ$ )	$\sigma(\text{mb/sr})$	$d\sigma(\text{mb/sr})$
189.6	45.0	0.26	0.55	$4.261E-05$	$2.820E-06$
189.6	54.8	0.30	0.91	$3.483E-05$	$1.830E-06$
189.6	65.0	0.37	1.46	$2.766E-05$	$1.110E-06$
189.6	76.0	0.55	2.14	$1.740E-05$	$6.020E-07$
189.6	88.0	0.56	3.27	$7.909E-06$	$2.560E-07$
189.6	101.0	0.56	3.27	$2.374E-06$	$1.390E-07$
279.1	75.3	0.75	3.64	$1.005E-06$	$6.750E-08$
279.1	88.4	0.75	3.64	$2.534E-07$	$2.450E-08$
279.1	97.1	0.75	3.64	$1.433E-07$	$2.140E-08$
365.1	74.7	0.75	3.64	$1.691E-07$	$3.370E-08$
104.5	75.0	0.60	2.91	$4.502E-07$	$3.300E-07$
364.6	40.0	0.68	3.27	$7.688E-05$	$3.550E-06$
364.6	50.0	0.68	3.27	$1.185E-05$	$5.900E-07$
366.7	79.5	0.68	3.27	$8.727E-08$	$1.550E-08$
366.7	79.5	0.68	3.27	$8.244E-08$	$1.110E-08$
366.7	87.0	0.68	3.27	$1.105E-08$	$2.620E-09$
366.7	95.5	0.75	3.64	$1.167E-09$	$5.170E-10$
366.7	105.0	0.75	3.64	$7.313E-10$	$4.330E-10$

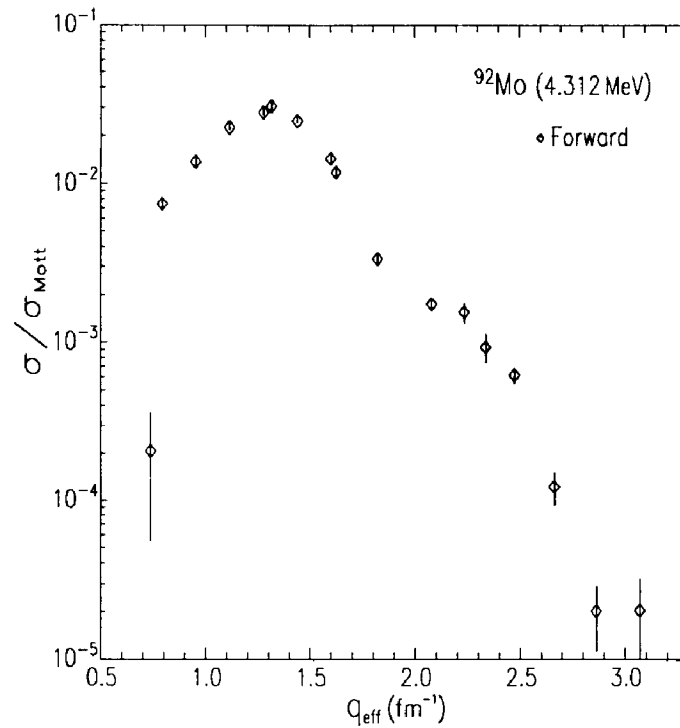


Figure B.15 Data for scattering in forward directions from state at 4.312 MeV.

Normalized Cross Sections for level at 4.495 MeV					
$E(\text{MeV})$	$\theta$ ( $^\circ$ )	$d\theta$ ( $^\circ$ )	$d\phi$ ( $^\circ$ )	$\sigma(\text{mb/sr})$	$d\sigma(\text{mb/sr})$
189.6	45.0	0.26	0.55	$2.199E-04$	$7.570E-06$
189.6	54.8	0.30	0.91	$2.174E-05$	$1.410E-06$
189.6	65.0	0.37	1.46	$6.388E-06$	$4.820E-07$
189.6	76.0	0.55	2.14	$1.176E-05$	$4.690E-07$
189.6	88.0	0.56	3.27	$6.546E-06$	$2.260E-07$
189.6	101.0	0.56	3.27	$1.358E-06$	$1.030E-07$
279.1	75.3	0.75	3.64	$3.864E-07$	$3.720E-08$
279.1	88.4	0.75	3.64	$3.634E-08$	$8.610E-09$
279.1	97.1	0.75	3.64	$5.089E-08$	$1.250E-08$
365.1	74.7	0.75	3.64	$4.870E-08$	$1.800E-08$
104.5	90.0	0.75	3.27	$3.437E-05$	$2.190E-06$
104.5	60.0	0.68	0.22	$3.370E-04$	$6.270E-05$
104.5	60.0	0.56	2.55	$4.286E-04$	$2.260E-05$
104.5	75.0	0.68	0.36	$8.444E-05$	$1.960E-05$
104.5	75.0	0.60	2.91	$1.055E-04$	$6.190E-06$
364.6	40.0	0.68	3.27	$5.235E-05$	$2.660E-06$
364.6	50.0	0.68	3.27	$7.351E-06$	$4.200E-07$
366.7	79.5	0.68	3.27	$3.568E-08$	$9.870E-09$
366.7	79.5	0.68	3.27	$3.541E-08$	$7.190E-09$
366.7	87.0	0.68	3.27	$1.047E-08$	$2.570E-09$
366.7	105.0	0.75	3.64	$7.516E-10$	$4.410E-10$

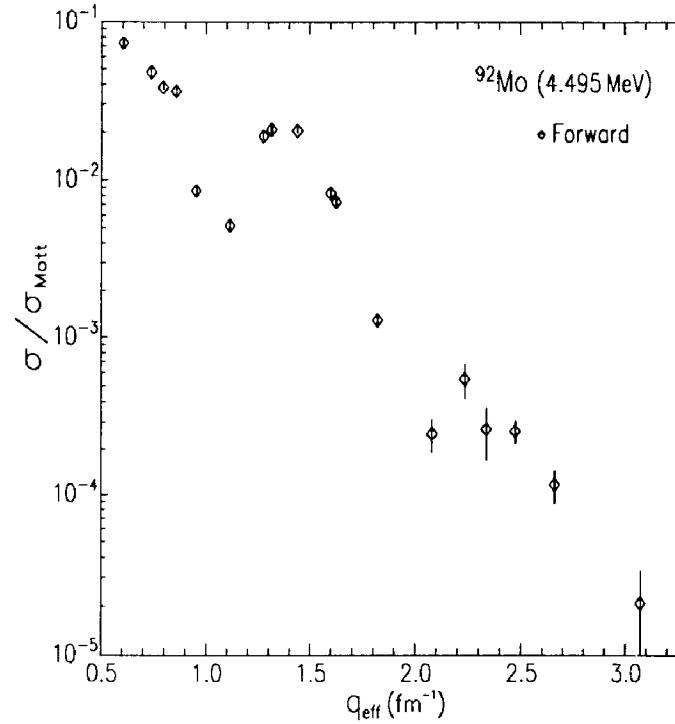


Figure B.16 Data for scattering in forward directions from state at 4.495 MeV.

Normalised Cross Sections for level at 4.555 MeV					
$E(\text{MeV})$	$\theta$ ( $^\circ$ )	$d\theta$ ( $^\circ$ )	$d\phi$ ( $^\circ$ )	$\sigma(\text{mb/sr})$	$d\sigma(\text{mb/sr})$
189.6	45.0	0.26	0.55	1.642E-05	1.710E-06
189.6	54.8	0.30	0.91	8.971E-06	8.840E-07
189.6	65.0	0.37	1.46	7.202E-06	5.150E-07
189.6	76.0	0.55	2.14	8.456E-06	3.840E-07
189.6	88.0	0.56	3.27	8.835E-06	2.780E-07
189.6	101.0	0.56	3.27	6.923E-06	2.640E-07
279.1	75.3	0.75	3.64	9.859E-06	4.300E-07
279.1	88.4	0.75	3.64	4.171E-06	1.900E-07
279.1	97.1	0.75	3.64	1.445E-06	8.760E-08
365.1	74.7	0.75	3.64	1.973E-06	1.290E-07
364.6	40.0	0.68	3.27	4.451E-05	2.360E-06
364.6	50.0	0.68	3.27	3.343E-05	1.370E-06
366.7	79.5	0.68	3.27	6.199E-07	4.630E-08
366.7	79.5	0.68	3.27	6.113E-07	3.640E-08
366.7	87.0	0.68	3.27	6.473E-08	6.720E-09
366.7	95.5	0.75	3.64	6.894E-09	1.290E-09
366.7	105.0	0.75	3.64	7.653E-10	4.500E-10

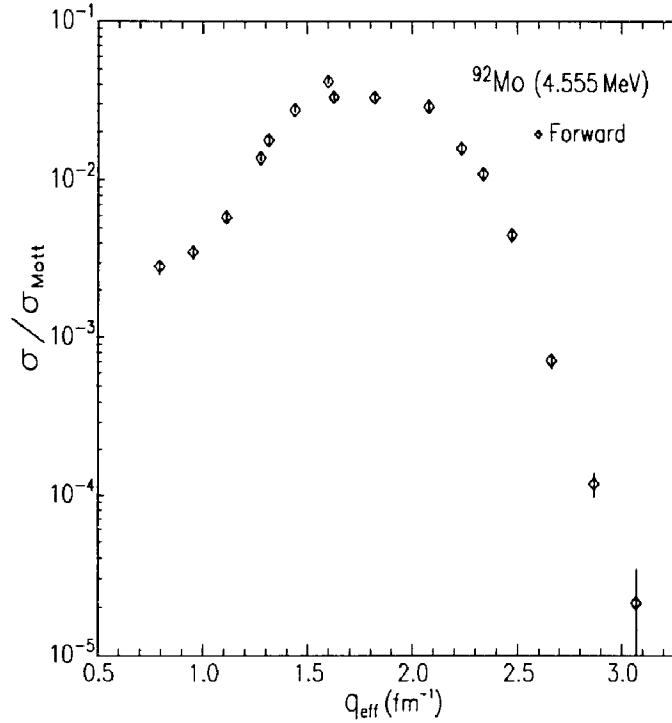


Figure B.17 Data for scattering in forward directions from state at 4.555 MeV.

Normalized Cross Sections for level at 4.598 MeV					
$E(\text{MeV})$	$\theta$ ( $^\circ$ )	$d\theta$ ( $^\circ$ )	$d\phi$ ( $^\circ$ )	$\sigma(\text{mb/sr})$	$d\sigma(\text{mb/sr})$
189.6	45.0	0.26	0.55	$1.329E-04$	$5.480E-06$
189.6	54.8	0.30	0.91	$5.156E-05$	$2.320E-06$
189.6	65.0	0.37	1.46	$2.066E-05$	$9.350E-07$
189.6	76.0	0.55	2.14	$1.427E-05$	$5.310E-07$
189.6	88.0	0.56	3.27	$8.229E-06$	$2.650E-07$
189.6	101.0	0.56	3.27	$3.003E-06$	$1.600E-07$
279.1	75.3	0.75	3.64	$2.935E-06$	$1.500E-07$
279.1	88.4	0.75	3.64	$2.721E-07$	$2.570E-08$
279.1	97.1	0.75	3.64	$3.701E-08$	$1.070E-08$
365.1	74.7	0.75	3.64	$4.371E-09$	$5.400E-09$
104.5	90.0	0.75	3.27	$2.095E-05$	$1.610E-06$
104.5	75.0	0.60	2.91	$3.887E-05$	$3.320E-06$
130.4	75.0	0.19	1.82	$6.669E-05$	$1.300E-05$
364.6	40.0	0.68	3.27	$6.485E-05$	$3.130E-06$
364.6	50.0	0.68	3.27	$1.755E-05$	$8.020E-07$
366.7	79.5	0.68	3.27	$2.833E-08$	$8.810E-09$
366.7	79.5	0.68	3.27	$3.939E-08$	$7.620E-09$
366.7	87.0	0.68	3.27	$2.094E-09$	$1.140E-09$
366.7	105.0	0.75	3.64	$7.264E-10$	$4.370E-10$

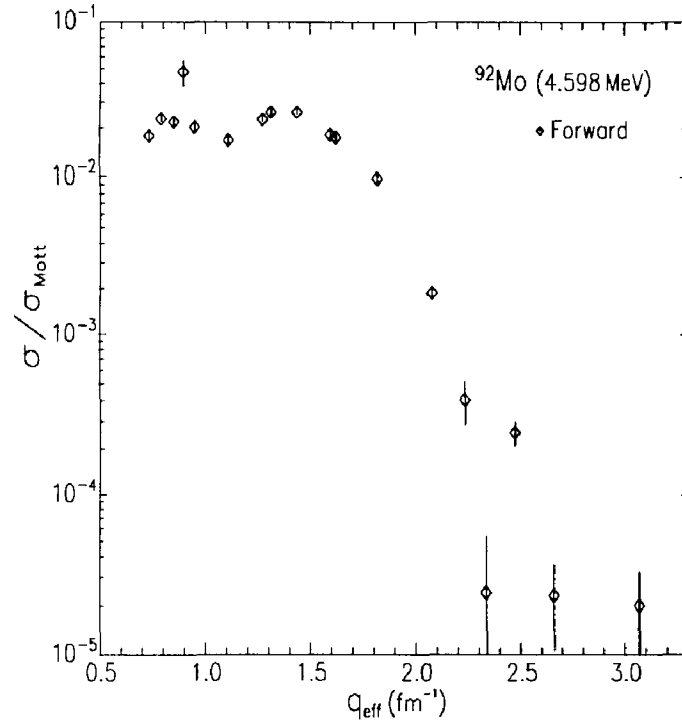


Figure B.18 Data for scattering in forward directions from state at 4.598 MeV.



Normalised Cross Sections for level at 4.634 MeV					
$E(\text{MeV})$	$\theta$ ( $^\circ$ )	$d\theta$ ( $^\circ$ )	$d\phi$ ( $^\circ$ )	$\sigma(\text{mb/sr})$	$d\sigma(\text{mb/sr})$
189.6	45.0	0.26	0.55	$4.121E-05$	$2.790E-06$
189.6	54.8	0.30	0.91	$1.144E-05$	$1.010E-06$
189.6	65.0	0.37	1.46	$8.544E-06$	$5.660E-07$
189.6	76.0	0.55	2.14	$3.614E-06$	$2.370E-07$
189.6	88.0	0.56	3.27	$1.357E-06$	$8.850E-08$
189.6	101.0	0.56	3.27	$4.639E-07$	$5.920E-08$
279.1	75.3	0.75	3.64	$3.590E-07$	$3.570E-08$
279.1	88.4	0.75	3.64	$4.541E-08$	$9.700E-09$
279.1	97.1	0.75	3.64	$8.891E-08$	$1.680E-08$
365.1	74.7	0.75	3.64	$8.408E-08$	$2.380E-08$
104.5	90.0	0.75	3.27	$4.548E-06$	$6.870E-07$
364.6	40.0	0.68	3.27	$1.928E-05$	$1.350E-06$
364.6	50.0	0.68	3.27	$1.100E-06$	$1.350E-07$
366.7	79.5	0.68	3.27	$2.378E-08$	$8.080E-09$
366.7	79.5	0.68	3.27	$1.724E-08$	$5.000E-09$
366.7	87.0	0.68	3.27	$7.364E-09$	$2.160E-09$
366.7	105.0	0.75	3.64	$6.821E-10$	$4.230E-10$

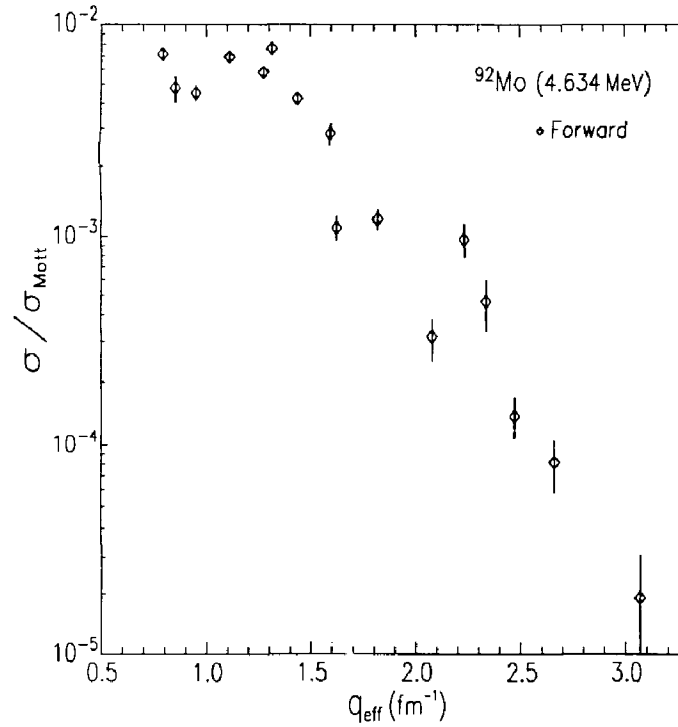


Figure B.19 Data for scattering in forward directions from state at 4.634 MeV.

Normalised Cross Sections for level at 4.724 MeV					
$E(\text{MeV})$	$\theta$ ( $^\circ$ )	$d\theta$ ( $^\circ$ )	$d\phi$ ( $^\circ$ )	$\sigma(\text{mb/sr})$	$d\sigma(\text{mb/sr})$
189.6	45.0	0.26	0.55	$1.431E-04$	$5.760E-06$
189.6	54.8	0.30	0.91	$9.031E-05$	$3.300E-06$
189.6	65.0	0.37	1.46	$3.880E-05$	$1.390E-06$
189.6	76.0	0.55	2.14	$1.167E-05$	$4.690E-07$
189.6	88.0	0.56	3.27	$2.011E-06$	$1.100E-07$
189.6	101.0	0.56	3.27	$3.458E-07$	$5.120E-08$
279.1	75.3	0.75	3.64	$1.119E-07$	$1.890E-08$
279.1	88.4	0.75	3.64	$1.865E-08$	$6.180E-09$
279.1	97.1	0.75	3.64	$9.351E-09$	$5.360E-09$
365.1	74.7	0.75	3.64	$4.402E-09$	$5.440E-09$
104.5	90.0	0.75	3.27	$3.396E-05$	$2.190E-06$
104.5	60.0	0.56	2.55	$7.373E-05$	$7.520E-06$
104.5	75.0	0.60	2.91	$3.871E-05$	$3.320E-06$
130.4	75.0	0.19	1.82	$4.433E-05$	$1.060E-05$
364.6	40.0	0.68	3.27	$3.941E-05$	$2.180E-06$
364.6	50.0	0.68	3.27	$1.441E-06$	$1.570E-07$
366.7	79.5	0.68	3.27	$2.384E-08$	$8.130E-09$
366.7	79.5	0.68	3.27	$2.239E-08$	$5.740E-09$
366.7	87.0	0.68	3.27	$9.645E-10$	$7.790E-10$
366.7	105.0	0.75	3.64	$3.668E-10$	$3.130E-10$

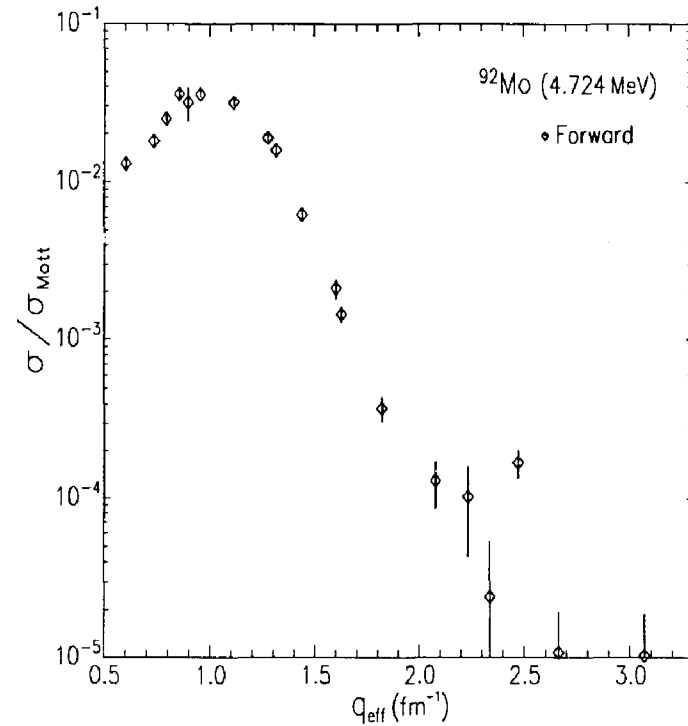


Figure B.18 Data for scattering in forward directions from state at 4.724 MeV.

Normalized Cross Sections for level at 5.090 MeV					
$E(\text{MeV})$	$\theta$ ( $^\circ$ )	$d\theta$ ( $^\circ$ )	$d\phi$ ( $^\circ$ )	$\sigma(\text{mb/sr})$	$d\sigma(\text{mb/sr})$
189.6	45.0	0.26	0.55	$5.805E-05$	$3.420E-06$
189.6	54.8	0.30	0.91	$1.596E-05$	$1.220E-06$
189.6	65.0	0.37	1.46	$1.935E-05$	$9.120E-07$
189.6	76.0	0.55	2.14	$1.223E-05$	$4.890E-07$
189.6	88.0	0.56	3.27	$2.438E-06$	$1.250E-07$
189.6	101.0	0.56	3.27	$9.174E-08$	$2.660E-08$
279.1	75.3	0.75	3.64	$5.540E-07$	$4.700E-08$
279.1	88.4	0.75	3.64	$1.735E-07$	$2.020E-08$
279.1	97.1	0.75	3.64	$4.468E-09$	$3.760E-09$
365.1	74.7	0.75	3.64	$4.292E-08$	$1.730E-08$
104.5	90.0	0.75	3.27	$7.642E-06$	$9.210E-07$
104.5	60.0	0.56	2.55	$1.226E-04$	$1.020E-05$
104.5	75.0	0.60	2.91	$2.895E-05$	$2.840E-06$
364.6	40.0	0.68	3.27	$3.849E-05$	$2.160E-06$
364.6	50.0	0.68	3.27	$6.997E-07$	$1.080E-07$
366.7	79.5	0.68	3.27	$2.223E-08$	$7.980E-09$
366.7	79.5	0.68	3.27	$4.098E-08$	$7.960E-09$
366.7	87.0	0.68	3.27	$1.633E-08$	$3.310E-09$
366.7	105.0	0.75	3.64	$5.940E-10$	$4.110E-10$

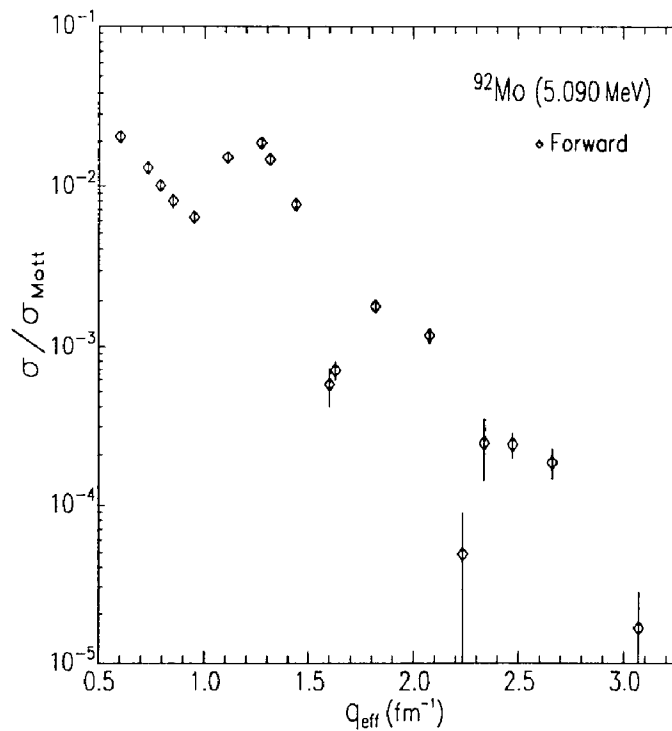


Figure B.22 Data for scattering in forward directions from state at 5.007 MeV.

Normalized Cross Sections for level at 5.090 MeV					
$E(\text{MeV})$	$\theta$ ( $^\circ$ )	$d\theta$ ( $^\circ$ )	$d\phi$ ( $^\circ$ )	$\sigma(\text{mb/sr})$	$d\sigma(\text{mb/sr})$
189.6	155.0	0.58	3.54	$7.613E-08$	$8.620E-09$
125.7	155.0	0.75	1.82	$6.131E-07$	$4.620E-08$
175.1	150.0	0.75	2.18	$3.522E-07$	$3.420E-08$
239.7	155.0	0.75	3.64	$7.794E-09$	$2.100E-09$
219.2	155.0	0.75	2.72	$3.232E-08$	$7.690E-09$
259.0	155.0	0.75	3.64	$5.588E-09$	$1.970E-09$
204.8	155.0	0.75	3.64	$2.476E-08$	$3.840E-09$
159.5	155.0	0.75	2.73	$1.811E-07$	$1.470E-08$
139.4	155.0	0.75	3.64	$3.175E-07$	$3.800E-08$
100.3	155.0	0.75	3.64	$2.211E-06$	$1.230E-07$

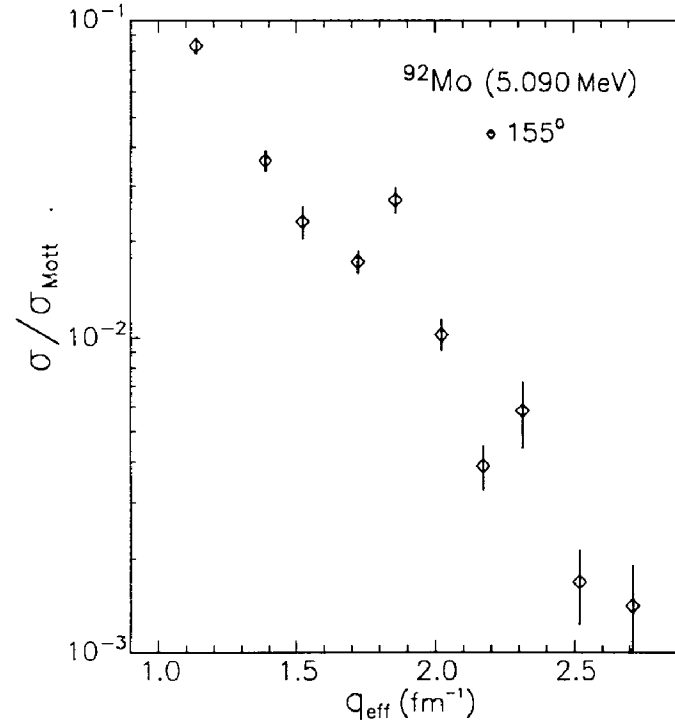


Figure B.23 Data for scattering in forward directions from state at 5.090 MeV.

Summary of Backward Scattering Data Analysis				
<i>N</i>	<i>E*</i> (MeV)	<i>J*</i>	Number of <i>q</i> -points	Data included in DWBA fit shown (yes/no)
1	1.509	2 <sup>+</sup>	12	no
2	2.282	4 <sup>+</sup>	13	no
3	2.527	5 <sup>-</sup>	13	yes
4	2.612	6 <sup>+</sup>	11	no
5	2.760	8 <sup>+</sup>	11	no
6	2.850	3 <sup>-</sup>	13	yes
7	3.096	2 <sup>+</sup>	5	no
8	3.583	3 <sup>-</sup>	6	yes
9	3.626	7 <sup>-</sup>	8	no
10	3.879	4 <sup>+</sup>	10	no
11	3.929	2 <sup>+</sup>	10	no
12	4.159	5 <sup>-</sup>	10	yes
13	4.312	5 <sup>-</sup>	10	yes
14	4.560	7 <sup>-†</sup>	10	yes
15	4.690	(6 <sup>-</sup> )†	10	yes
16	4.925	7 <sup>+</sup>	10	yes
17	5.090	4 <sup>+</sup>	10	yes

†Spin-parity assignment determined in this experiment.

Table B.2 Summary of backward scattering data analysis. The spin-parity assignment were taken from *Refs.* 48, 49 or 50 unless otherwise noted.

Normalized Cross Sections for level at 2.527 MeV					
$E(\text{MeV})$	$\theta$ ( $^\circ$ )	$d\theta$ ( $^\circ$ )	$d\phi$ ( $^\circ$ )	$\sigma(\text{mb/sr})$	$d\sigma(\text{mb/sr})$
189.6	155.0	0.58	3.54	$6.695E-08$	$7.590E-09$
125.7	155.0	0.75	1.82	$3.151E-06$	$1.720E-07$
175.1	150.0	0.75	2.18	$1.462E-07$	$1.920E-08$
239.7	155.0	0.75	3.64	$1.843E-08$	$3.140E-09$
219.2	155.0	0.75	2.72	$6.577E-08$	$1.070E-08$
259.0	155.0	0.75	3.64	$1.811E-09$	$1.050E-09$
204.8	155.0	0.75	3.64	$6.601E-08$	$6.470E-09$
159.5	155.0	0.75	2.73	$3.900E-07$	$2.530E-08$
139.4	155.0	0.75	3.64	$1.901E-06$	$1.960E-07$
290.4	155.0	0.75	2.91	$3.975E-12$	$2.640E-11$
80.4	160.0	0.75	3.64	$1.411E-06$	$1.570E-07$
100.3	155.0	0.75	3.64	$4.473E-06$	$2.640E-07$
100.3	155.0	0.75	3.64	$4.191E-06$	$2.210E-07$

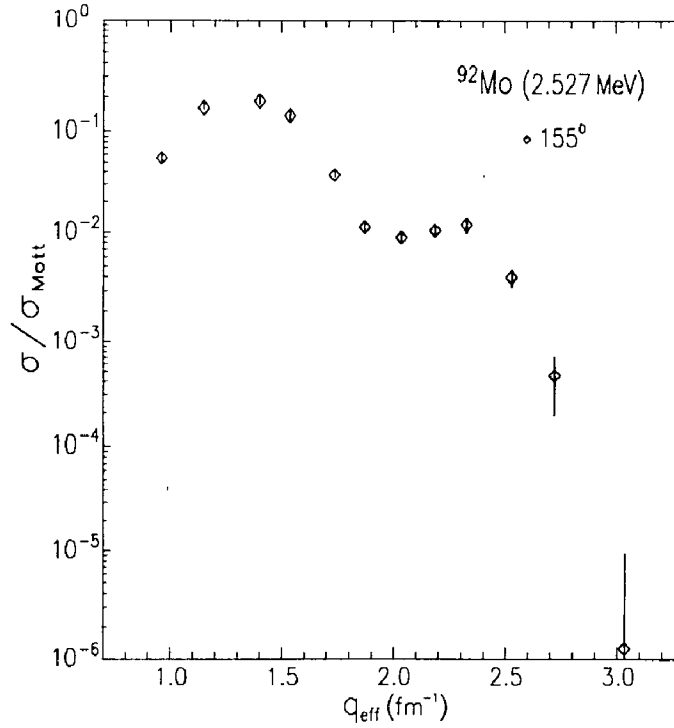


Figure B.24 Data for scattering at backward angles from state at 2.527 MeV.

Normalized Cross Sections for level at 2.850 MeV					
$E(\text{MeV})$	$\theta$ ( $^\circ$ )	$d\theta$ ( $^\circ$ )	$d\phi$ ( $^\circ$ )	$\sigma(\text{mb/sr})$	$d\sigma(\text{mb/sr})$
189.6	155.0	0.58	3.54	$1.240E-07$	$1.120E-08$
125.7	155.0	0.75	1.82	$7.962E-07$	$5.290E-08$
175.1	150.0	0.75	2.18	$8.613E-07$	$6.110E-08$
239.7	155.0	0.75	3.64	$2.498E-08$	$3.720E-09$
219.2	155.0	0.75	2.72	$5.738E-08$	$9.950E-09$
259.0	155.0	0.75	3.64	$4.213E-09$	$1.620E-09$
204.8	155.0	0.75	3.64	$5.740E-08$	$5.940E-09$
159.5	155.0	0.75	2.73	$9.937E-07$	$5.600E-08$
139.4	155.0	0.75	3.64	$1.236E-06$	$1.300E-07$
290.4	155.0	0.75	2.91	$7.951E-12$	$3.790E-11$
80.4	160.0	0.75	3.64	$3.886E-05$	$2.080E-06$
100.3	155.0	0.75	3.64	$1.628E-05$	$8.570E-07$
100.3	155.0	0.75	3.64	$1.692E-05$	$8.570E-07$

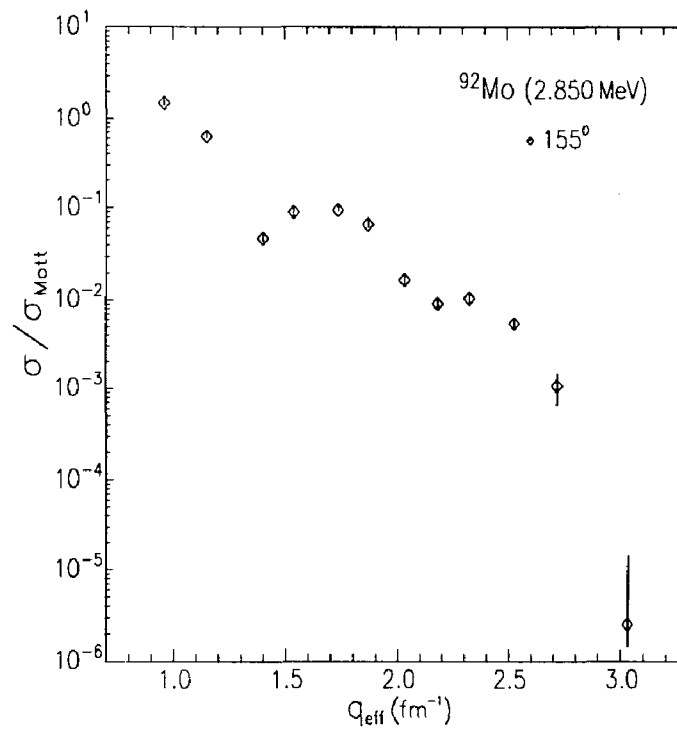


Figure B.25 Data for scattering at backward angles from state at 2.850 MeV.

Normalised Cross Sections for level at 4.159 MeV					
$E(\text{MeV})$	$\theta$ ( $^\circ$ )	$d\theta$ ( $^\circ$ )	$d\phi$ ( $^\circ$ )	$\sigma(\text{mb/sr})$	$d\sigma(\text{mb/sr})$
189.6	155.0	0.58	3.54	$1.429E-07$	$1.240E-08$
125.7	155.0	0.75	1.82	$1.194E-06$	$7.390E-08$
175.1	150.0	0.75	2.18	$4.508E-07$	$3.900E-08$
239.7	155.0	0.75	3.64	$1.077E-08$	$2.400E-09$
219.2	155.0	0.75	2.72	$5.084E-08$	$9.450E-09$
259.0	155.0	0.75	3.64	$1.004E-09$	$7.970E-10$
204.8	155.0	0.75	3.64	$8.290E-08$	$7.600E-09$
159.5	155.0	0.75	2.73	$4.078E-07$	$2.640E-08$
139.4	155.0	0.75	3.64	$8.769E-07$	$9.380E-08$
290.4	155.0	0.75	2.91	$8.543E-10$	$4.090E-10$
100.3	155.0	0.75	3.64	$1.786E-06$	$1.010E-07$

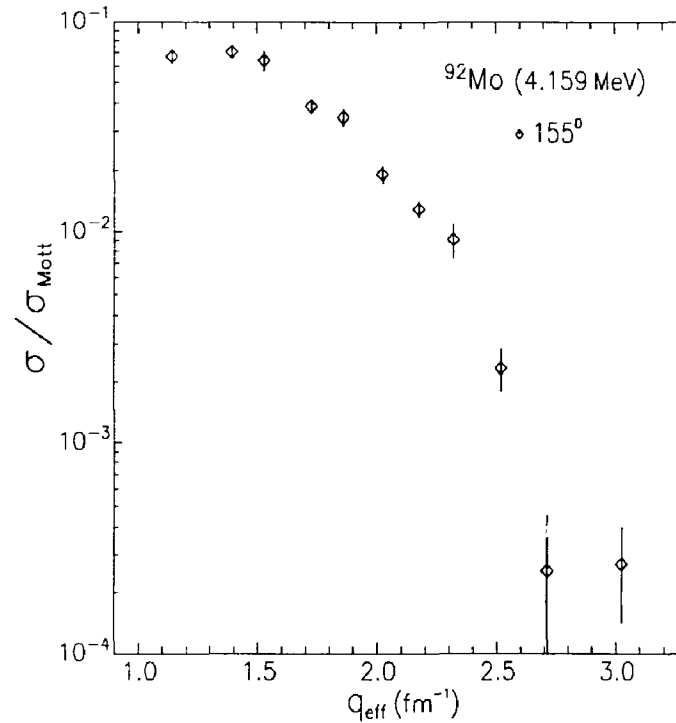


Figure B.26 Data for scattering at backward angles from state at 4.159 MeV.



Normalized Cross Sections for level at 4.312 MeV					
$E(\text{MeV})$	$\theta$ ( $^\circ$ )	$d\theta$ ( $^\circ$ )	$d\phi$ ( $^\circ$ )	$\sigma(\text{mb/sr})$	$d\sigma(\text{mb/sr})$
189.6	155.0	0.58	3.54	$1.096E-07$	$1.050E-08$
125.7	155.0	0.75	1.82	$2.075E-07$	$2.090E-08$
175.1	150.0	0.75	2.18	$2.316E-07$	$2.570E-08$
239.7	155.0	0.75	3.64	$4.301E-09$	$1.500E-09$
219.2	155.0	0.75	2.72	$1.930E-08$	$5.710E-09$
259.0	155.0	0.75	3.64	$2.912E-09$	$1.370E-09$
204.8	155.0	0.75	3.64	$4.327E-08$	$5.100E-09$
159.5	155.0	0.75	2.73	$3.067E-07$	$2.120E-08$
139.4	155.0	0.75	3.64	$1.496E-07$	$2.040E-08$
290.4	155.0	0.75	2.91	$6.678E-12$	$3.570E-11$
100.3	155.0	0.75	3.64	$7.082E-07$	$4.590E-08$

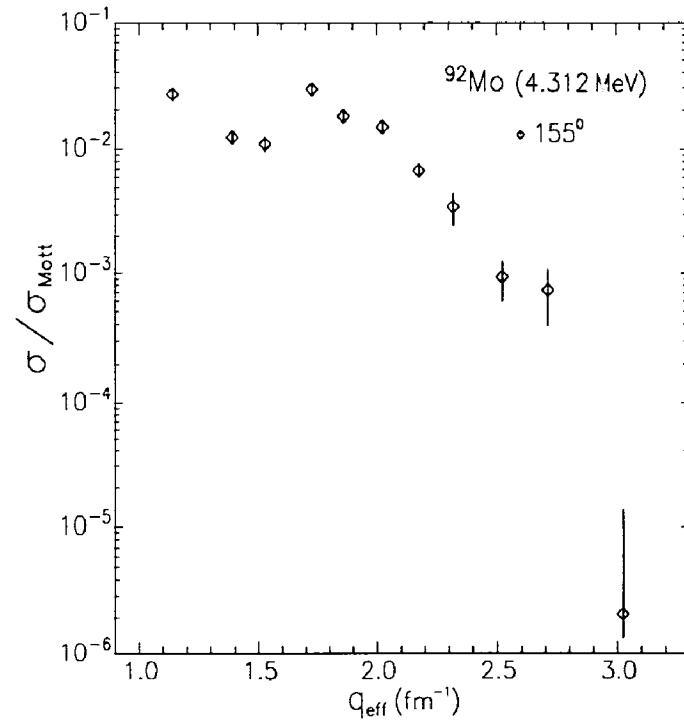


Figure B.27 Data for scattering at backward angles from state at 4.312 MeV.

Normalised Cross Sections for level at 4.555 MeV					
$E(\text{MeV})$	$\theta$ ( $^\circ$ )	$d\theta$ ( $^\circ$ )	$d\phi$ ( $^\circ$ )	$\sigma(\text{mb/sr})$	$d\sigma(\text{mb/sr})$
189.6	155.0	0.58	3.54	$6.806E-07$	$4.080E-08$
125.7	155.0	0.75	1.82	$4.906E-07$	$3.740E-08$
175.1	150.0	0.75	2.18	$1.043E-06$	$7.160E-08$
239.7	155.0	0.75	3.64	$1.402E-07$	$1.100E-08$
219.2	155.0	0.75	2.72	$2.828E-07$	$2.590E-08$
259.0	155.0	0.75	3.64	$1.317E-08$	$2.980E-09$
204.8	155.0	0.75	3.64	$4.958E-07$	$2.940E-08$
159.5	155.0	0.75	2.73	$1.012E-06$	$5.720E-08$
139.4	155.0	0.75	3.64	$6.567E-07$	$7.180E-08$
290.4	155.0	0.75	2.91	$1.489E-09$	$5.500E-10$
100.3	155.0	0.75	3.64	$1.241E-07$	$1.380E-08$

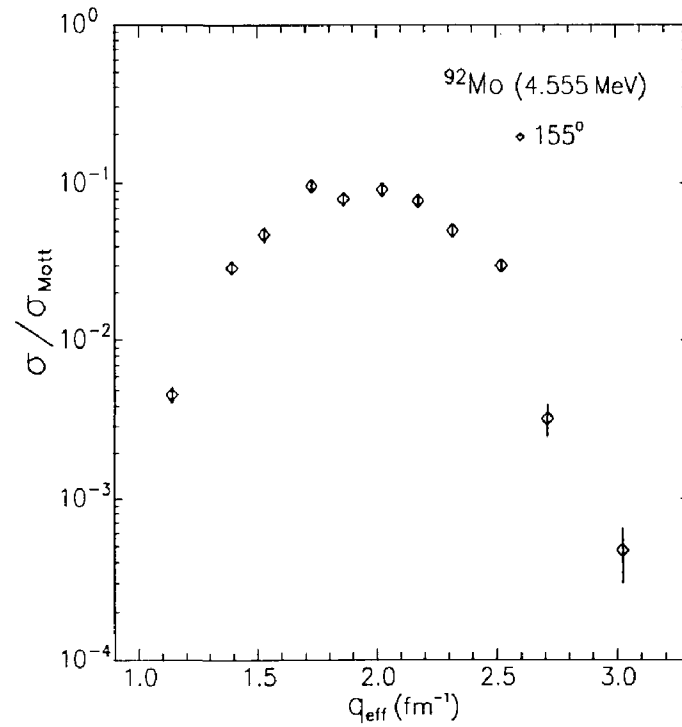


Figure B.28 Data for scattering at backward angles from state at 4.555 MeV.

Normalised Cross Sections for level at 4.690 MeV					
$E(\text{MeV})$	$\theta$ ( $^\circ$ )	$d\theta$ ( $^\circ$ )	$d\phi$ ( $^\circ$ )	$\sigma(\text{mb/sr})$	$d\sigma(\text{mb/sr})$
189.6	155.0	0.58	3.54	$1.723E-07$	$1.420E-08$
125.7	155.0	0.75	1.82	$5.649E-07$	$4.150E-08$
175.1	150.0	0.75	2.18	$1.211E-07$	$1.780E-08$
239.7	155.0	0.75	3.64	$5.777E-08$	$6.210E-09$
219.2	155.0	0.75	2.72	$1.591E-07$	$1.820E-08$
259.0	155.0	0.75	3.64	$9.910E-09$	$2.580E-09$
204.8	155.0	0.75	3.64	$2.072E-07$	$1.460E-08$
159.5	155.0	0.75	2.73	$1.459E-07$	$1.250E-08$
139.4	155.0	0.75	3.64	$3.172E-07$	$3.770E-08$
290.4	155.0	0.75	2.91	$6.680E-10$	$3.690E-10$
100.3	155.0	0.75	3.64	$2.323E-07$	$2.050E-08$

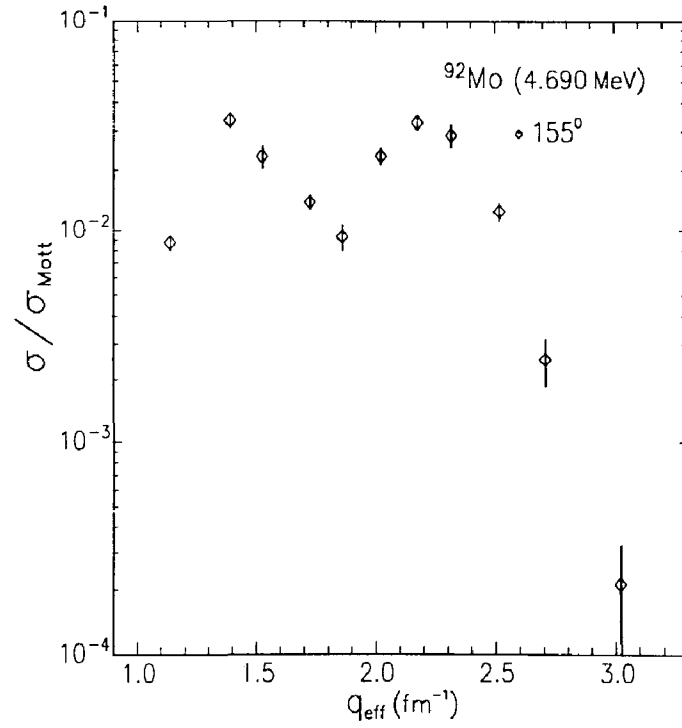


Figure B.29 Data for scattering at backward angles from state at 4.690 MeV.

Normalized Cross Sections for level at 4.925 MeV					
$E(\text{MeV})$	$\theta$ ( $^\circ$ )	$d\theta$ ( $^\circ$ )	$d\phi$ ( $^\circ$ )	$\sigma(\text{mb}/\text{sr})$	$d\sigma(\text{mb}/\text{sr})$
189.6	155.0	0.58	3.54	$9.262E-08$	$9.610E-09$
125.7	155.0	0.75	1.82	$6.079E-07$	$4.430E-08$
175.1	150.0	0.75	2.18	$6.338E-08$	$1.270E-08$
239.7	155.0	0.75	3.64	$1.594E-07$	$1.220E-08$
219.2	155.0	0.75	2.72	$1.603E-07$	$1.840E-08$
259.0	155.0	0.75	3.64	$2.163E-08$	$3.940E-09$
204.8	155.0	0.75	3.64	$1.435E-07$	$1.120E-08$
159.5	155.0	0.75	2.73	$9.641E-08$	$9.660E-09$
139.4	155.0	0.75	3.64	$3.539E-07$	$4.150E-08$
290.4	155.0	0.75	2.91	$3.275E-09$	$8.450E-10$
100.3	155.0	0.75	3.64	$5.651E-07$	$3.880E-08$

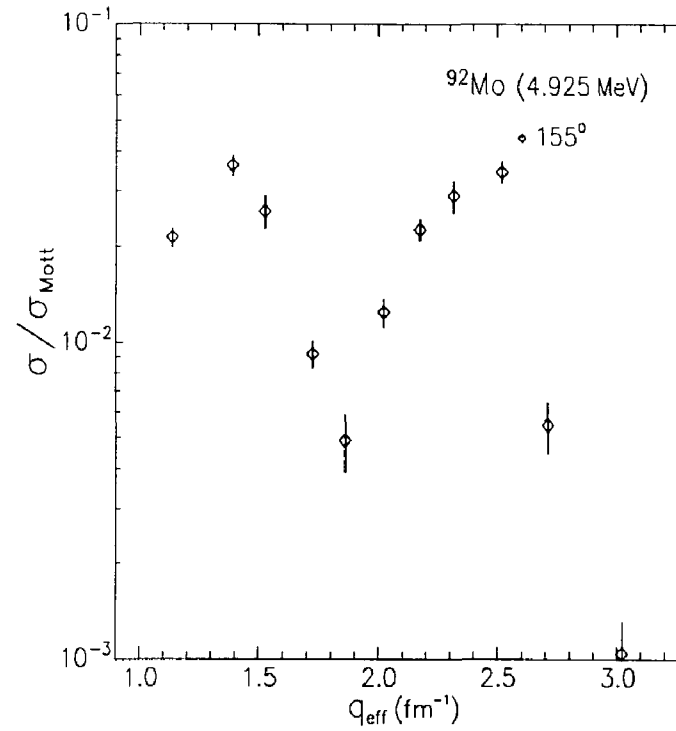


Figure B.30 Data for scattering at backward angles from state at 4.925 MeV.

Normalised Cross Sections for level at 5.090 MeV					
$E(\text{MeV})$	$\theta$ ( $^\circ$ )	$d\theta$ ( $^\circ$ )	$d\phi$ ( $^\circ$ )	$\sigma(\text{mb/sr})$	$d\sigma(\text{mb/sr})$
189.6	155.0	0.58	3.54	$7.613E-08$	$8.620E-09$
125.7	155.0	0.75	1.82	$6.131E-07$	$4.620E-08$
175.1	150.0	0.75	2.18	$3.522E-07$	$3.420E-08$
239.7	155.0	0.75	3.64	$7.794E-09$	$2.100E-09$
219.2	155.0	0.75	2.72	$3.232E-08$	$7.690E-09$
259.0	155.0	0.75	3.64	$5.588E-09$	$1.970E-09$
204.8	155.0	0.75	3.64	$2.476E-08$	$3.840E-09$
159.5	155.0	0.75	2.73	$1.811E-07$	$1.470E-08$
139.4	155.0	0.75	3.64	$3.175E-07$	$3.800E-08$
100.3	155.0	0.75	3.64	$2.211E-06$	$1.230E-07$

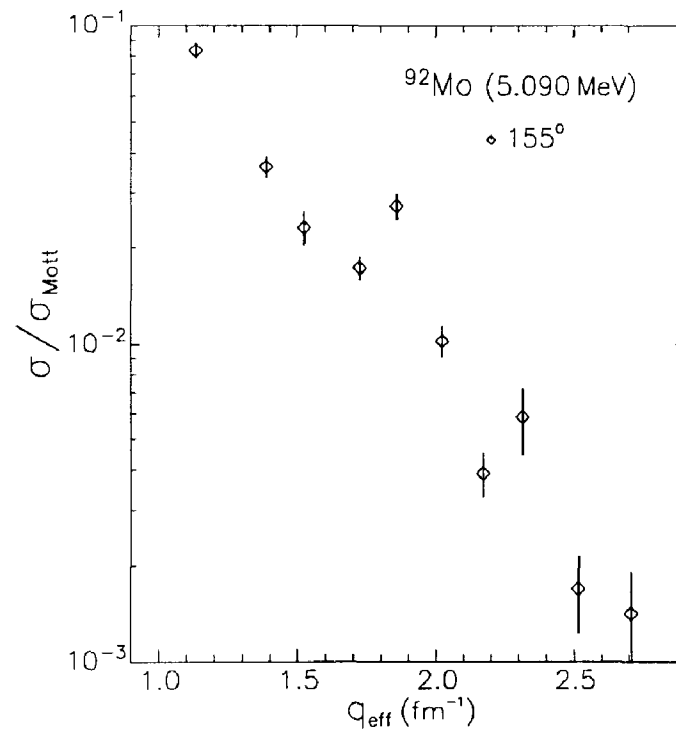


Figure B.31 Data for scattering at backward angles from state at 5.090 MeV.

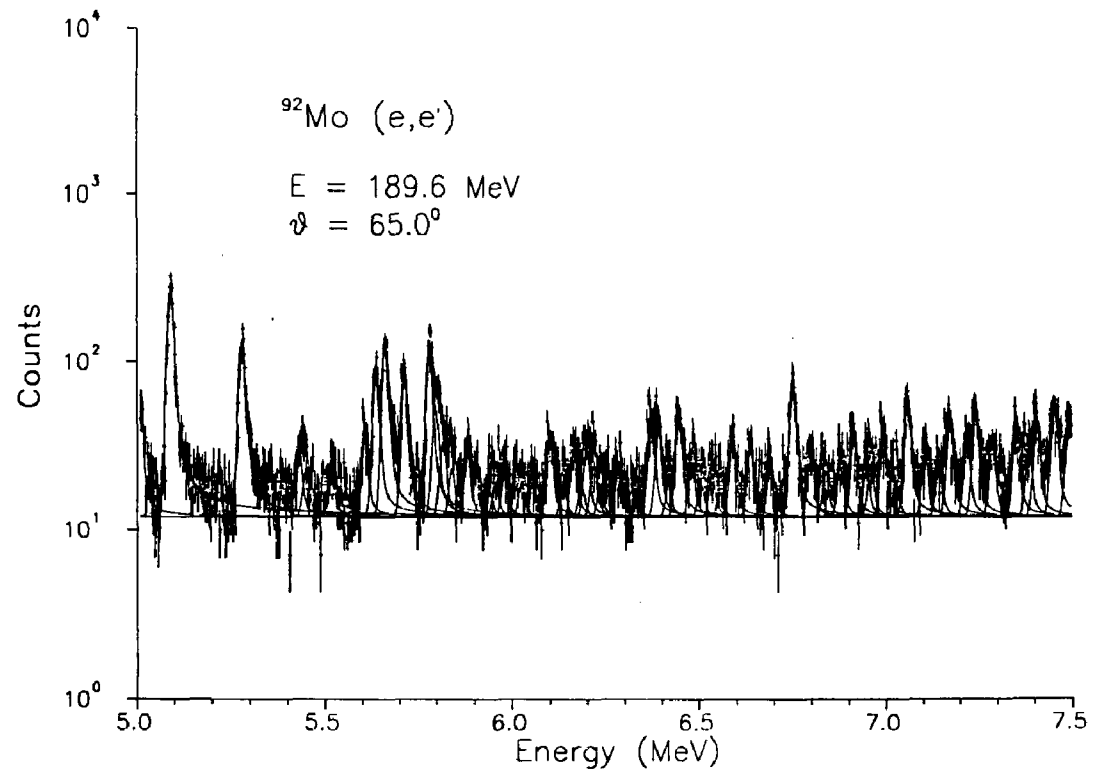


Figure B.32 Fitted spectrum for 189.6 MeV electrons scattered at 65.0 degrees.

## Appendix C

### Transition Density Parameters

This appendix contains the expansion parameters for the Transition densities shown in Chapter 6. The forms of the expansions are given in Chapter 5. The error bands shown in the figures of Chapter 6 are determined from the full error matrix and can not be fully reproduced using the errors of the parameters. The correlations between the Polynomial-Gaussian parameters are so large that the error band can not be well produced without the entire error matrix. For densities expanded in the PG model no errors are given for the coefficients.

The integral of the densities is given by the  $B(\lambda)$  values. For  $\rho_\lambda$  and  $J_{\lambda,\lambda}$  these correspond to  $B(E\lambda)$  and  $B(M\lambda)$  defined in Chapter 2. For the current  $J_{\lambda,\lambda+1}$  we can define a similiar integral,

$$B(J\lambda) = \left[ \frac{J_f}{J_i} \int_0^\infty J_{\lambda,\lambda+1}(r) r^{\lambda+3} dr \right]^2$$

These transition probabilities are also given in the following tables.

Transition Charge Density Parameters  
Fourier-Bessel Expansion  $R_0 = 11.0 \text{ fm}$

N	1.509	2.282	3.096	3.369	3.545	3.583
	2 <sup>+</sup>	4 <sup>+</sup>	2 <sup>+</sup>	4 <sup>+</sup>	2 <sup>+</sup>	3 <sup>-</sup>
1	8.652 ± 0.146	2.776 ± 0.079	4.234 ± 0.098	0.591 ± 0.038	1.185 ± 0.096	2.078 ± 0.060
2	18.633 ± 0.166	8.565 ± 0.114	8.785 ± 0.096	1.266 ± 0.033	2.465 ± 0.073	5.096 ± 0.084
3	10.829 ± 0.171	9.137 ± 0.113	4.509 ± 0.116	0.822 ± 0.032	1.025 ± 0.104	3.931 ± 0.084
4	-4.286 ± 0.129	3.343 ± 0.098	-2.504 ± 0.090	-0.144 ± 0.048	-0.805 ± 0.074	-0.266 ± 0.082
5	-7.019 ± 0.114	-1.396 ± 0.080	-2.896 ± 0.088	-0.475 ± 0.044	-0.521 ± 0.056	-1.760 ± 0.074
6	-0.619 ± 0.150	-1.771 ± 0.080	0.731 ± 0.135	-0.205 ± 0.056	0.390 ± 0.069	-0.107 ± 0.090
7	2.652 ± 0.119	-0.042 ± 0.067	1.950 ± 0.111	0.025 ± 0.093	0.794 ± 0.147	1.028 ± 0.091
8	1.251 ± 0.114	0.495 ± 0.060	0.626 ± 0.137	0.033 ± 0.103	0.500 ± 0.235	0.565 ± 0.073
9	-0.273 ± 0.115	0.130 ± 0.145	-0.173 ± 0.117	-0.001 ± 0.133	0.124 ± 0.154	0.005 ± 0.048
10	-0.220 ± 0.093	-0.185 ± 0.132	0.123 ± 0.132	-0.005 ± 0.114	-0.004 ± 0.104	-0.021 ± 0.038
11	0.028 ± 0.136	-0.026 ± 0.170	0.290 ± 0.323	-0.002 ± 0.109	-0.027 ± 0.066	0.020 ± 0.035
12	0.021 ± 0.116	0.036 ± 0.179	0.088 ± 0.504	0.001 ± 0.059	0.015 ± 0.050	-0.007 ± 0.028
13	0.011 ± 0.112	-0.027 ± 0.072	-0.019 ± 0.537	0.000 ± 0.051	-0.002 ± 0.050	-0.002 ± 0.021
14	-0.001 ± 0.094	0.014 ± 0.051	0.022 ± 0.356	-0.001 ± 0.046	0.000 ± 0.051	0.003 ± 0.014
15	-0.004 ± 0.042	-0.006 ± 0.034	0.025 ± 0.128	-0.000 ± 0.018	-0.002 ± 0.019	-0.001 ± 0.012
B(Eλ) <sup>†</sup>	1.091E+03 ±4.8 %	3.428E+05 ±27.2 %	2.6841E+02 ±6.6 %	3.6704E+04 ±29.5 %	1.9710E+01 ±29.1 %	4.3537E+03 ±8.8 %

<sup>†</sup> The units of  $B(E\lambda)$  are  $e^2 \text{ fm}^{2\lambda}$ .

Table C.1 This table gives the transition density expansion coefficients for states fit with a single density using the FBE. The form of the expansion is given in Chapter 5. The coefficients  $A_n$  have all been multiplied by a factor of 1000.



Transition Charge Density Parameters  
Fourier-Bessel Expansion  $R_0 = 11.0 \text{ fm}$

N	3.879	3.929	4.598
	4 <sup>+</sup>	2 <sup>+</sup>	2 <sup>+</sup>
1	1.422 ± 0.068	3.429 ± 0.131	3.723 ± 0.349
2	3.959 ± 0.093	6.460 ± 0.126	1.934 ± 0.372
3	4.245 ± 0.103	1.934 ± 0.143	-2.144 ± 0.248
4	1.564 ± 0.097	-3.338 ± 0.096	-4.145 ± 0.231
5	-0.820 ± 0.095	-1.945 ± 0.106	-5.038 ± 0.296
6	-0.982 ± 0.126	1.651 ± 0.134	-3.615 ± 0.301
7	-0.111 ± 0.153	1.824 ± 0.170	-1.678 ± 0.277
8	0.210 ± 0.108	0.153 ± 0.198	0.138 ± 0.255
9	0.018 ± 0.123	-0.337 ± 0.135	0.052 ± 0.369
10	-0.036 ± 0.113	0.017 ± 0.142	-0.247 ± 0.804
11	0.007 ± 0.092	0.073 ± 0.116	-0.435 ± 0.751
12	0.007 ± 0.065	-0.034 ± 0.085	0.243 ± 0.502
13	-0.005 ± 0.053	-0.008 ± 0.065	0.165 ± 0.287
14	0.001 ± 0.043	0.014 ± 0.045	0.153 ± 0.190
15	-0.000 ± 0.034	-0.005 ± 0.039	-0.112 ± 0.108
<b>B(Eλ)<sup>†</sup></b>	<b>1.490E + 05</b>	<b>1.877E + 02</b>	<b>5.182E + 02</b>
	±23.1 %	±10.5 %	±23.2 %

<sup>†</sup> The units of  $B(E\lambda)$  are  $e^2 \text{ fm}^{2\lambda}$

Table C.1 (Continued).

Transition Charge and Current Density Parameters

Fourier-Bessel Expansion  $R_0 = 11.0 \text{ fm}$

N	2.527 5 <sup>-</sup>		2.850 3 <sup>-</sup>		4.159 5 <sup>-</sup>	
	charge	current	charge	current	charge	current
1	2.463 ± 0.031	-0.769 ± 0.155	8.581 ± 0.094	-1.275 ± 0.287	2.013 ± 0.047	-0.497 ± 0.612
2	7.286 ± 0.047	-4.196 ± 0.598	20.878 ± 0.125	-5.915 ± 0.980	4.572 ± 0.060	-2.981 ± 1.079
3	8.685 ± 0.055	-8.976 ± 0.765	16.322 ± 0.113	-8.998 ± 0.852	5.158 ± 0.066	-8.025 ± 0.821
4	4.224 ± 0.065	-9.428 ± 0.444	-0.798 ± 0.099	-2.880 ± 1.043	3.420 ± 0.090	-12.783 ± 0.586
5	-1.097 ± 0.063	-4.103 ± 0.796	-8.384 ± 0.110	7.799 ± 1.251	0.662 ± 0.144	-12.876 ± 0.539
6	-2.757 ± 0.053	1.045 ± 1.269	-3.096 ± 0.1 <sup>7</sup>	11.439 ± 0.556	-0.915 ± 0.117	-7.975 ± 0.857
7	-1.596 ± 0.046	1.804 ± 1.174	2.245 ± 0.096	6.860 ± 1.188	-0.826 ± 0.066	-2.574 ± 0.925
8	-0.338 ± 0.056	0.440 ± 0.574	2.108 ± 0.063	1.792 ± 0.882	-0.214 ± 0.098	-0.260 ± 0.603
9	0.068 ± 0.136	-0.102 ± 0.157	0.630 ± 0.089	0.074 ± 0.273	-0.045 ± 0.175	-0.190 ± 0.643
10	0.038 ± 0.341	0.028 ± 0.115	0.565 ± 0.185	0.004 ± 0.075	-0.049 ± 0.153	-0.185 ± 0.824
11	-0.097 ± 0.435	0.023 ± 0.089	0.727 ± 0.268	0.003 ± 0.052	-0.024 ± 0.122	0.059 ± 0.757
12	-0.225 ± 0.348	-0.026 ± 0.068	0.294 ± 0.246	-0.008 ± 0.036	0.026 ± 0.095	0.063 ± 0.642
13	-0.237 ± 0.193	0.003 ± 0.050	-0.121 ± 0.194	0.006 ± 0.026	-0.002 ± 0.089	-0.043 ± 0.581
14	-0.133 ± 0.080	0.010 ± 0.036	-0.147 ± 0.114	-0.001 ± 0.019	0.008 ± 0.048	-0.006 ± 0.442
15	-0.035 ± 0.018	-0.001 ± 0.022	-0.042 ± 0.032	-0.002 ± 0.012	-0.019 ± 0.027	0.025 ± 0.299
B(λ) <sup>†</sup>	3.407E+07 ±5.1 %	1.735E+08 ±56.9 %	7.595E+04 ±3.3 %	1.802E+05 ±55.7 %	4.818E+07 ±8.9 %	7.625E+07 ±13.0 %

<sup>†</sup> For charge densities  $B(\lambda)=B(E\lambda)$  and is in units of  $e^2 fm^{2\lambda}$ .

For current densities  $B(\lambda)=B(J\lambda)$  and is in units of  $\mu^2 fm^{2\lambda+2}$ .

Table C.2 This table gives the transition density expansion coefficients for states fit with two densities,  $\rho_\lambda$  and  $J_{\lambda,\lambda+1}$ , using the FBE. The form of the expansion is given in Chapter 5. The coefficients  $A_n$  have all been multiplied by a factor of 1000.

Transition Charge and Current Density Parameters  
 Fourier-Bessel Expansion  $R_0 = 11.0 \text{ fm}$

N	4.312 5 <sup>-</sup>		4.555 7 <sup>-</sup>		5.090 4 <sup>+</sup>	
	charge	current	charge	current	charge	current
1	0.832 ± 0.033	1.173 ± 1.283	0.637 ± 0.017	-1.053 ± 0.108	2.102 ± 0.063	-1.564 ± 2.826
2	2.648 ± 0.057	2.429 ± 4.039	2.478 ± 0.038	-5.930 ± 0.380	5.586 ± 0.087	1.563 ± 8.344
3	3.590 ± 0.033	-1.690 ± 5.111	4.536 ± 0.063	-14.807 ± 0.563	4.932 ± 0.230	3.044 ± 3.928
4	2.390 ± 0.125	-10.081 ± 2.906	5.022 ± 0.089	-21.836 ± 0.664	-0.003 ± 0.295	4.212 ± 5.501
5	0.340 ± 0.218	-13.502 ± 1.032	3.594 ± 0.079	-20.823 ± 0.747	-2.856 ± 0.178	-0.863 ± 1.129
6	-0.727 ± 0.186	-8.449 ± 3.060	1.574 ± 0.072	-12.686 ± 0.691	-1.541 ± 0.283	-0.909 ± 9.075
7	-0.599 ± 0.087	-2.112 ± 2.663	0.280 ± 0.067	-4.128 ± 0.621	0.252 ± 0.374	2.330 ± 0.415
8	-0.178 ± 0.040	-0.104 ± 1.354	-0.077 ± 0.050	-0.017 ± 0.492	0.412 ± 0.144	-2.372 ± 2.100
9	-0.022 ± 0.051	-0.429 ± 0.709	-0.024 ± 0.034	0.310 ± 0.380	0.123 ± 0.141	1.009 ± 2.547
10	-0.026 ± 0.046	-0.118 ± 0.702	0.021 ± 0.027	-0.170 ± 0.272	0.180 ± 0.235	-0.559 ± 2.255
11	-0.013 ± 0.035	0.178 ± 0.531	0.004 ± 0.022	-0.118 ± 0.227	0.138 ± 0.208	0.309 ± 1.764
12	0.010 ± 0.024	0.011 ± 0.491	-0.007 ± 0.015	0.073 ± 0.168	-0.047 ± 0.159	-0.181 ± 1.307
13	0.004 ± 0.017	-0.079 ± 0.356	-0.002 ± 0.013	0.055 ± 0.142	-0.053 ± 0.110	0.127 ± 0.975
14	-0.004 ± 0.011	0.044 ± 0.361	-0.000 ± 0.009	-0.013 ± 0.110	0.027 ± 0.079	-0.125 ± 0.694
15	-0.002 ± 0.005	-0.026 ± 0.318	-0.000 ± 0.002	-0.010 ± 0.038	0.021 ± 0.043	0.282 ± 0.721
B(λ) <sup>†</sup>	3.474E+06 ±13.3 %	1.955E+09 ±210.0 %	1.070E+10 ±10.7 %	1.648E+12 ±35.3 %	3.229E+05 ±12.7 %	1.795E+08 ±165.1 %

<sup>†</sup> For charge densities  $B(\lambda)=B(E\lambda)$  and is in units of  $e^2 fm^{2\lambda}$ .

For current densities  $B(\lambda)=B(J\lambda)$  and is in units of  $\mu^2 fm^{2\lambda+2}$ .

Table C.2 (Continued).

Transition Charge Density Parameters  
Polynomial-Gaussian Expansion

N	2.612	4.495	4.724	5.007	
	6 <sup>+</sup>	2 <sup>+</sup>	4 <sup>+</sup>	(1 <sup>-</sup> )	
				charge	current
1	0.2376	6.6911	1.8229	9.0082	-12.9781
2	-0.2724	-19.5438	-1.1893	-25.8161	7.2538
3	0.1601	7.3302	0.5174	31.0083	-12.2086
4	0.0000	-0.9415	0.0014	-11.8337	2.2691
5	-	0.1465	-	1.1244	0.0010
$r_0(fm)$	2.026	2.086	2.266	2.326	
$B(\lambda)^{\dagger}$	2.654E+08	6.452E+01	1.156E+05	5.079E-02	1.070E+01
	±20.4 %	±11.3 %	±23.3 %	±85.0 %	±713.1 %

<sup>†</sup> For charge densities  $B(\lambda)=B(E\lambda)$  and is in units of  $e^2 fm^{2\lambda}$ .

For current densities  $B(\lambda)=B(J\lambda)$  and is in units of  $\mu^2 fm^{2\lambda+2}$ .

Table C.3 This table gives the transition density expansion coefficients for states fit with the Polynomial-Gaussian expansion. The form of the expansion is given in Chapter 5. The coefficients  $A_n$  have all been multiplied by a factor of 1000.